SYNTHESIS AND APPLICATION OF POLYMERIC MICELLES ASSEMBLED FROM PENTAFLUOROPHENYL ESTER-CONTAINING AMPHIPHILIC BLOCK COPOLYMERS

Miss Panittha Damsongsang

A Dissertation Submitted in Partial Fulfillment of the Requirements
for the Degree of Doctor of Philosophy in Chemistry
Department of Chemistry
FACULTY OF SCIENCE
Chulalongkorn University
Academic Year 2021

การสังเคราะห์และการประยุกต์ไมเซลล์พอลิเมอร์ที่ประกอบขึ้นจากแอมฟิฟิลิกบล็อกโคพอลิเมอร์ที่มีเพนทะฟลูออโรเฟนิลเอสเทอร์

น.ส.พณิฎฐา ดำส่งแสง

วิทยานิพนธ์นี้เป็นส่วนหนึ่งของการศึกษาตามหลักสูตรปริญญาวิทยาศาสตรดุษฎีบัณฑิต
สาขาวิชาเคมี ภาควิชาเคมี
คณะวิทยาศาสตร์ จุฬาลงกรณ์มหาวิทยาลัย
ปีการศึกษา 2564

Thesis Title	SYNTHESIS AND APPLICATION OF POLYMERIC MICELLES ASSEMBLED FROM PENTAFLUOROPHENYL ESTER-CONTAINING AMPHIPHILIC BLOCK COPOLYMERS
By	Miss Panittha Damsongsang
Field of Study	Chemistry
Thesis Advisor	Professor VORAVEE HOVEN, Ph.D.

Accepted by the FACULTY OF SCIENCE, Chulalongkorn University in Partial Fulfillment of the Requirement for the Doctor of Philosophy

..... Dean of the FACULTY OF SCIENCE
(Professor POLKIT SANGVANICH, Ph.D.)

DISSERTATION COMMITTEE

..... Chairman
(Professor VUDHICHAI PARASUK, Ph.D.)

..... Thesis Advisor
(Professor VORAVEE HOVEN, Ph.D.)

..... Examiner
(Assistant Professor PANUWAT PADUNGROS, Ph.D.)

..... Examiner
(Junjuda Unruangsri, Ph.D.)

..... External Examiner
(Associate Professor Panya Sunintaboon, Ph.D.)

พณิฎฐา ดำส่งแสง : การสังเคราะห์และการประยุกต์ไมเซลล์พอลิเมอร์ที่ประกอบขึ้นจากแอมฟิฟิลิกบล็อกโคพอลิเมอร์ที่มีเพนทะฟลูออโรเฟนิลเอสเทอร์. (SYNTHESIS AND APPLICATION OF POLYMERIC MICELLES ASSEMBLED FROM PENTAFLUOROPHENYL ESTER-CONTAINING AMPHIPHILIC BLOCK COPOLYMERS) อ.ที่ปรึกษาหลัก : ศ. ดร.วรวีร์ โฮเว่น

พอลิเมอร์ตั้งต้นที่มีหมู่เพนทะฟลูออโรเฟนิลเอสเทอร์ที่ปรับเปลี่ยนหมู่ฟังก์ชันได้ ซึ่งได้แก่ พอลิเพนทะฟลูออโรเฟนิลแอคริเลต (PPFPA) และพอลิเพนทะฟลูออโรเฟนิลเมทาคริเลต (PPFPMA) และพอลิเมอร์ซึ่งเป็นสวิทเทอร์ไอออนิกของพอลิ(2-เมทิลเมทาคริโลอิลออกซีเอทิลฟอสโฟริลโคลีน) (PMPC) เป็นพอลิเมอร์สองชนิดที่มีสมบัติการละลายต่างกันอย่างสิ้นเชิง จึงเป็นการยากที่จะสังเคราะห์ไดบล็อกโคพอลิเมอร์จากพอลิเมอร์สองประเภทนี้แบบควบคุมได้ด้วยวิธีดั่งเดิม งานวิจัยนี้รายงานการสังเคราะห์และการเกิดเป็นอนุภาคของไดบล็อกโคพอลิเมอร์ของพอลิเมอร์สองประเภทข้างต้นด้วยวิธี polymerization-induced self-assembly (PISA) ผ่านกลไกการเกิดปฏิกิริยา reversible addition fragmentation chain transfer (RAFT) dispersion polymerization นับเป็นแนวทางใหม่ซึ่งไม่มีการศึกษาวิจัยมาก่อน โดย PMPC ที่สังเคราะห์โดย RAFT polymerization เป็นบล็อกแรกทำหน้าที่เป็นสายถ่ายโอนโซ่ (PMPC Macro-CTA) ในการสังเคราะห์พอลิเมอร์ที่มีหมู่เพนทะฟลูออโรฟีนิวเอสเทอร์เป็นบล็อกที่สอง ภายใต้การใช้สัดส่วนโคพอลิเมอร์และองค์ประกอบของแข็งที่เหมาะสม ทำให้ได้โครงสร้างนาโนที่ประกอบขึ้นเป็นพอลิเมอร์ไมเซลล์ที่มีรูปร่างทรงกลม โดยมีขนาดเล็กกว่า 100 นาโนเมตร จากการวิเคราะห์ด้วยเทคนิคการกระเจิงแสงแบบพลวัต และกล้องจุลทรรศน์อิเล็กตรอนแบบส่องผ่าน พอลิเมอร์ไมเซลล์สามารถถูกดัดแปรให้มีหมู่ฟังก์ชันที่หลากหลายได้ผ่านการทำปฏิกิริยาดัดแปรหลังพอลิเมอไรเซชันของแกนกลางซึ่งเป็นบล็อกของพอลิเมอร์ตั้งต้นที่มีหมู่เพนทะฟลูออโรเฟนิลโดยการเกิดปฏิกิริยากับตัวดัดแปรนิวคลีโอไฟล์ต่างๆ นับเป็นวัสดุที่มีศักยภาพในการพัฒนาไปใช้ในด้านต่างๆได้อย่างกว้างขวาง

สาขาวิชา เคมี ลายมือชื่อนิสิต .....

ปีการศึกษา 2564 ลายมือชื่อ อ.ที่ปรึกษาหลัก .....

6072855823 : MAJOR CHEMISTRY

KEYWORD: Pentafluorophenyl ester Post-polymerization modification
Polymerization-induced self-assembly

Panittha Damsongsang : SYNTHESIS AND APPLICATION OF POLYMERIC MICELLES ASSEMBLED FROM PENTAFLUOROPHENYL ESTER-CONTAINING AMPHIPHILIC BLOCK COPOLYMERS. Advisor: Prof. VORAVEE HOVEN, Ph.D.

Functionalizable pentafluorophenyl ester (PFP)-based polymer precursors, namely poly(pentafluorophenyl acrylate) (PPFPA) and poly(pentafluorophenyl metharylate) (PPFPMA), and zwitterionic poly(2-methacryloyloxyethyl phosphorylcholine) (PMPC) are the two polymers having extremely different solubility. It is therefore almost impossible to synthesize their block copolymers in a controlled manner by the conventional approach. Herein, we demonstrated, for the first time, that the synthesis and *in situ* formation of nanoassemblies of their diblock copolymer can be done via polymerization-induced self-assembly (PISA) using reversible addition-fragmentation chain-transfer (RAFT) dispersion polymerization. PMPC was synthesized as the first block and further employed as a macro chain transfer agent (PMPC Macro-CTA) for the synthesis of the PFP-based polymer as a second block. Synthesized using an appropriate range of copolymer composition and solid concentration, *in situ* self-assembled nanostructures of the diblock copolymers were evaluated by dynamic light scattering and transmission electron microscopy. To demonstrate the functionalizability of the core-forming block of PFP-based polymer precursor, the nanoparticles were subjected to post-polymerization modification with nucleophilic modifiers yielding nanostructures bearing multifunctionality that may be applicable for a wide range of applications.

Field of Study: Chemistry Student's Signature .....

Academic Year: 2021 Advisor's Signature .....

ACKNOWLEDGEMENTS

First, I would like to express my deepest appreciation to my advisor, Professor Dr. Voravee P. Hoven, for her invaluable support, patience, knowledge, moral support, and feedback. I also could not have undertaken this journey without Associate Professor Dr. Shin-ichi Yusa, who is my advisor in Japan, for his generous support and providing lots of knowledge. Additionally, I am grateful to all committees for their valuable suggestions.

Many thanks to VH and SY members for their advice, suggestions, and kind help during my PhD study. Thanks should also go to my best friends who are my companions on the PhD journey, Miss Piyawan Paisrisarn and Miss Haruethai Kongcharoen, for their emotional support and inspiration.

Lastly, I would like to extend my sincere thanks to my family and my sister for their love, all support, entertainment, positive thinking, and encouragement. Their always belief in me has kept my spirits and motivation high during my study.

Panittha Damsongsang

TABLE OF CONTENTS

Page

.....iii

ABSTRACT (THAI) iii

..... iv

ABSTRACT (ENGLISH) iv

ACKNOWLEDGEMENTS v

TABLE OF CONTENTS vi

LISTS OF FIGURES..... 9

LIST OF TABLES 14

CHAPTER I 15

INTRODUCTION 15

1.1 Theory and Literature Review 15

1.2 Objectives..... 31

1.2 Scope of investigation 31

CHAPTER II..... 33

MATERAILS AND METHODS 33

2.1 Materials 33

2.2 Characterization 34

2.3 Methods..... 34

2.3.1 Synthesis of pentafluorophenyl acrylate (PFPA) monomer..... 34

2.3.2 Synthesis of PMPC macro-CTA 35

2.3.3 Dispersion polymerization of PPFPA using PMPC macro-CTA..... 36

2.3.4 Dispersion polymerization of PFPMA using PMPC macro-CTA 37

2.3.5 Post-polymerization modification of $PMPC_n$-*b*-$PPFPMA_m$ by 1-pyrenemethylamine 39

2.3.6 Synthesis of PPFPA by RAFT polymerization 40

2.3.7 Post-polymerization modification of PPFPA 40

2.3.8 Determination of critical micelle concentration 41

2.3.9 Oxidation stability of PDA_x-*co*-$PPEA_y$ micelles 42

CHAPTER III 43

RESULTS AND DISCUSSION 43

3.1 Synthesis of PMPC macro-CTA 43

3.2 Dispersion polymerization of PPFPA using PMPC macro-CTA 46

3.2.1 Synthesis of PFPA monomer 46

3.2.2 Synthesis of PMPC-*b*-PPFPA in 2,2,2-trifluoroethanol 49

3.2.3 Synthesis of PMPC-*b*-PPFPA in ethanol 54

3.3 Dispersion polymerization of PFPMA using PMPC macro-CTA 59

3.3.1 Characterization of nanostructures formed upon PISA 63

3.4 Core functionalization of nanostructures 68

3.5 Post-polymerization modification of PPFPA for being used as an antioxidant nanoparticle 76

3.5.1 Synthesis of PPFPA as a polymer precursor 76

3.5.2 Micellar formation of PDA_x-*co*-$PPEA_y$ 82

3.5.2.1 Size distribution of PDAx-co-PPEAy 82

3.5.2.2 CMC determination of the micelles 83

3.5.3 Oxidation stability of PDA_x-*co*-$PPEA_y$ 84

CHAPTER IV 87

CONCLUSION AND SUGGESTION 87

REFERENCES 90

APPENDIX 104

VITA 110

LISTS OF FIGURES

Figure 1.1 Preparation of DOX and ICG encapsulated in POEGMA-*b*-POMFMA polymeric micelles [23]. 16

Figure 1.2 Chemical structures of amphiphilic block copolymer, 1-pyrenecarboxaldehyde (Py-CHO) as a probe, and p-phenylenediamine (PPD) as an analyte [8]. 17

Figure 1.3 Mechanistic morphological transformation of diblock copolymeric nanostructures of PGMA-*b*-PHPMA from spheres, worms to vesicles [35]. 19

Figure 1.4 Phase diagram and TEM images of diblock copolymeric PGMA-*b*-PHPMA nanostructures of (A) series of $PGMA_{47}$-*b*-PHPMA and (B) $PGMA_{78}$-*b*-PHPMA with the variety of DP_{PHPMA} and total solid concentration [36]. 20

Figure 1.5 Post-polymerization modification of PPFPMA with reactive modifiers to yield the redox-responsive nanogels [56]. 22

Figure 1.6 Synthetic route of (a) PDMAm-*b*-P(DMAm-co-PFPA) macro-CTA in EtOH, and (B) PDMAm-*b*-P(DMAm-*co*-PFPA)-*b*-PNIPAm via PITSA at 50°C in water. Thermoresponsive nano-objects were subsequently treated with HMDA [59]. 24

Figure 1.7 Schematic illustration of the preparation of PEG_{113}-b-$PPFMA_{200}$ by RAFT-mediated photoinitiated PISA at 37°C in DMSO and subsequently treated with ethylenediamine and cystamine to prepare P1 and for P2, respectively [60]. 25

Figure 1.8 Schematic illustration of PMPC-*b*-PHPMA and morphological transition depending on DP_{PHPMA} core-forming block and total solids concentration (w/w %) [63]. 27

Figure 1.9 Schematic illustration of the preparation of poly(MPC-*co*-PENAO)-*b*-PMMA via PISA in H_2O/EtOH [70]. 28

Figure 2.1 Synthesis of PMPC macro-CTA via RAFT polymerization 35

Figure 2.2 Synthetic route of PMPC-*b*-PPFPA via RAFT dispersion polymerization 36

Figure 2.3 Synthetic route of PMPC-*b*-PPFPMA via RAFT dispersion polymerization...37

Figure 2.4 Post-polymerization modification of $PMPC_n$-*b*-$PPFPMA_m$ with 1-pyrenemethylamine (PMA).....39

Figure 2.5 Synthetic route of PPFPA by RAFT polymerization followed by post-polymerization modification to prepare antioxidant nanoparticles.....40

Figure 3.1 ^{1}H-NMR spectra of PMPC macro-CTAs having DP of (A) 25, (B) 50, and (C) 100.....44

Figure 3.2 GPC traces of PMPC macro-CTA DP_{25} ( ), DP_{50} (----) and DP_{100} (----).....45

Figure 3.3 Synthesis of PFPA monomer 46

Figure 3.4 NMR spectra of PFPA monomer: (A) ^{1}H NMR, (B) ^{13}C NMR, and (C) ^{19}F NMR 48

Figure 3.5 Solutions of (A) PM_{25}-PF_m-*20*%, and (B) PM_{50}-PF_m-*20*% performed in TFE..49

Figure 3.6 (A) A plot of monomer conversion as a function of polymerization time and (B) pseudo-first-order polymerization kinetics of PM_{25}-PF_m and PM_{50}-PF_m series with 20% solid concentration.....50

Figure 3.7 DLS profiles and TEM images of PM_{25}-PF_m-*20*% and DLS profiles of PM_{50}-PF_m-*20*% in TFE at C_p = 1 mg/mL.....51

Figure 3.8 The relationship between mean diameter of the particles and DP_{PPFPA} of (A) PM_{25}-PF_m-*20*% and (B) PM_{50}-PF_m-*20*% determined by DLS at C_p = 1 mg/mL.....52

Figure 3.9 Polymer solutions of PM_{25}-PF_m-*20*% prepared in ethanol.....54

Figure 3.10 (A) A plot of monomer conversion vs polymerization time and (B) pseudo-first-order polymerization kinetics of PM_{25}-PF_m-*20*% series in EtOH.....54

Figure 3.11 DLS profiles of PM_{25}-PF_m-*20*% in EtOH using polymer concentration (C_p) 1 mg/mL 56

Figure 3.12 The relationship between mean particle diameter and DP_{PPFPA} of PM_{25}-PF_m-*20*% determined by DLS as a number distribution function at C_p = 1 mg/mL.....56

Figure 3.13 Polymer solutions of PM_{100}-PF_m-*20*% prepared in EtOH 57

Figure 3.14 (A) A plot of monomer conversion vs polymerization time and (B) pseudo-first-order polymerization kinetics of PM_{100}-PF_m-*20*% in ethanol. 57

Figure 3.15 DLS profiles of PM_{100}-PF_m-*20*% in EtOH at C_p = 1 mg/mL.....58

Figure 3.16 The relationship between mean particle diameter and DP_{PPFPA} of PM_{100}-PF_m-*20*% determined by DLS as a number distribution function at C_p = 1 mg/mL.....58

Figure 3.17 (A) ^{1}H NMR spectrum of PM_{50}-PFM_{60}, and (B) ^{13}C NMR spectrum of PM_{50}-PFM_{60}, recorded in $CDCl_3$/MeOH-d_4 (3/1, v/v) at 60°C.....60

Figure 3.18 (A) ^{19}F NMR spectrum, recorded in $CDCl_3$/MeOH-d_4 (3/1, v/v) at 60 °C and (B) ATR-IR spectrum of PM_{50}-PFM_{60}.....61

Figure 3.19 (A) Monomer conversion as a function of polymerization time and (B) pseudo-first order kinetics of PFPMA polymerization using PMPC as a macro-CTA.....62

Figure 3.20 TEM images (10,000x) and proposed morphologies of the PM_{50}-PFM_m and PM_{100}-PFM_m series having 5 and 20% solid concentration. Each TEM image contains two insets; one on the top right shows an image of the copolymer solution and one at the bottom right shows a magnified TEM image (40,000x). 64

Figure 3.21 DLS profiles of PM_{50}-PFM_m and PM_{100}-PFM_m series with a variety of solid concentration.....65

Figure 3.22 ^{1}H NMR spectra of (A) PM_{100}-PFM_{61}-*5*%, recorded in $CDCl_3$/MeOH-d_4 (3/1, v/v) at 60 °C, (B) PMA and (C) PM_{100}-PFM_{61}-*5*% after reacting with PMA, recorded in MeOH-d_4 at 25 °C.....70

Figure 3.23 (A) ^{19}F NMR spectra recorded in $CDCl_3$/MeOH-d_4 (3/1, v/v) at 60 °C and (B) FT-IR spectra of PM_{100}-PFM_{61}-*5*% (a) before and (b) after reacting with PMA. 71

Figure 3.24 (A) UV-visible absorption spectra in MeOH at 25 °C and (B) fluorescence emission spectra (λ_{ex} = 340 nm) in H_2O at 25 °C with slid width of 1.0 nm of PMA (—), PM_{100}-PFM_{61}-*5*% before (···) and after (---) reacting with PMA. 72

Figure 3.25 (A) Representative TEM micrographs and (B) DLS profiles of PM_{100}-PFM_{61} before and after modification with PMA, prepared in H_2O with polymer concentration (C_p) = 1.0 g/L, I indicates the light scattering intensity (LSI). 75

Figure 3.26 Synthetic route of PPFPA by RAFT polymerization and post-polymerization modification to be used as an antioxidant nanoparticle.....76

Figure 3.27 ^{1}H NMR spectrum of PPFPA, recorded in $CDCl_3$ at 25°C 77

Figure 3.28 (A) ^{19}F NMR spectrum recorded in $CDCl_3$ at 25 °C and (B) ATR-IR spectrum of PPFPA. 78

Figure 3.29 ^{19}F NMR spectra recorded in $CDCl_3$ at 25°C of PPFPA of (A) before and (B) after reacting with DA and PEA to yield the various ratios of PDA_x-*co*-$PPEA_y$.....79

Figure 3.30 ATR-IR spectra of (a) PPFPA, (b) DA, (c) PEA, (d) PDA_{10}-*co*-$PPEA_{90}$, (f) PDA_{25}-*co*-$PPEA_{75}$, (g) PDA_{50}-*co*-$PPEA_{50}$, (h) PDA_{75}-*co*-$PPEA_{25}$ 80

Figure 3.31 ^{1}H spectra of PDA_x-*co*-$PPEA_y$, recorded in $CDCl_3$/acetone-d_6 (1/1, v/v) at 25°C 81

Figure 3.32 Size distribution profiles of PDA_x-*co*-$PPEA_y$, prepared in H_2O with polymer concentration (C_p) = 1.0 g/L, I indicate the light scattering intensity (LSI).....83

Figure 3.33 CMC determination by fluorescence spectroscopy using the plots of the logarithmic concentration of the micelles (mg/mL) and I_1/I_3 of (a) PDA_{10}-*co*-$PPEA_{90}$, (b) PDA_{25}-*co*-$PPEA_{75}$, (c) PDA_{50}-*co*-$PPEA_{50}$ and (d) PDA_{75}-*co*-$PPEA_{25}$.....84

Figure 3.34 The solutions of DA and (I) PDA_{10}-*co*-$PPEA_{90}$, (II) PDA_{25}-*co*-$PPEA_{75}$, (III) PDA_{50}-*co*-$PPEA_{50}$, (IV) PDA_{75}-*co*-$PPEA_{25}$ continuously stirred under air for (a) 2 h, (b) 2 d, (c) 5 d, (d) 7 d and (e) 14 d. 85

Figure 3.35 Determination of oxidation stability of free DA and PDA_x-*co*-$PPEA_y$ when continuously stirred for (a) 2 h, (b) 2 d, (c) 5 d, (d) 7 d and (e) 14 d.....86

Figure A1 DLS profiles of PM_{25}-PF_m-*20*% and PM_{50}-PF_m-*20*% as number distribution in TFE using polymer concentration (C_p) 1 mg/mL..... 104

Figure A2 DLS profile of $PMPC_{25}$ Macro-CTA in TFE using polymer concentration (C_p) 1 mg/mL 105

Figure A3 DLS profiles of PMPC macro-CTA with DPs of (a) 25, (b) 50 and (c) 100 in EtOH using polymer concentration (C_p) 1 mg/mL 105

Figure A4 DLS profiles of PM_{25}-PF_m-20% as number distribution in EtOH using polymer concentration (C_p) 1 mg/mL 106

Figure A5 DLS profiles of PM_{100}-PF_m-*20*% as number distribution in EtOH using polymer concentration (C_p) 1 mg/mL 107

Figure A6 DLS profiles as a function of LSI of PM_{50}-PFM_m and PM_{100}-PFM_m series with a variety of solid concentration 108

Figure A7 Calibration curve of PMA as a function of dye concentration in MeOH. .. 109

LIST OF TABLES

Table 2.1 The variety factors of DPs of PMPC macro-CTA, PPFPMA and total solid concentration for dispersion polymerization in EtOH.....38

Table 2.2 Composition of DA and PEA used for post-polymerization modification....41

Table 3.1 Molecular weights and molecular weight distribution of the synthesized PMPC macro-CTAs.....46

Table 3.2 The exchange ratio of PMPC:PPFMA calculated from ^{1}H NMR and UV-visible spectroscopy.....72

Table 3.3 Molecular weights and molecular weight distribution of the synthesized PPFPA.....78

Table 3.4 The compositions of DA and PEA in the polymer chain calculated from ^{1}H NMR.....82

CHAPTER I
INTRODUCTION

1.1 Theory and Literature Review

Polymeric nanoparticles are nanomaterials that have been widely utilized as nanocarriers in various applications because their functionality could be conveniently tunable. Their structures are viable and more stable than those of other self-assembled nano-objects such as surfactants [1, 2]. Polymeric nanoparticles as nanocarriers have gained much attention especially those used as carriers for drug delivery [3-5], stimuli-responsive nanoparticles [6, 7], nanosensors for the detection of harmful organic compounds [8, 9], and nanoreactors used as catalysts for organic reactions [10, 11].

In general, the self-assembly of amphiphilic copolymers which have hydrophilic and hydrophobic segments is a general approach for preparing polymeric nanoparticles. There are two categories of amphiphilic copolymers: block and random copolymers. Block copolymers have been favorably employed because of their well-defined structures [12-16]. The well-known synthetic methodology that yields copolymer with well-controlled molecular weight, molecular weight distribution, and composition is that based on controlled/living radical polymerization such as reversible addition-fragmentation chain transfer (RAFT) [17-19], and atom transfer radical polymerization (ATRP) [20-22].

Li and co-workers [23] prepared poly(oligo(ethylene glycol) methacrylate)-*block*-poly(furfuryl methacrylate) (POEGMA-*b*-PFMA) by RAFT polymerization. The diblock copolymer then was modified with *N*-octyl maleimide via Diels-Alder reaction yielding the near-infrared (NIR) photothermal nano-assembled POEGMA-*b*-POMFMA. Doxorubicin (DOX), an anticancer drug and indocyanine green (ICG), a NIR dye were encapsulated in the polymeric micelles. Faster drug release could occur upon NIR

irradiation due to photothermal effect-induced drug release and partial retro DA reaction (**Figure 1.1**).

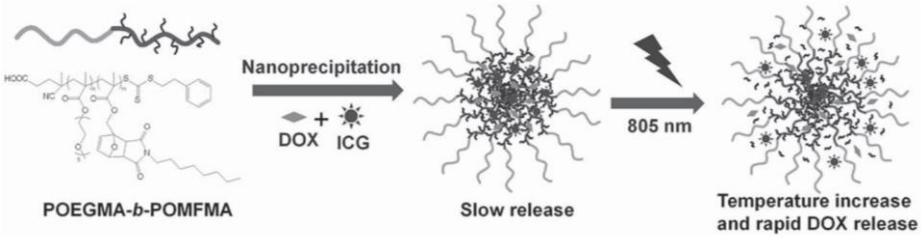

Figure 1.1 Preparation of DOX and ICG encapsulated in POEGMA-*b*-POMFMA polymeric micelles [23].

Polymeric nanoparticles can also be utilized as nanosensors to detect harmful chemical substances. Gao and co-workers [8] developed a block copolymer of poly(ethylene glycol) monomethyl ether methacrylate and polymeric ionic liquid 2-(3-methylimidazolium-1-yl) ethylmethacrylate bis-(trifluoromethanesulfonimide) (PEGMEMA-*b*-PIL-MAA). The assembled micelles from the copolymer was employed as nanosensor to detect *p*-phenylenediamine (PPD). 1-Pyrenecarboxaldehyde (Py-CHO) encapsulated inside the core of the micelles was used as a probe to detect PPD through the amine-aldehyde condensation reaction. The micelles showed high performance on PPD detection with a limit of detection as 0.007 μmol L^{-1} which was lower than those of other fluorescent probes such as organogel and fluorescent conjugated polymers (**Figure 1.2**).

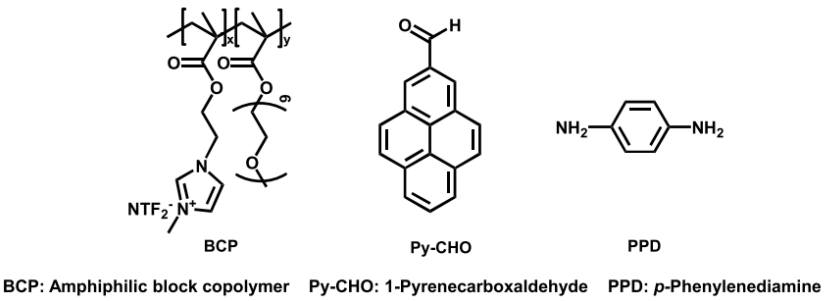

Figure 1.2 Chemical structures of amphiphilic block copolymer, 1-pyrenecarboxaldehyde (Py-CHO) as a probe, and p-phenylenediamine (PPD) as an analyte [8].

Polymeric micelles are usually prepared from amphiphilic copolymers by a conventional method based on stepwise micellar self-assembly induced by adding selective solvents. However, this method requires the elimination of solvent by dialysis or evaporation [24-26]. Only low concentration of micelles (≤1.0 wt.% solids) can be obtained from the conventional method so that it is not practical to be applied for industrial applications [27].

Polymerization-induced self-assembly (PISA) has been recently introduced as an alternative synthetic method to prepare self-assembled nanoparticles. PISA can be effectively performed via dispersion or emulsion polymerization based on controlled living radical polymerization, e.g., RAFT [28, 29] and ATRP [30, 31]. PISA is a powerful technique as it can *in situ* generate self-assembled nano-objects with a high solid content [32, 33] and tunable well-defined morphologies such as spheres, worms, and vesicles [27, 34]. In principle, a first block used as a stabilizer block is synthesized first and employed as a chain extension for the synthesis of a second core-forming block. The solvent used in this method must dissolve all components used for the synthesis of the second block. Then, nanostructures simultaneously self-assemble when the second block is long enough to decrease its solubility and induce phase separation to promote *in situ* self-assembly to form nanoparticles. Morphological transition from spheres, worms to vesicles can be determined from

“packing parameter” which is calculated by the equation: $p = v_0/a_e l_0$, where v_0 is the volume of the core-forming block, a_e is the equilibrium interface area per chain, and l_0 is the length of the core-forming block. Also, the morphological transition is dependent on the solid content, solvent, and chemical structures of both blocks.

In 2016, Gao and co-workers prepared polymeric micelles via PISA through RAFT dispersion polymerization by using biocompatible poly(ethylene glycol) (PEG) as a polymerization medium (PEG-PISA). They prepared various block copolymeric nano-objects with various stabilizer block and used polystyrene (PS) as a core-forming block such as poly[(ethylene glycol)monomethyl ether]-*block*-polystyrene (mPEG-*b*-PS). This research demonstrated that PEG-PISA system could effectively provide block copolymers with well-defined nanostructures.

Moreover, PISA has emerged as the effective tool to generate tunable polymeric nanoparticles bearing various morphologies.

Blanaz and co-workers [35] studied mechanistic insights for morphological transition of block copolymeric nano-objects (**Figure 1.3**). Block copolymes based on water-soluble poly(glycerol monomethacrylate) (PGMA) as a macromolecular chain transfer agent (macro-CTA) and poly(2-hydroxypropyl methacrylate) (PHPMA) as a core-forming block were prepared to study the mechanism of polymerization-induced morphological transformation of the nanoparticles. Sphere was observed as a starting shape. High order morphologies were observed with longer DP of PHPMA core-forming block from spheres to worms, and finally to vesicles through jellyfish as an intermediate shape.

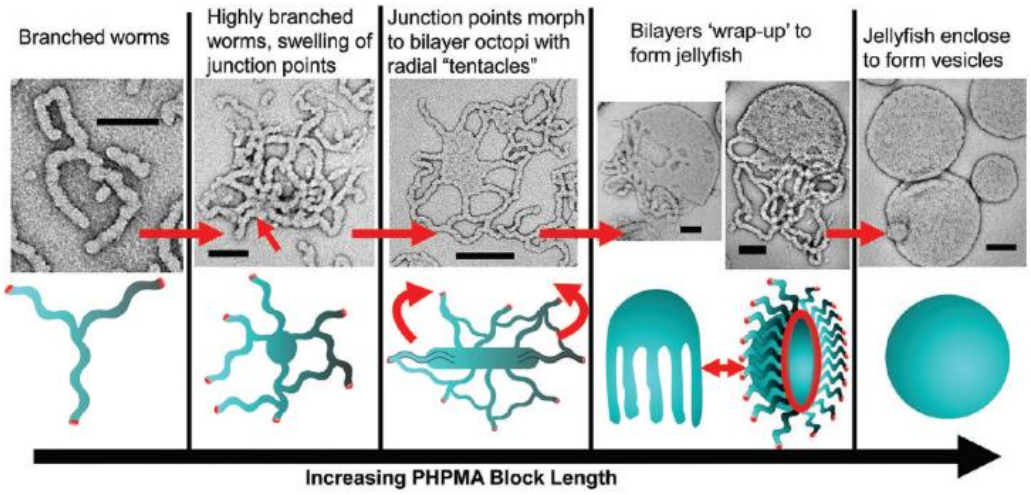

Figure 1.3 Mechanistic morphological transformation of diblock copolymeric nanostructures of PGMA-*b*-PHPMA from spheres, worms to vesicles [35].

Additionally, In 2012, Blanaz and co-workers [36] studied about morphological transition of PGMA-*b*-PHPMA by PISA through RAFT aqueous dispersion polymerization. It was found that high order morphology transition depends on 3 factors: DPs of the stabilizer and core-forming blocks, and total solid concentration. For short DPs of PGMA stabilizer block, micellar morphologies depended on only the DP of PHPMA core-forming block without the effect from total solid concentration. For morphological transformation of longer PGMA stabilizer block, the transformation depended on both the DP of PHPMA core-forming block and total solid concentration (**Figure 1.4**). However, spherical morphology was dominant when PGMA was much longer because it required a longer PHPMA core-forming block to reduce molecular curvature and *in situ* induce morphological transition.

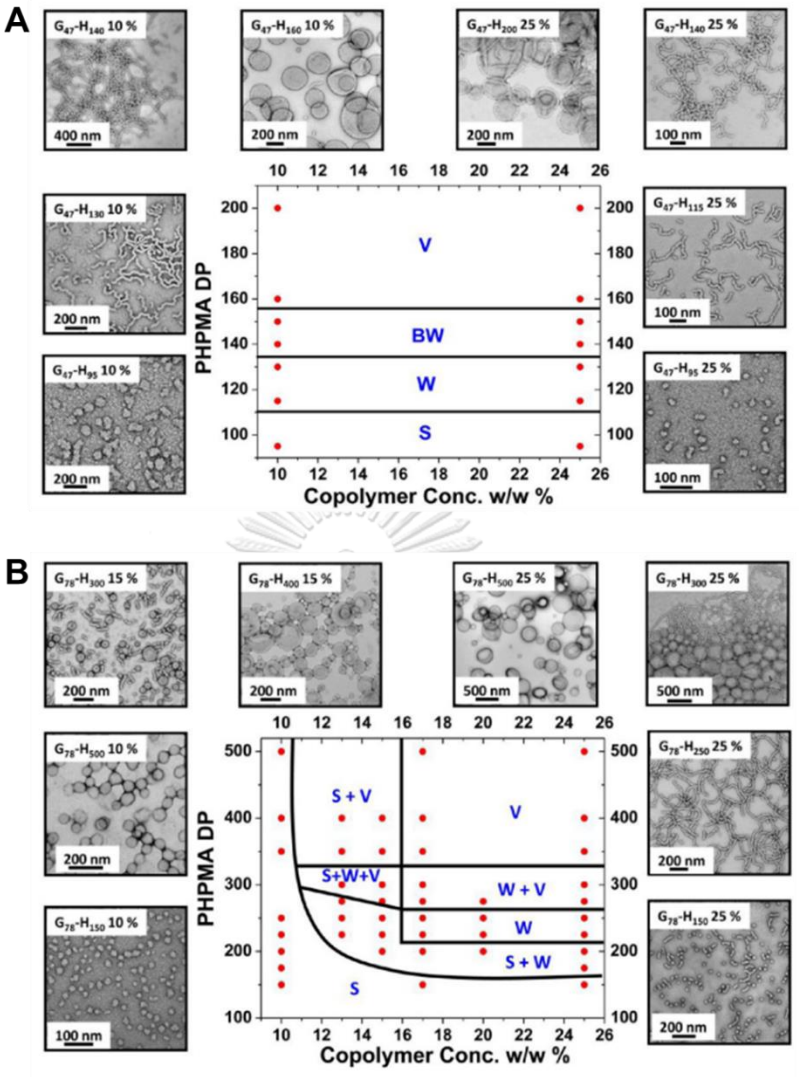

Figure 1.4 Phase diagram and TEM images of diblock copolymeric PGMA-*b*-PHPMA nanostructures of (A) series of $PGMA_{47}$-*b*-PHPMA and (B) $PGMA_{78}$-*b*-PHPMA with the variety of DP_{PHPMA} and total solid concentration [36].

PISA has been performed mostly in aqueous solution. However, organic solvents such as ethanol have also been employed.

In 2012, Semsarilar and co-workers [37] prepared various kind of block copolymers using poly(glycerol monomethacrylate) (PGMA), poly(2-(methacryloyloxy)ethyl phosphorylcholine (PMPC), poly[2-poly(dimethylamino)ethyl methacrylate (PDMA) and poly(methacrylic acid) (PMAA) as stabilizer blocks. Poly(benzyl methacrylate) (PBzMA) was synthesized as a second block via PISA

through RAFT dispersion polymerization in ethanol. Sphere, worm, and vesicle obtained from this system were dependent on DPs of stabilizer, core-forming blocks, and total solid concentration.

Polymeric nano-objects bearing multifunctionality have been usually used in advanced applications. However, it is sometimes a difficult manner to prepare multifunctional polymers because of the requirement of multiple steps and complicated procedures. Post-polymerization modification or post-functionalization of polymer precursors having active functional side groups have been widely used to generate polymers having multifunctional components [38-40]. Common chemical reactions for use in post-functionalization to modify polymer precursors include Huisgen 1,3-dipolar cycloaddition [41], Alder-ene reaction [42], thiol-*para*-fluoro substitution [43, 44], and active ester groups [45-47].

A precursor polymer having *N*-hydroxysuccinimide (NAS) was prepared from *N*-hydroxysuccinimide methacrylate in DMSO via ATRP and yield poly(acrylamide) derivatives upon post-polymerization modification as reported by Monge and co-workers [48]. PNAS was then post-modified with benzylamine as a reactive primary amine under mild condition yielding poly(*N*-benzyl methacrylate amide). However, there are some drawbacks of using NAS-based polymers because of their limited solubility in common organic solvents. Pentafluorophenyl (PFP)-based polymers (PPFP) are polymer precursors that have gained much more attention recently due to their better solubility in organic solvents and higher hydrolytic stability than the PNAS [49-51]. Having five electronegative fluorine atoms, PPFPs can be easily substituted by reactive modifiers, especially, primary amines under mild conditions [47, 52-54]. Moreover, post-polymerization modification of PPFPs can be conveniently followed by ^{19}F nuclear resonance (NMR) spectroscopy [49, 55].

In 2017, Noree and co-workers [56] prepared amphiphilic random copolymers of poly(pentafluorophenyl methacrylate)-*co*-poly(oligo(ethylene glycol methacrylamide) (PPFPMA-*co*-POEGMAM) through post-polymerization modification

of PPFPMA by oligo(ethylene glycol) methyl ether amine (OEG-NH_2) (**Figure 1.5**). The micellar formation of redox-responsive nanogel could be achieved via tandem post-polymerization modification with cystamine as a dithiol crosslinker. Moreover, isopropylamine was utilized as a reactive modifier to post-functionalize the nanoparticles to eliminate the remaining PFP groups. The redox-responsive nanoparticles showed the release profiles of the hydrophobic dye, Nile red (NR), at an accelerated rate in the presence of glutathione. These nanogels are suitable for controlled drug delivery.

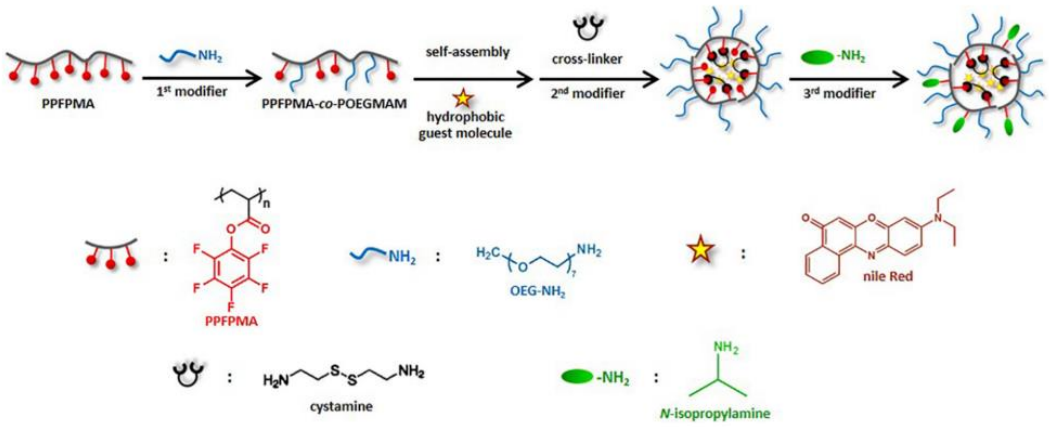

Figure 1.5 Post-polymerization modification of PPFPMA with reactive modifiers to yield the redox-responsive nanogels [56].

Because of the well-known advantages of PFP-based polymer precursors for the preparation of polymers bearing multifunctionality, some researchers have also been interested to prepare core-functionalizable nanostructures from PPFPs via PISA.

Vakili and co-workers [57] prepared thermoresponsive diblock copolymeric nano-objects by PISA through RAFT aqueous emulsion polymerization. Poly(*N,N*-dimethylacrylamide) (PDMAm) macro-CTA agent was used for the synthesis of poly(pentafluorophenyl acrylate) (PPFPA) block. Core-functionalizable polymeric nano-objects of $PDMAm_{48}$-*b*-$PPFPA_{51}$ was first prepared with a molecular weight (M_n) of 140 kg mol^{-1} and M_w/M_n of 1.25 as evaluated by GPC suggesting the well-controlled polymerization. Morphology and particle size of the self-assembled

$PDMAm_{48}$-*b*-$PPFPA_{51}$ nanostructure were found to be 481.1 ± 39.9, 458 ± 27.7 nm, and 547.5 ± 25.2 nm as determined by atomic force microscopy (AFM), transmission electron microscopy (TEM), and scanning electron microscopy (SEM), respectively. Hexamethylenediamine (HMDA) as a crosslinker was used for core-functionalization of the nano-objects. $PDMAm_{48}$-*b*-$PPFPA_{51}$ was then post-functionalized to yield nanoparticles of which diameter slightly increased from 450.1 ± 74.0 to 489.6 ± 39.9 nm as determined by DLS. Moreover, the thermoresponsive diblock copolymer was also synthesized by UV-initiated RAFT dispersion polymerization. PDMAm-*b*-P(DMAm-*co*-PFPA) macro-CTA was used for the synthesis of thermoresponsive PNIPAm via polymerization-induced thermal self-assembly (PITSA) at a temperature above lower critical solution temperature (LCST) of NIPAm (32°C) as shown in **Figure 1.6** [54, 58]. It was found that the diameter of nanoparticles increased with chain lengths of PNIPAm. And the nanoparticles can also be core-crosslinked with HMDA.

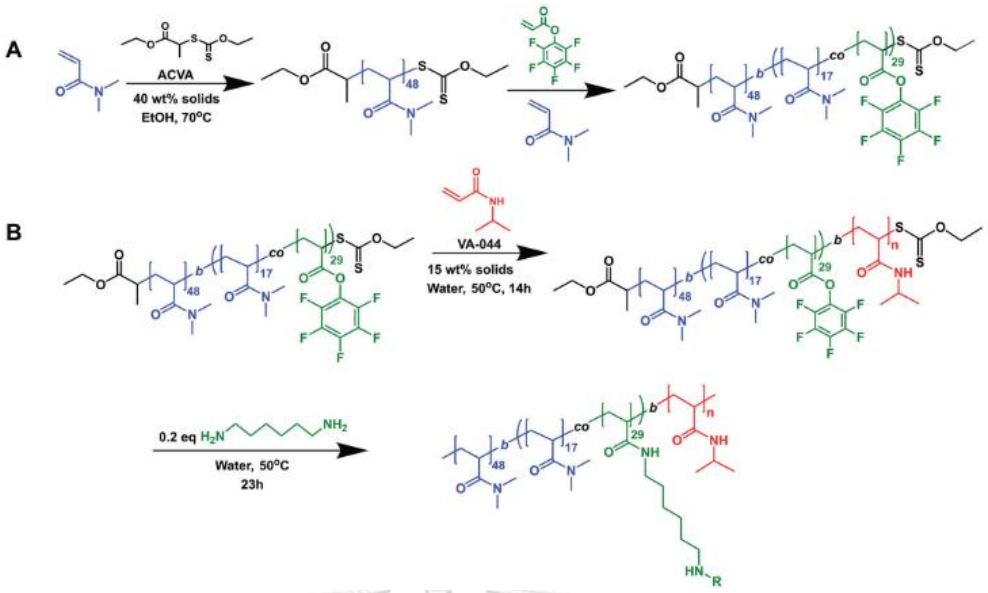

Figure 1.6 Synthetic route of (a) PDMAm-*b*-P(DMAm-*co*-PFPA) macro-CTA in EtOH, and (B) PDMAm-*b*-P(DMAm-*co*-PFPA)-*b*-PNIPAm via PITSA at 50°C in water. Thermoresponsive nano-objects were subsequently treated with HMDA [59].

The preparation of core-functionalizable nanoparticles via PISA was also reported by Couturaud and co-workers [60]. Poly(pentafluorophenyl methacrylate (PPFMA) was first prepared by RAFT-mediated photoinitiated PISA. They used PEG with DP of 113 as a macro-CTA whereas DP of PPFMA was set to be 200. The preparation of PEG_{113}-*b*-$PPFMA_x$ was performed in DMSO under visible light irradiation (405 nm) at 37°C for 4 h (**Figure 1.7**). The onset of self-assembly was found when the reaction was conducted for 0.6 h. Self-assembled PEG_{113}-*b*-$PPFMA_{200}$ (M1) was obtained with a mean diameter of 320 nm as determined by DLS in DMSO. However, spherical nanoparticles were only obtained although DPs of PPFMA and solid content were varied. The ratio of R_G/R_H = 0.783 evaluated by static light scattering (SLS) was close to the theoretical value (R_G/R_H = 0.775). R_G and R_H are radius of gyration and hydrodynamic radius, respectively. This indicated that the nanoparticles had homogeneous morphology of spheres. When they switched the solvent from DMSO to H_2O, the nanoparticles precipitated presumably via fusion mechanism. To enhance

the stability of particles in H_2O, the particles were crosslinked with ethylenediamine and cystamine to generate P1 and P2, respectively. As determined by FT-IR spectroscopy, the absence of former C=O stretching at 1780 cm^{-1} of pentafluorophenyl ester and the emergence of a new signal from C=O stretching of amide bond at 1650 cm^{-1} verified the success of cross-linking.

Redox-responsiveness of disulfide linkage-containing particles was tested using glutathione (GSH) as a reducing agent. P1 and P2 were treated by different concentrations of GSH in PBS buffer and measured the change of particle size with incubation time (h). It was expected that the particles without disulfide linkages, P1 would not show any redox responsiveness in all cases. According to the results, P2 solely showed redox responsiveness when treated with 10 mM of GSH. The Z-average diameter (nm) increased with respective incubation time (h). Cross-linked P1 and P2 nanoparticles were also tested for cytotoxicity against A549 cells. The cell viability was more than 92% indicating that P1 and P2 nanoparticles are biocompatible. These nano-objects would be great materials for drug delivery systems.

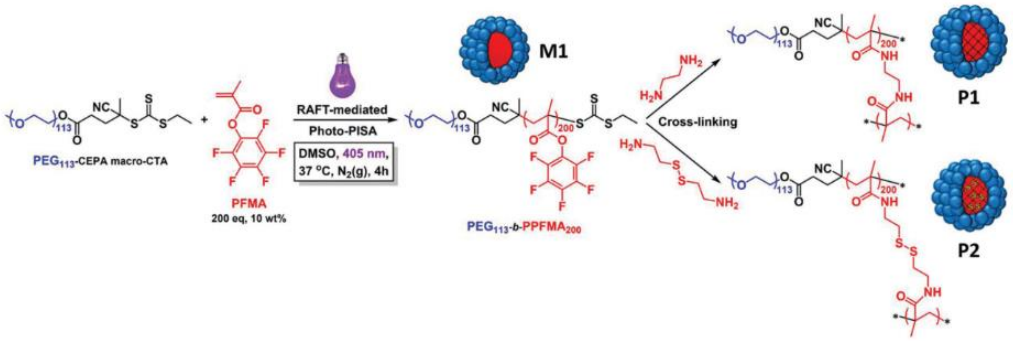

Figure 1.7 Schematic illustration of the preparation of PEG_{113}-b-$PPFMA_{200}$ by RAFT-mediated photoinitiated PISA at 37°C in DMSO and subsequently treated with ethylenediamine and cystamine to prepare P1 and for P2, respectively [60].

Poly(2-methacryloyloxyehthyl phosphorylcholine) (PMPC) is a zwitterionic polymer of which it monomeric design mimics cell membrane structure [61-63]. Owing to its highly water-solubility, biocompatibility, PMPC exhibits great antifouling property that reduces undesirable non-specific adsorption of proteins and cells [62, 64]. Moreover, PMPC can preserve biomolecules as it provides suitable environment for maintaining the stability and activity of the biomolecules [61, 65-67]. PMPC has emerged as a superior antifouling polymer to the well-known PEG whose degraded products under some conditions such as sonolytic degradation of reactive oxygen species [68] are found to be toxic to mammalian cells. There are reports on the use of PMPC as the water-soluble and biocompatible block for preparing polymeric micelles as drug carriers [69-74].

Hu and co-workers [69] prepared polymeric micelles of poly(aspatic acid)-*block*-poly(2-methacryloyloxyethyl phosphorylcholine) (PLAsp-*b*-PMPC). Redox-responsiveness was introduced by the modification of disulfide bond conjugated with tetraphenylethylene (TPE) as aggregation-induced emission (AIE) imaging providing TPE-SS-PLAsp-*b*-PMPC. The redox-responsive nano-assembly containing encapsulated anticancer drug, doxorubicin (DOX) showed highly efficient drug delivery due to its fast disassembly in the presence of GSH. The polymeric micelles could be able to be traced due to the AIE property of the conjugated TPE in the polymer chain. These smart polymeric micelles have a great potential to be further used in biomedical applications for chemotherapy and bioimaging.

PMPC has also been used to prepare polymeric micelles by PISA. Sugihara and co-workers [63] studied mechanistic morphological transformation of the block copolymers having PMPC as a chain extension. Block copolymers of PMPC and poly(2-hydroxypropyl methacrylate) (PMPC-*b*-PHPMA) were prepared via PISA through aqueous dispersion polymerization (**Figure 1.8**). A variety of morphologies, sphere, worm, and vesicle were obtained depending on the DP of the core-forming block of PHPMA (DP_{PHPMA}) and total solid concentration.

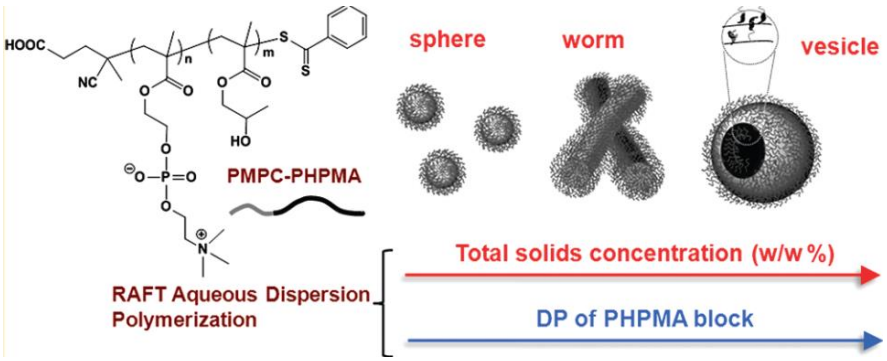

Figure 1.8 Schematic illustration of PMPC-*b*-PHPMA and morphological transition depending on DP_{PHPMA} core-forming block and total solids concentration (w/w %) [63].

Polymeric micelles prepared by PISA having PMPC shell was investigated by Noy and co-workers [70]. They prepared block copolymer of PMPC and poly(4-(*N*-(*S*-penicillaminylacetyl)amino)phenylarsonous acid) (PENAO) having conjugated with an anticancer drug as a stabilizer block and poly(methyl methacrylate) (PMMA) as a core-forming block to yield (P(MPC-*co*-PENAO)-*b*-PMMA) by PISA in mixed solvents of H_2O/EtOH. The effect of zwitterionic PMPC chain lengths on the reactivity and cytotoxicity of the drug was determined. Soft tissue sarcoma cell lines (HT1080 and SW982) were subjected to be used for cellular uptake, cytotoxicity, and reactivity studies. The antifouling characteristic of PMPC shell can protect the micelles from non-specific adsorption of proteins such as bovine serum albumin (BSA). Less cytotoxicity was found in PENAO anticancer drug conjugated in the micelles having shorter PMPC shells when compared to the unencapsulated PENAO. Moreover, PENAO activity increased with the decreasing PMPC shell.

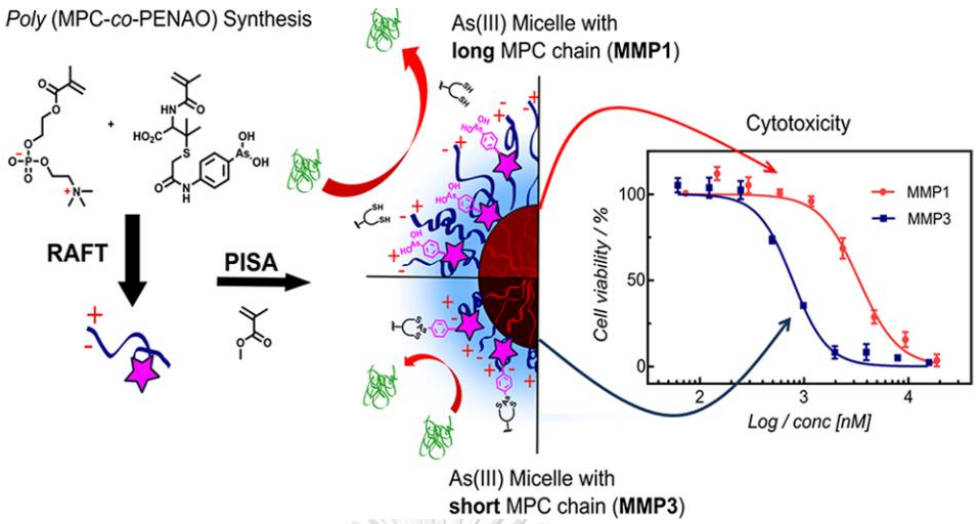

Figure 1.9 Schematic illustration of the preparation of poly(MPC-*co*-PENAO)-*b*-PMMA via PISA in H_2O/EtOH [70].

Taking advantage of PISA strategy, this research aimed to prepare of new biocompatible and core-functionalizable polymeric micelles based on block copolymers of hydrophilic PMPC and hydrophobic PFP-based polymer precursors, namely poly(pentafluorophenyl acryalate) (PPFPA) and poly(pentafluorophenyl methacrylate) (PPFPMA) to yield PMPC-*b*-PPFPA and PMPC-*b*-PPFPMA, respectively. The synthesis of these diblock copolymers is hard to be achieved via the conventional approach due to the extremely different solubility of the two blocks. PMPC is synthesized as the first block via reversible addition-fragmentation chain transfer (RAFT) polymerization which would act as a macro chain transfer agent (PMPC macro-CTA) for dispersion RAFT polymerization of PFP-based monomers that simultaneously form the core-forming block via PISA process. Effects of degree of polymerization (DP) of both PMPC and PFP-based polymers as a second block as well as solid concentrations on the morphology and size of the nanoassemblies are systematically investigated.

As core-functionalizable property of the diblock copolymer, we have interested to study post-polymerization modification using various modifiers such as fluorescent dyes to form fluorescently labeled nanoparticles. Due to the favorable

biocompatibility and antifouling characteristic of the PMPC stabilizing block, it is anticipated that these polymeric micelles would possess potential applications in the area of biotechnology and biomedicine such as bioimaging, enzymatic nanoreactors, cellular nanosensors.

Recently, reactive oxygen species (ROS), namely, hydrogen peroxide, hydroxyl radical, are the main products produced from metabolic processes such as normal cells respiration in human body [75-77]. However, overproduction of ROS mainly caused high stress cells leading to inflammable diseases [78-80]. Therefore, antioxidant compounds, such as ascorbate, glutathione, tocopherol, can act as a ROS scavenger for inflammable treatment [81]. In addition, Nagasaki group has extensively reported the synthesis of antioxidant nanoparticles for radical scavenging. TEMPO is the main pendant group to scavenge ROS species [82-84].

In particular, polyphenol derivatives are also well-known as natural radical scavenger. They are largely found in fruits, vegetables, and natural products [85]. However, some polyphenols are poorly bioavailable as a result of their low oxidation stability [86]. Therefore, the preparation of polymeric nanocarriers having conjugated polyphenol derivative is a very attractive way to fabricate antioxidant nanoparticles with improved stability. Poly(catechol) is a polyphenol derivative which has been widely used for various applications. In 1998, Dubey and co-workers prepared various kind of poly(catechol) by oxidative polymerization using peroxidase as a catalyst [87].

Polydopamine (PDA) is another polyphenol derivative which has been used for various applications especially surface coating [88, 89] because of its universal coating property. PDA was also recognized as a radical scavenger. In 2015, Hasegawa group [90] prepared antioxidant micelles from block copolymer of poly(ethylene glycol)-*b*-poly(dopamine) (PEG-*b*-PDA). They first prepared block copolymer of PEG-pyrrole as a macro chain transfer agent (macro-CTA) for RAFT polymerization of *N*-

acryloyl glycine *tert*-butyl ester. The micellar nanoparticles of PEG-*b*-PDA were obtained by deprotection of *tert*-butyl groups. This antioxidant nanoparticles showed the great ROS reduction on scavenging endogenous ROS in human umbilical vein endothelial cells. Moreover, the micelles also inhibited angiogenesis in the chicken as determined by *ex ovo* chorioallantoic membrane assay. In the same year, Hasegawa group also studied the synthesis of antioxidant nanoparticles [76]. The block of PEG was replaced by poly(*N*-acryloyl morpholine) (PAM) to synthesize the block copolymers with higher oxidation stability. The stability against auto-oxidation was found to be proportional to the catechol contents which can be varied as a function of *tert*-butyl group deprotection. The copolymer with higher catechol contents showed a better anti-angiogenic activity.

The direct preparation of polyphenol-containing polymer especially through radical polymerization is quite difficult because of its reactivity towards radical species during polymerization. Also, hydroxyl groups have to be protected before polymerization [91]. PDA was applied as a coating layer on ultrafiltration (UF) membrane. The copolymer of PMPC and poly(2-(methacryloyloxy) ethyl lipoate) (MAEL) was reduced to convert MAEL to dithio-containing units (DTMAEL) before conjugated with the coated PDA via Michael addition [92]. In another work, PDA was coupled with PMPC through H-bonding and cation-π interactions [93]. Copolymers of PMPC and PDA were synthesized and then grafted onto polyethylenimine (PEI) surface to prepare antifouling surface [94]. Herein this research, we aim to prepare PDA-containing copolymers by post-polymerization modification of the precursor polymers bearing PFP groups with appropriate nucleophilic modifiers and then fabricate PDA-containing polymeric nanoparticles for antioxidant applications.

1.2 Objectives

1. To synthesize and characterize amphiphilic diblock copolymers.
2. To prepare nanoparticles from the synthesized amphiphilic block copolymers.
3. To characterize the copolymer nanoparticles.
4. To perform post-polymerization modification of the copolymer nanoparticles by nucleophilic modifiers.
5. To synthesize and characterize the amphiphilic copolymer through post-polymerization modification for being used as an antioxidant nanoparticle.

1.2 Scope of investigation

1. Literature survey for related works.
2. To synthesize PMPC macro-CTA for being used as chain extension for the second block using controlled radical polymerization based on reversible addition-fragmentation chain transfer (RAFT) process. Target degrees of polymerization are set to be in a range of 25-100.
3. Amphiphilic diblock copolymers of PMPC-*b*-PPFPA and PMPC-*b*-PPFPMA are prepared by PISA based on RAFT dispersion polymerization. Target degrees of polymerization of PPFPA and PPFPMA are set to be in a range of 100-200.
4. To investigate morphological transition of PMPC-*b*-PPFPA and PMPC-*b*-PPFPMA as a function of DPs of PMPC, PPFPA, PPFPMA and solid concentration.
5. Selected fluorescent dye is used as a nucleophilic modifier to modify PPFPMA located in the core of micellar nanoparticles that are *in situ* self-assembled from the amphiphilic diblock copolymer of PMPC-*b*-PPFPMA.
6. To characterize the modified copolymeric nano-objects and demonstrate their potential for future applications.

7. To synthesize and characterization of PDA-containing amphiphilic copolymer by post-polymerization modification of dopamine (DA) and *o*-phosphorylethanoamine (PEA) for being used as antioxidant nanoparticles.
8. To evaluate oxidation stability of PDA-containing amphiphilic copolymer.

CHAPTER II

MATERAILS AND METHODS

2.1 Materials

Methanol (99.9%, MeOH) from KT Chemicals (Osaka, Japan), ethanol (99.5%, EtOH) from Wako Pure Chemical (Osaka, Japan) and tetrahydrofuran (99.95%, THF) from Amakasu Chemical Industries (Tokyo, Japan) were used as received. Chloroform (99.0%) was purchased from Nacalai Tesque, Inc. (Kyoto, Japan). Ultrapure water was obtained by a Milli-Q system (18.2 MΩ). Dimethyl sulfoxide (99.0%, DMSO) was purchased from Wako (Osaka, Japan). 2-Methylacryloxyethyl phosphorylcholine (MPC) was obtained from NOF corp. 4,4'-Azobis(4-cyanovaleric acid) (ACVA or V-501, ≥ 97.0%) was purchased from Santa Cruz Biotechnology, Inc. (Texas, USA). 2,2'-Azobis[2-(2-imidazolin-2-y)propane]dihydrochloride (≥ 97%, VA-044), 2,2'-azobis(4-methoxy-2,4-dimethylvaleronitrile) (≥ 95%, V-70), and triethylamine (≥ 99.0%, TEA) were purchased from Wako Pure Chemical (Osaka, Japan). 4-Cyano-4-(phenylcarbonothioylthio)pentanoic acid (CPD) was prepared according to a published procedure [64]. Pentafluorophenol (PFP, ≥ 98%) was purchased from TCI chemicals (Tokyo, Japan). Acryloyl chloride was purchased from TCI chemicals (≥ 98%) (Tokyo, Japan). Pentafluorophenyl methacrylate (PFPMA, ≥ 97%) from TCI chemicals (Tokyo, Japan) was used after the inhibitor was removed by eluting through an inhibitor remover column for removing hydroquinone and monomethyl ether hydroquinone with a column size of 17 mm × 240 mm (Sigma-Aldrich, St. Louis, Missouri, USA). 1-Pyrenemethylamine (95.0%, PMA) was purchased from Sigma-Aldrich (St. Louis, Missouri, USA). Dopamine (DA) was purchased from Sigma-Aldrich (St. Louis, Missouri, USA), 4-Dimethylaminopyridine (DMAP, > 99.0%) was purchased from TCI chemicals (Tokyo, Japan).

2.2 Characterization

^{1}H, ^{13}C and ^{19}F nuclear magnetic resonance spectroscopy (NMR) measurements were performed using a JEOL (Tokyo, Japan) JNM ECZ 400 MHz NMR spectrophotometer. Number-averaged molecular weight (M_n) and molecular weight distribution (M_w/M_n) were determined by gel permeation chromatography (GPC) system composed of a refractive index detector with phosphate buffer solutions (pH 9.0) as the eluent. The measurements were performed at 40 °C and sodium poly(styrenesulfonate) as a standard was used for calibration. The flow rate was fixed at 1.0 mL/min. All sample solutions were filtered using a 0.20-μm pore size membrane before being subjected to the relevant measurements. Dynamic light scattering (DLS) measurements were performed using a Malvern (Malvern, UK) Zetasizer nano ZS equipped with He-Ne laser (4mW at 632.8 nm) at 25 °C. The sample solutions for light scattering experiments were filtered through 0.45 and 1.0 μm pore-size membranes. Analysis by infrared (IR) spectroscopy was performed using a Jasco (Tokyo, Japan) FT/IR-4200 by the attenuated total reflection (ATR) technique. Transmission electron microscopy (TEM) was performed using a JEOL (Tokyo, Japan) JEM-2100 with an accelerating voltage of 160 kV. Samples for TEM observation were prepared on a copper grid coated with thin films of Formvar and carbon and were then stained with sodium phosphotungstate before being dried under vacuum overnight. UV-Vis spectra were recorded on an Agilent 8453 in a quartz cell with 1 cm path length.

2.3 Methods

2.3.1 Synthesis of pentafluorophenyl acrylate (PFPA) monomer

Pentafluorophenol (PFP) (25.0 g, 0.136 mol) was dissolved in 100.0 mL of distilled $CHCl_3$ under inert atmosphere (Ar) at 0 °C. Triethylamine (TEA) (16.5 g, 0.163 mol) was

pre-dried using Na_2SO_4 for overnight and added dropwise to the cooled reaction mixture. Acryloyl chloride (AC) (14.7 g, 0.163 mol) and 0.10 g of 2,6-di-*tert*-butyl cresol as an inhibitor were then added dropwise to the solution under stirring under Ar for 3 h in an ice bath. The reaction was monitored by TLC using hexane/EtOAc 80:20 as a mobile phase. After the reaction, yellow precipitate in the solution was obtained. The mixture was extracted with a saturated brine solution containing NaCl to eliminate TEA. The reaction mixture was filtered and dried with Na_2SO_4 for 1 h before the organic phase was concentrated by an evaporator providing the crude yellow solution. The crude product was then be purified by column chromatography using hexane as a mobile phase. The pure product was characterized by ^{1}H, ^{19}F-NMR and ^{13}C-NMR spectroscopy.

Figure 2.1 Synthesis of PMPC macro-CTA via RAFT polymerization

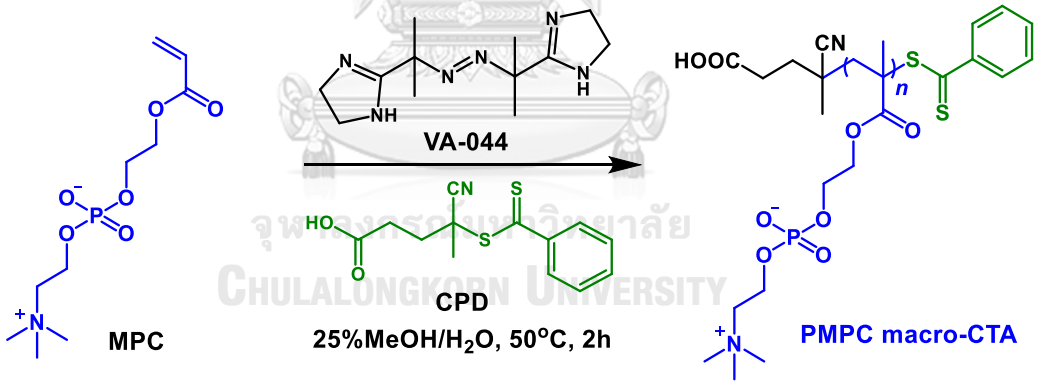

2.3.2 Synthesis of PMPC macro-CTA

Targeted degrees of polymerization (DPs) of PMPC macro-CTA were set to be 25, 50 and 100 which was synthesized by the following protocol **(Figure 2.1)**: *For targeted DP of 25*, MPC (7.38 g, 25 mmol, 25 eq), VA-044 (162.0 mg, 0.5 mmol, 0.5 eq) and CPD (279.4 mg, 1.0 mmol, 1.0 eq) were dissolved in 25 mL of the mixed

solvent of 25% (v/v) MeOH in water. *For targeted DP of 50*, MPC (7.38 g, 25 mmol, 50 eq), VA-044 (81.0 mg, 0.25 mmol, 0.5 eq), and CPD (139.7 mg, 0.5 mmol, 1.0 eq) were dissolved in 25 mL of the mixed solvent of 25 % (v/v) MeOH in water. And *for targeted DP of 100*, MPC (7.38 g, 25 mmol. 100 eq), VA-044 (40.0 mg, 0.125 mmol, 0.5 eq) and CPD (70.0 mg, 0.25 mmol, 1.0 eq) were also dissolved in 25 mL of the mixture of H_2O with 25% MeOH solution. After degassing by dispersing with Ar for 20 min, the mixture was put into an oil bath and continuously stirred at 50°C for 2 h. The reaction was stopped by quenching in an ice bath. %Conversion was calculated from ^{1}H-NMR data. M_n and dispersity (M_w/M_n) were determined by GPC.

Figure 2.2 Synthetic route of PMPC-*b*-PPFPA via RAFT dispersion polymerization

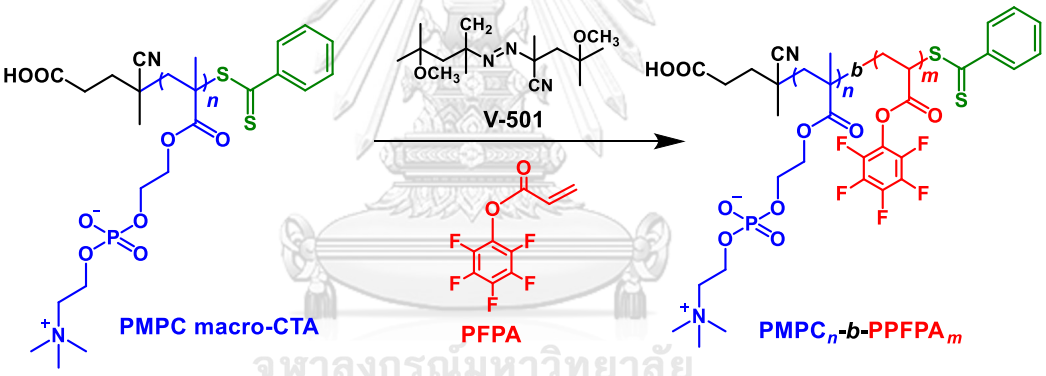

2.3.3 Dispersion polymerization of PPFPA using PMPC macro-CTA

Targeted DP of PPFPA was set to be 100 which was synthesized by the following protocol **(Figure 2.2)** to finally yield $PMPC_n$-*b*-$PPFPA_m$-*x*% (PM_n-PF_m-*x*%): pentafluorophenyl acrylate (PFPA) (1.19 g, 5 mmol, 100 eq), 4,4'-azobis(4-cyanovaleric acid) (V-501) as an initiator (7.0 mg, 25 µmol, 0.5 eq) and PMPC macro-CTA (0.4347 g, 50 mmol, 1.0 eq) were dissolved in 5.0 mL of 2,2,2-trifluoroethanol (TFE) or EtOH as a solvent. The mixed solution of 1 mL was added to an NMR tube. After that, the sample was degassed by dispersing with Ar for 5 min of each sample.

The mixture was put in an oil bath at 70°C (for the reaction performed in TFE and EtOH) and 40°C (for the reaction performed in EtOH) for a desired time interval. The reaction was stopped by quenching in an ice bath subjected to ^{1}H-NMR analysis to determine the percentage conversion of polymerization. The same procedure was also applied for the synthesis of the copolymers from PMPC macro-CTA having other DPs and different solvents.

Figure 2.3 Synthetic route of PMPC-*b*-PPFPMA via RAFT dispersion polymerization

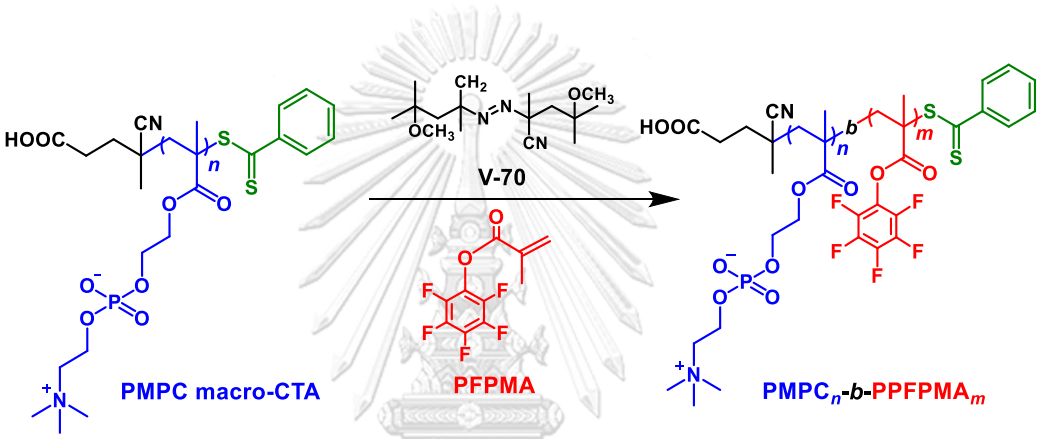

2.3.4 Dispersion polymerization of PFPMA using PMPC macro-CTA

Targeted DP of PPFPMA was set to be 200 with various total solid content (*x*%) to finally yield PMPC$_n$-*b*-PPFPMA$_m$-*x*% (PM$_n$-PFM$_m$-*x*%). PMPC$_{50}$-*b*-PPFPMA$_{200}$-19% was synthesized by the following protocol **(Figure 2.3)**: PFPMA (1.26 g, 5 mmol, 200 eq), V-70 (1.93 mg, 0.0125 mmol, 0.25 eq), and PMPC macro-CTA (0.66 g, 0.05 mmol, 1.0 eq of CTA) were dissolved in 5.0 mL EtOH. The mixed solution of 1 mL was added to an NMR tube. After that, the sample was degassed by dispersing with Ar for 5 min. The mixture was left in an oil bath at 40°C for a designated time interval. The reaction was stopped by quenching in an ice bath and subjected to ^{1}H-NMR analysis to determine the percentage conversion of polymerization. The same procedure was

also applied for the synthesis of the copolymers from PMPC macro-CTA having other DPs and different solid contents as investigated in **Table 2.1**.

Table 2.1 The variety factors of DPs of PMPC macro-CTA, PPFPMA and total solid concentration for dispersion polymerization in EtOH

DP of PMPC (*n*)	DP of PPFPMA (*m*)	Solid concentration (*wt*%)
50 **100**	Up to 200	2, 5, and 20%

Total solid concentration of polymer solution during dispersion polymerization can be calculated using **Equation 1 (Eq. 1)**.

$$\text{Total solid concentration } (wt\%) = \frac{\textbf{Macro CTA (g)+Monomer for second block (g)}}{\textbf{All reaction mixture (g)}} \times 100 \quad \textbf{Eq. 1}$$

2.3.5 Post-polymerization modification of $PMPC_n$-*b*-$PPFPMA_m$ by 1-pyrenemethylamine

Figure 2.4 Post-polymerization modification of $PMPC_n$-*b*-$PPFPMA_m$ with 1-pyrenemethylamine (PMA)

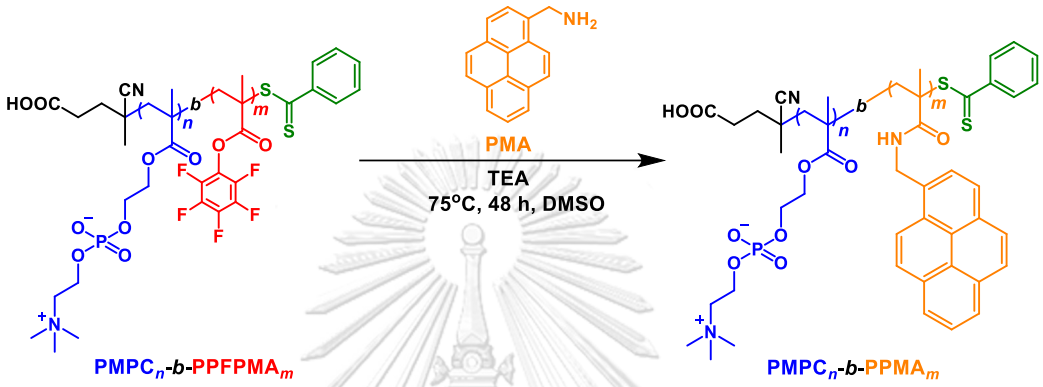

For modification reaction (**Figure 2.4**): $PMPC_{100}$-*b*-$PPFMA_{61}$ (20.0 mg, 0.02 mmol of PFPMA) was used as a model for post-polymerization modification. 1-pyrenemethylamine (PMA) (40.2 mg, 0.15 mmol) and TEA (15.3 mg, 0.15 mmol) were used as a modifier and base catalyst, respectively. All reactants were dissolved in 10.0 mL of DMSO. The molar ratio of [PFPMA unit in the polymer]/[PMA]/[TEA] was 1/5/5. The mixture was heated at 75°C for 48 h. The mixture was then purified by dialysis against MeOH and H_2O for 2 days each. The product was dried by freeze-drying to finally yield the pale-yellow powder (50.2 mg, 83%). Dye loading can be calculated using **Equation 2**:

$$\text{Dye loading content (mg/g)} = \frac{Weight\ of\ dye\ loaded\ in\ micelles\ (mg)}{Weight\ of\ dye{-}loaded\ in\ micelles\ (g)} \qquad \textbf{Eq. 2}$$

2.3.6 Synthesis of PPFPA by RAFT polymerization

Figure 2.5 Synthetic route of PPFPA by RAFT polymerization followed by post-polymerization modification to prepare antioxidant nanoparticles

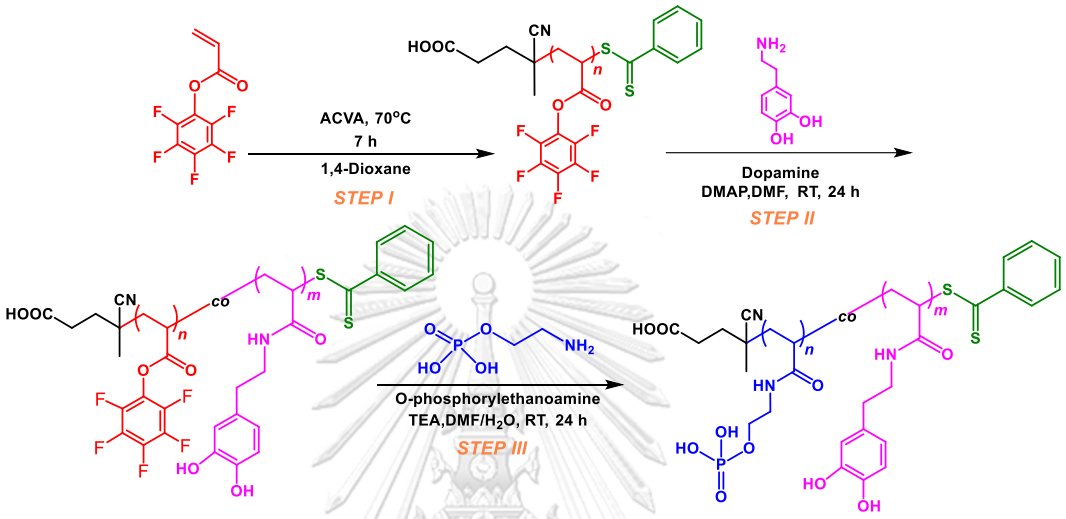

PPFPA was synthesized by RAFT polymerization of which targeted DP was set to be 100 (**Figure 2.5, step I**). PFPA (1.65 g, 10 mmol, 100 eq), CPD (27.9 mg, 0.1 mmol, 0.1 eq), ACVA (7.0 mg, 0.025 mmol, 0.025 eq) were dissolved in 5 mL of 1,4-dioxane as a solvent. After being degassed by dispersing with N_2 for 30 min, the mixture was left in an oil bath and continuously stirred at 70°C for 7 h. %Conversion, M_n and DP were calculated from ^{1}H-NMR data.

2.3.7 Post-polymerization modification of PPFPA

PPFPA was then used as a polymer precursor for preparing antioxidant nanoparticles by sequential post-polymerization modification with varied composition (**Table 2.2**) of dopamine (DA) and *o*-phosphorylethanoamine (PEA), which act as nucleophilic modifiers (**Figure 2.5, step II and step III**).

Table 2.2 Composition of DA and PEA used for post-polymerization modification

Feed ratio (%)	
DA	PEA
10	90
25	75
50	50
75	25

For 10% of DA, PPFPA (200 mg, 0.84 mmol, 100 equiv of PFPA group), DA (15.9 mg, 0.084 mmol, 10 equiv), DMAP (10.3 mg, 0.084 mmol, 1.0 equiv) as a base catalyst were dissolved in DMF as a solvent. The mixture was continuously stirred for 24 h at room temperature. After post-functionalization, the crude was purified by dialysis in acetone for 3 days to yield PDA_{10}-*co*-$PPFPA_{90}$. PDA_{10}-*co*-$PPFPA_{90}$ was then post-modified with the excess amount of PEA as follows: PDA_{10}-*co*-$PPFPA_{90}$ (100 mg, 0.38 mmol, 90 eq of PFPA group), PEA (0.24 g, 1.68 mmol, 180 eq), TEA (0.17 g, 1.68 mmol, 180 eq) were dissolved in the mixture of 10% (v/v) H_2O/DMF. The reaction was also continuously stirred at room temperature for 24 h. The product was purified by dialysis in DI for 3 days and dried by lyophilization. The product was characterized by ^{1}H NMR and ATR-IR spectroscopy. The compositions of DA and PEA substituted at PFP-entities in the polymer chain were calculated by relative integration of characteristic peaks of DA and PEA. The same procedure was also applied for the synthesis of the copolymers of other compositions.

2.3.8 Determination of critical micelle concentration

The critical micelle concentration (CMC) was determined by fluorescence spectroscopy using pyrene as a hydrophobic probe. A 10 µL aliquot of pyrene dissolved in acetone was added to 1.0 mL of the polymer solution with the

concentration of polymeric micelles in a range of 10 – 1000 μg/mL. The polymer solutions were sonicated at 60°C for 3 h and then shaken overnight at room temperature. The samples were determined by emission spectra by fixing the excitation wavelength at 334 nm. Excitation spectra were recorded from 350 – 450 nm. The intensity ratios of the third at 392 nm and the first peaks at 373 nm (I_3/I_1) were plotted against the logarithm concentration of micelles (mg/mL) to determine the CMC.

2.3.9 Oxidation stability of PDA_x-*co*-$PPEA_y$ micelles

The oxidation stability of PDA_x-*co*-$PPEA_y$ micelles when directly exposed to air was determined by UV-vis spectroscopy. The polymeric micelles with a concentration of 1.5 mg/mL of were dissolved in PBS buffer (pH 7.4) and continuously stirred under air for 2 h, 2 d, 5 d, 7 d and 14 d. UV-vis spectra of each sample were recorded in a wavenumber range of 200 – 600 nm.

CHAPTER III
RESULTS AND DISCUSSION

3.1 Synthesis of PMPC macro-CTA

PMPC macro-CTAs having targeted DPs of 25, 50 and 100 were synthesized via RAFT polymerization at 50°C in the mixed solvents of 25% (v/v) MeOH in water for 2 h (**Scheme 2.1**). All PMPC macro-CTAs were characterized by ^{1}H NMR spectroscopy of which ^{1}H NMR spectra are shown in **Figure 3.1**. The characteristic proton signals appearing at 0.8 – 1.1 ppm (peak *e*) and 1.9 ppm (peak d) attributed to CH_3 and CH_2 of polymer backbone, respectively. The proton signal of peak *m* at 3.1 ppm is assignable to the methyl groups of quaternary amine ($(C\underline{H}_3)_3$-N^+). The signals around 3.6 – 4.3 ppm belong to α-methyl of phosphoryl group (peak *a, k*), ester bond (peak *b*) and quaternary amine (peak *l*) of PMPC side group. An appearance of signals from aromatic protons (peak *f, g, h*) suggested the presence dithiobenzoate group at the chain end of PMPC macro-CTA.

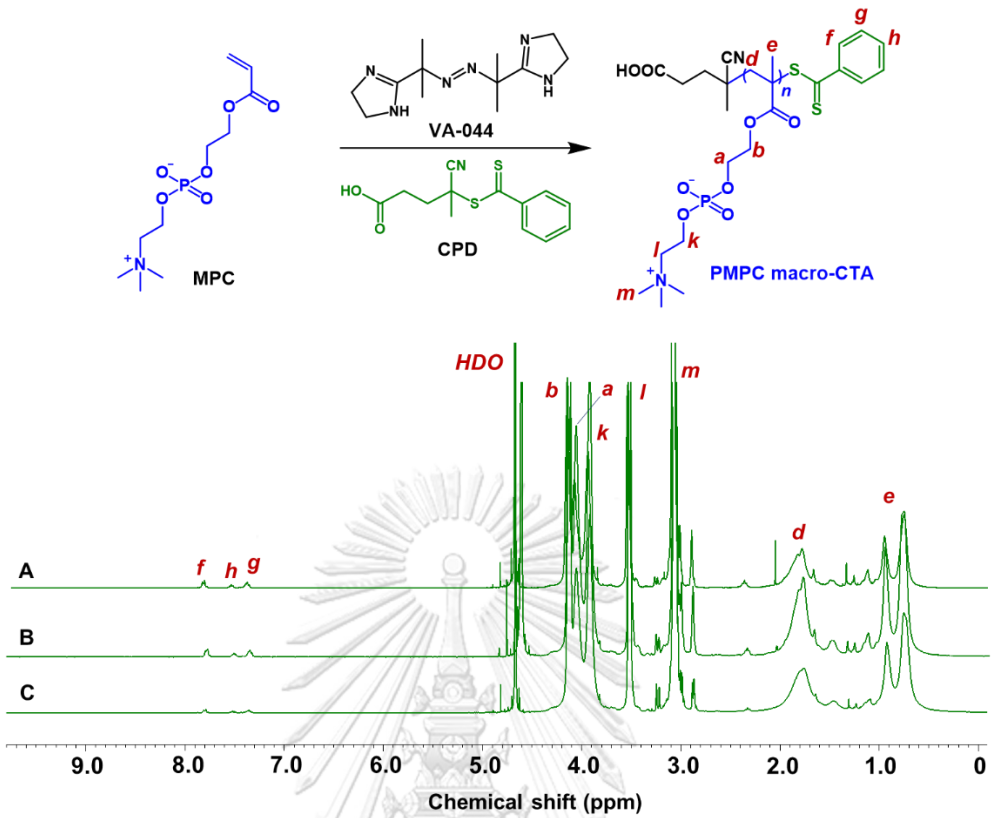

Figure 3.1 ^{1}H-NMR spectra of PMPC macro-CTAs having DP of (A) 25, (B) 50, and (C) 100.

Theoretical molecular weight ($M_{n.Th}$) of PMPC macro-CTA was calculated using **Equation 3.1.**

$$M_{n,Th} = \frac{[monomer] \times M_{w,monomer}}{[CTA]} \times conversion + M_{w,CTA} \quad \textbf{(3.1)}$$

The molecular weight of PMPC macro-CTA was calculated from the ^{1}H-NMR data ($M_{n.NMR}$) using **Equation 3.2**.

$$M_{n,\,NMR} = \frac{\int H_l \,/\, 2}{\int H_{f,g,h} \,/ 5} + M_{w,CTA} \quad \textbf{(3.2)}$$

where H_l are the protons at position *l* corresponding to PMPC side chain and $H_{f,g,h}$ are the protons of dithioester end-group at the position *f,g,h* appearing in the ^{1}H-NMR spectrum (**Figure 3.1**).

GPC traces of all PMPC macro-CTAs shown in **Figure 3.2** appearing as single peaks together with molecular weight distribution values of less than (M_w/M_n) < 1.5 suggested that the RAFT polymerization was well-controlled. The fact that the M_n values calculated from ^{1}H NMR and GPC are in good agreement with the theoretical values $M_{n,Th}$ (**Table 3.1**) also supports the assumption.

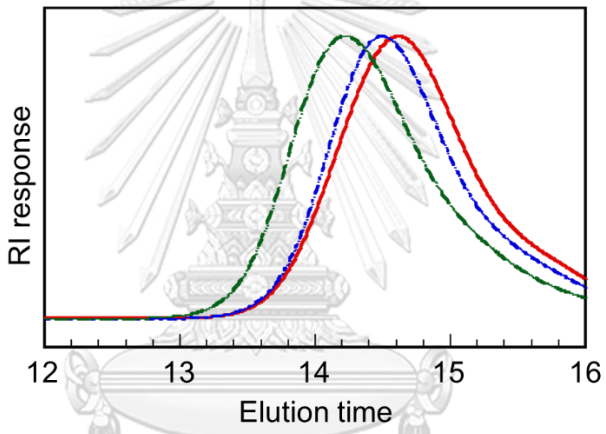

Figure 3.2 GPC traces of PMPC macro-CTA DP_{25} (—), DP_{50} (----) and DP_{100} (----)

Table 3.1 Molecular weights and molecular weight distribution of the synthesized PMPC macro-CTAs.

Target DP	*%Conversion*	$M_{n,\ Th}$ × 10^4 (g/mol)	$M_{n,\ NMR}$ × 10^4 (g/mol)	$M_{n,\ GPC}$ × 10^4 (g/mol)	M_w/M_n
25	100	0.77	0.87	0.78	1.14
50	100	1.50	1.33	1.25	1.10
100	100	2.98	3.00	1.49	1.32

$M_{n.Th}$ = Theoretical number-averaged molecular weight

$M_{n,\ NMR}$ = Number-averaged molecular weight determined from ^{1}H NMR data

$M_{n,\ GPC}$ = Number-averaged molecular weight determined by GPC

M_w/M_n= Molecular weight distribution determined by GPC

3.2 Dispersion polymerization of PPFPA using PMPC macro-CTA

3.2.1 Synthesis of PFPA monomer

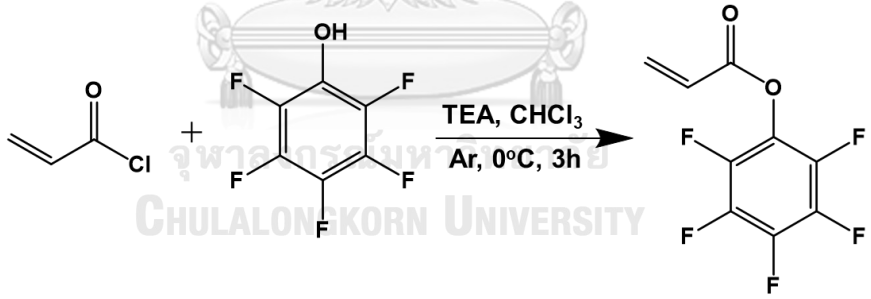

Figure 3.3 Synthesis of PFPA monomer

PFPA was synthesized via substitution reaction of acryloyl chloride and pentafluorophenol (PEP) in $CHCl_3$ under inert atmosphere (Ar) at 0°C for 3 h in the presence of TEA as a base catalyst. The crude product was purified by column chromatography using hexane as an eluent. 1.23 g of PFPA was obtained with 38% yield. The pure PFPA was then characterized by ^{1}H, ^{13}C and ^{19}F NMR of which spectra are shown in **Figure 3.4**. As anticipated, the peaks of methylene protons of alkene

appeared at 6.2 - 6.8 ppm in the ^{1}H NMR spectrum, ^{13}C NMR was also used to confirm the success of PFPA synthesis that showed the characteristic peaks (*a, b*) of carbon atoms of alkene at 125.1 – 131.5 ppm. The carbons of the fluorophenyl ring appeared at 136.6 – 142.9 ppm. The carbonyl peak appeared at 162.1 ppm. Besides, ^{19}F NMR spectrum showed the peaks of fluorine signals at -162.8, 158.3, and -152.6 ppm attributable to fluorine atoms of the pentafluorophenyl ring.

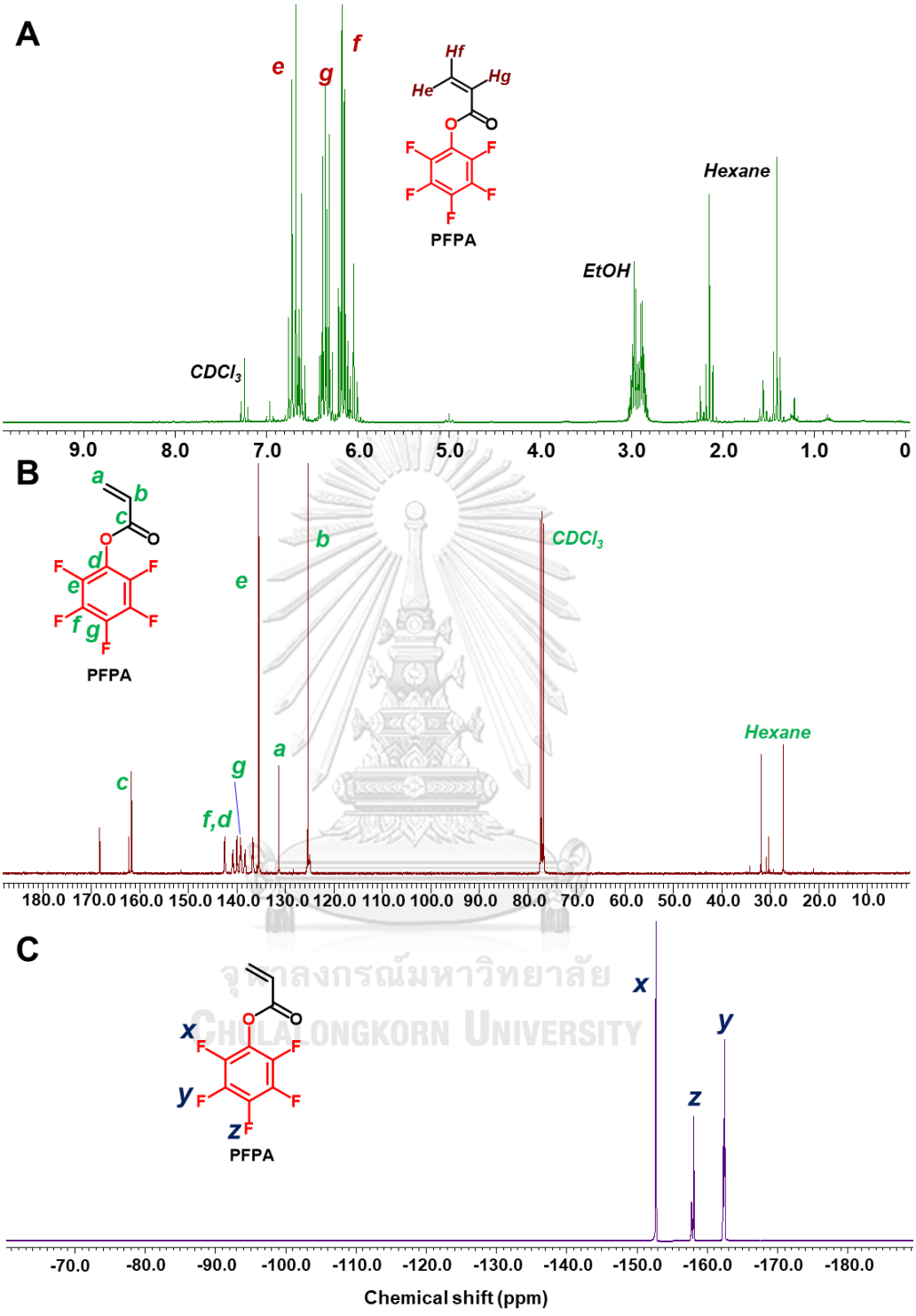

Figure 3.4 NMR spectra of PFPA monomer: (A) ^{1}H NMR, (B) ^{13}C NMR, and (C) ^{19}F NMR

3.2.2 Synthesis of PMPC-*b*-PPFPA in 2,2,2-trifluoroethanol

In PISA process, PMPC macro-CTA and the monomer, PFPA have to be soluble in the same solvent. 2,2,2-trifluoroethanol (TFE) can dissolve PMPC macro-CTA and PFPA monomer while the polymer of PFPA (PPFPA) cannot dissolve and decreases its solubility to form micelles *in situ*. A series of the block copolymer, $PMPC_n$-*b*-$PPFPA_m$ with different solid concentration (*x*%) (PM_n-PF_m-*x*%) were first synthesized in TFE at 70°C. PMPC macro-CTA with DP_{25} and DP_{50} were first selected for the synthesis of block copolymer via PISA.

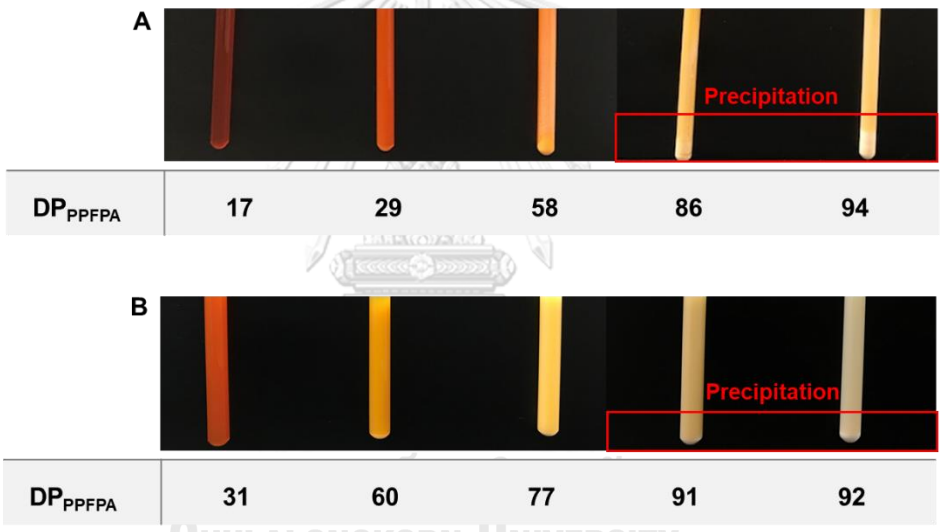

Figure 3.5 Solutions of (A) PM_{25}-PF_m-*20*%, and (B) PM_{50}-PF_m-*20*% performed in TFE

For the system of PM_{25}-PF_m-*20*%, the polymer solution became turbid with increasing DP_{PPFPA}. However, precipitation of the polymer solutions occurred at the late stage of the reaction at DP_{PPFPA} of 86 and 94. Upon increasing the DP_{PMPC} stabilizer block, the PM_{50}-PF_m-*20*% solution became precipitated at DP_{PPFPA} of 91 and 92 suggesting that the well-dispersed polymeric nanoaggregates were not formed.

A kinetic study investigated a relationship between monomer conversion and polymerization time as shown in **Figure 3.6A**. Semi-logarithmic plots of the two series are also shown in **Figure 3.6B**.

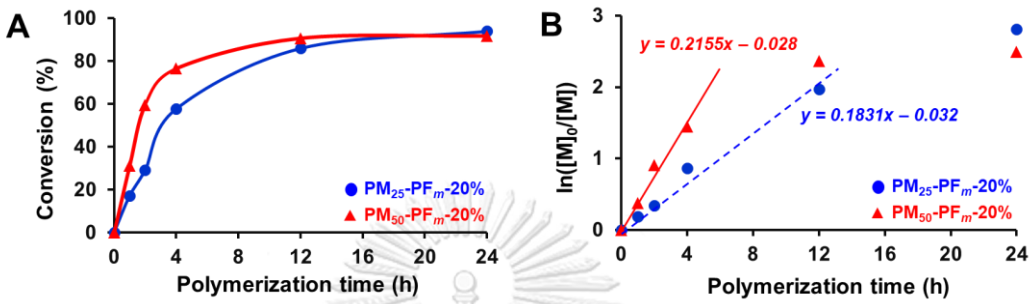

Figure 3.6 (A) A plot of monomer conversion as a function of polymerization time and (B) pseudo-first-order polymerization kinetics of PM_{25}-PF_m and PM_{50}-PF_m series with 20% solid concentration

According to the kinetic study, the highest monomer conversion of the two series reached the maximum at almost 100% within 24 h. The semi-logarithmic plots showed linear trends from the beginning of polymerization within 4 h for PM_{25}-PF_m-20% and 12 h for PM_{25}-PF_m-20%. These results implied that the polymerization of the two systems was not well-controlled at the later stage of the reaction presumably due to the phase separation of the resulting block copolymers as evidenced from the precipitation (**Figure 3.5**). Particle size and size distribution of the polymeric micelles at all polymerization time intervals was also monitored by DLS (**Figure 3.7**). For the series of PM_{25}-PF_m-20% (1st column), the particle size distribution was relatively broad at low DP of the core-forming PPFPA block (m = 17, 29) implying that the micelles are not homogeneous in size. The PDI became lower once the PPFPA block length became longer than the PMPC block length (m > n). TEM images in the second column of **Figure 3.7** revealed that the micelles of the PM_{25}-PF_m-20% are spherical in shape.

P_{25}-PF_m-20%		P_{50}-PF_m-20%
DLS	TEM	DLS
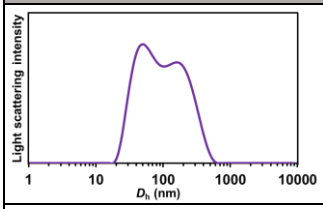	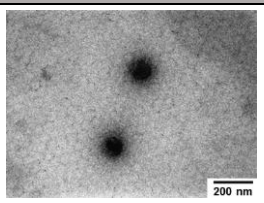	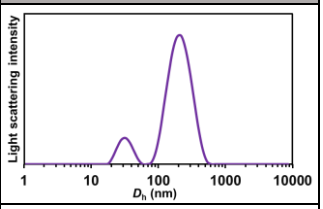
Size = 62.7 ± 1.2	Size = 117.3 ± 56.1	Size = 124.8 ± 4.6
m = 17,		m = 31,
PDI = 0.460 ± 0.009, LSI = 3,702 kcps	-	PDI = 0.413 ± 0.057, LSI = 12,262 kcps
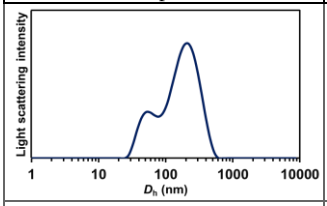	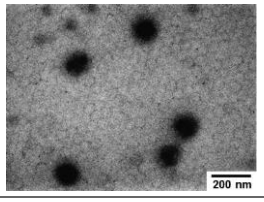	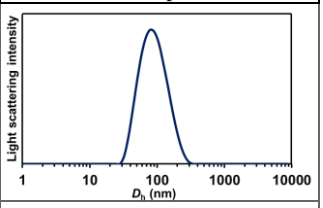
Size = 122.5 ± 4.9	Size = 211.1 ± 52.8	Size = 79.8 ± 0.7
m = 29,		m = 60,
PDI = 0.295 ± 0.015, LSI = 26,219 kcps	-	PDI = 0.176 ± 0.015, LSI = 22,445 kcps
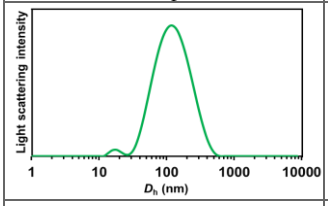	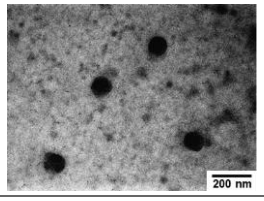	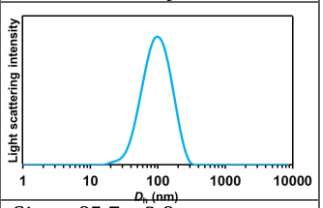
Size = 99.0 ± 3.0	Size = 144.2 ± 50.0	Size = 85.7 ± 2.8
m = 58,		m = 77,
PDI = 0.245 ± 0.015, LSI = 37,054 kcps	-	PDI = 0.144 ± 0.080, LSI = 26,759 kcps
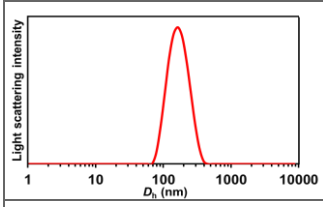	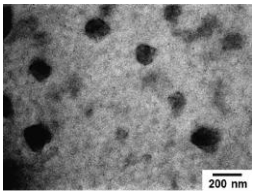	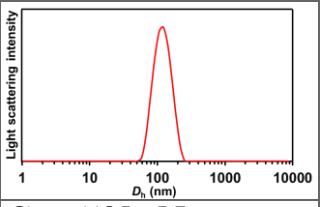
Size = 156.7 ± 1.6	Size = 160.9 ± 32.3	Size = 116.5 ± 5.7
m = 94,		m = 92,
PDI = 0.130 ± 0.042, LSI = 97,842 kcps	-	PDI = 0.116 ± 0.051, LSI = 64,143 kcps

Figure 3.7 DLS profiles and TEM images of PM_{25}-PF_m-*20*% and DLS profiles of PM_{50}-PF_m-*20*% in TFE at C_p = 1 mg/mL.

The micelles assembled from the series of PM_{50}-PF_m-20% had relatively narrow size distribution (PDI < 0.2) when the length of PPFPA block was equal to or larger than that of PMPC block. This also indicates the strong impact of the core-forming PPFPA which is the main driving force of self-assembly during PISA. It should be observed that light scattering intensity values (LSI) at all conditions are relatively high suggesting that there were large quantity of the micelles in solution. Since DLS profiles as a function of light scattering intensity (LSI) of some conditions were not unimodal distribution. Therefore, DLS profiles as a function of number distribution (**Figure A1**) were investigated instead to observe the relationship between mean particle diameters and DP_{PPFPA}. As shown in **Figure 3.8**, the diameter of the particles tended to increase as a function of DP_{PPFPA}. Nevertheless, the relationship is not exactly linear which may be explained as a result of uncontrolled PISA and inter-micellar aggregation.

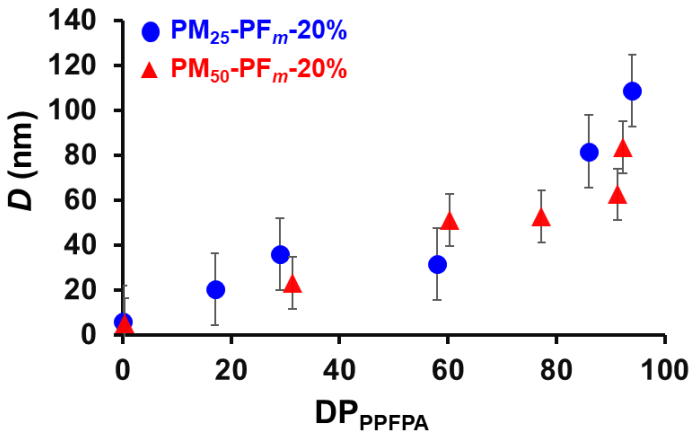

Figure 3.8 The relationship between mean diameter of the particles and DP_{PPFPA} of (A) PM_{25}-PF_m-*20%* and (B) PM_{50}-PF_m-*20%* determined by DLS at C_p = 1 mg/mL

As shown in **Figure 3.7**, TEM images indicate that all micelles in the series of PM_{25}-PF_m-20% were spherical. Morphological transition as a function of DP_{PPFPA} was not observed. It was found that the $PMPC_{25}$ macro-CTA alone also aggregate in TFE with the mean diameter as about 182 nm and LSI as 3,125.4 kcps. (**Figure A2**). It

was suspected that this behavior may prevent morphological transition. For this reason, an alternative solvent may be used to overcome this limitation. Ethanol was chosen as an alternative solvent because it can dissolve all reactants including PFPA monomer. More importantly, PMPC macro-CTA of all DPs were in unimer state as shown in DLS profiles (**Figure A3**) with low LSI values implying that PMPC macro-CTA did not aggregate in ethanol. Therefore, ethanol was a suitable solvent for PISA.

3.2.3 Synthesis of PMPC-*b*-PPFPA in ethanol

The reactions were performed at 70°C in ethanol using PMPC macro-CTA DP_{25}. The polymer solutions became precipitated at all time points suggesting poorly controlled polymerization as shown in **Figure 3.9**.

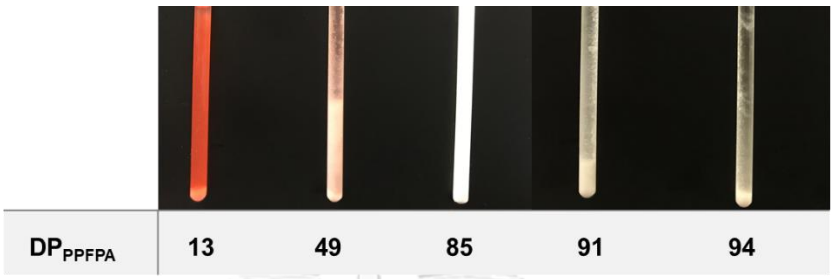

Figure 3.9 Polymer solutions of PM_{25}-PF_m-*20*% prepared in ethanol

A kinetic study was also monitored by ^{1}H NMR spectroscopy. Monomer conversion dramatically increased from 0 to 5 h (**Figure 3.10A**). After that, the polymerization rate gradually increased until reaching 100% at 24 h. Linear pseudo-first-order polymerization kinetics was observed up to 5 h (**Figure 3.10B**) suggesting the polymerization was not well-controlled beyond 5 h. This agrees well with the fact that precipitation of solutions was observed during PISA, particularly at the late stage of polymerization.

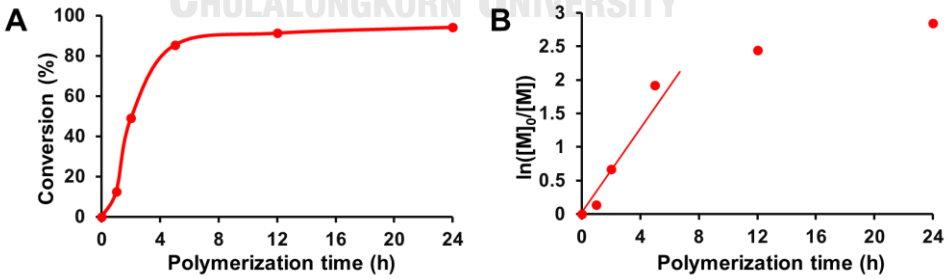

Figure 3.10 (A) A plot of monomer conversion vs polymerization time and (B) pseudo-first-order polymerization kinetics of PM_{25}-PF_m-*20*% series in EtOH

According to DLS profiles of this condition investigated as the size distribution of LSI function (**Figure 3.11**), size distributions of PM_{25}-PF_m-*20*% showed bimodal

distributions, indicating that the micellar formation was not well-formed due to precipitation during polymerization. The evolution of particle size against DP_{PPFPA} of this condition was also found to be irregular implying the uncontrolled polymerization (**Figure 3.12**). In addition, the mean diameter of particles as a function of number distribution dramatically increased at DP_{PPFPA} from 13 to 49 and went down at DP_{PPFPA} 85. Therefore, this condition was still not well-controlled.

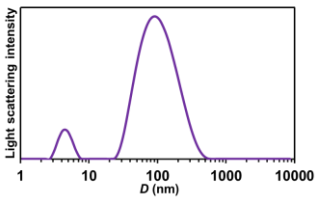	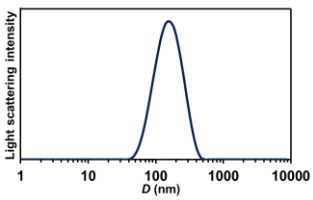	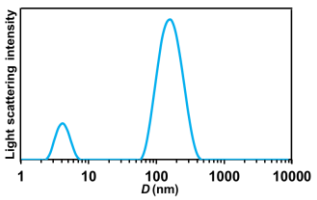
Size = 119.2 ± 1.3	Size = 167.3 ± 7.2	Size = 232.8 ± 73.9
m = 13,	m = 49,	m = 85,
PDI = 0.496 ± 0.007, LSI = 471.4 kcps	PDI = 0.683 ± 0.077, LSI = 541.5 kcps	PDI = 0.683 ± 0.077, LSI = 340.5 kcps
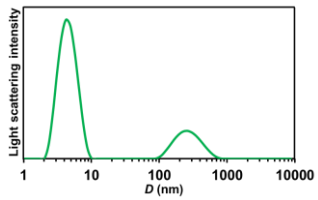	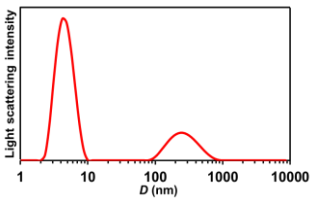	
Size = 299.9 ± 21.2	Size = 205.8 ± 56.3	
m = 92,	m = 94	
PDI = 0.328 ± 0.004, LSI = 89.9 kcps	PDI = 0.347 ± 0.137, LSI = 97.7 kcps	

Figure 3.11 DLS profiles of PM_{25}-PF_m-*20*% in EtOH using polymer concentration (C_p) 1 mg/mL

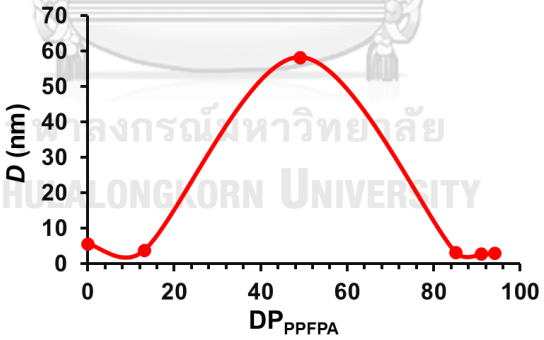

Figure 3.12 The relationship between mean particle diameter and DP_{PPFPA} of PM_{25}-PF_m-*20*% determined by DLS as a number distribution function at C_p = 1 mg/mL

To maintain the stability of diblock copolymeric nanoparticles, PMPC macro-CTA as a stabilizer block should be increased from 50 to 100. Moreover, the condition of polymerization should also be changed by performing the reaction at a lower temperature to retard the polymerization rate as investigated. The reactions were performed at a lower temperature of 40°C in ethanol using PMPC macro-CTA DP_{100}. Polymer solutions at different time points became opaquer as the DP_{PPFPA} increased as shown in **Figure 3.13**.

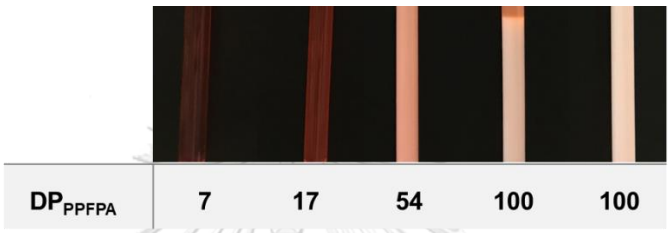

Figure 3.13 Polymer solutions of PM_{100}-PF_m-*20*% prepared in EtOH

Under this condition, the polymer solution did not precipitate as a relatively long $PMPC_{100}$ macro-CTA was used as the stabilizer block. Monomer conversion evaluated by ^{1}H NMR spectroscopy gradually increased with polymerization time and reached 100% at 12 h (**Figure 3.14A**). Besides, the pseudo-first-order kinetic plot showed linearity from 0 h until 5 h (**Figure 3.14B**) suggesting well-controlled polymerization. The kinetic results agreed with the physical appearance of the polymer solutions that did not precipitate during PISA.

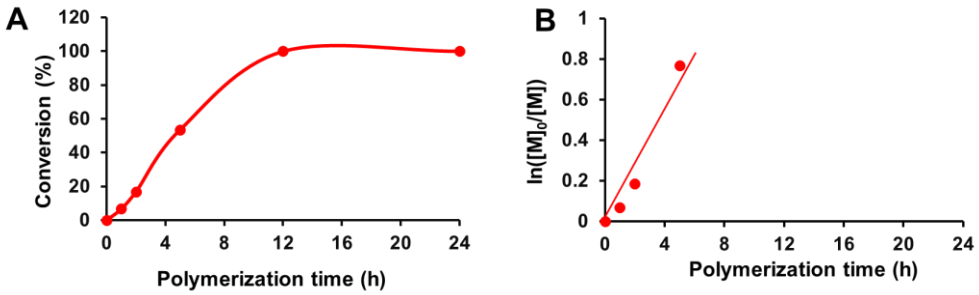

Figure 3.14 (A) A plot of monomer conversion vs polymerization time and (B) pseudo-first-order polymerization kinetics of PM_{100}-PF_m-*20*% in ethanol.

DLS profiles of PM_{100}-PF_m-*20*% this condition investigated as a function of LSI (**Figure 3.15**) distributions showed bimodal distributions under some conditions: PM_{100}-PF_7 and PM_{100}-PF_{17} indicating that polymerization of PPFPA was not well-controlled. The evolution of particle size against DP_{PPFPA} agreed with the previous assumption that the trend was also found to be unusual due to uncontrolled polymerization as shown in **Figure 3.16**.

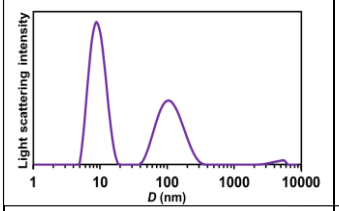	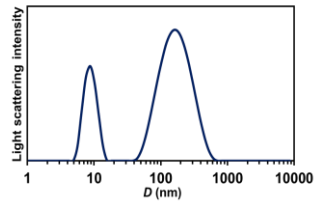	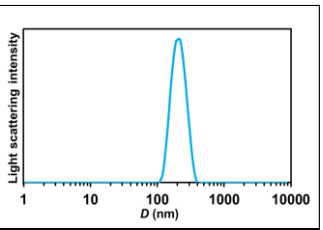
Size = 139.2 ± 18.1	Size = 213.1 ± 25.8	Size = 224.8 ± 7.54
m = 7,	m = 17,	m = 54,
PDI = 0.558 ± 0.018, LSI = 464 kcps	PDI = 1.000 ± 0.000, LSI = 1,296 kcps	PDI = 0.062 ± 0.040, LSI = 82,817 kcps
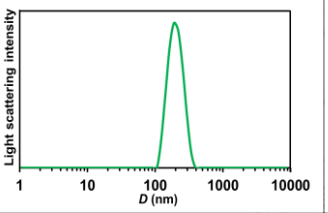	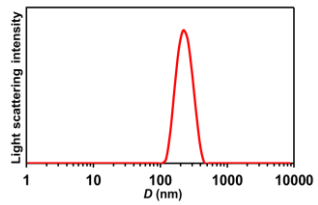	
Size = 209.8 ± 4.1	Size = 242.4 ± 7.0	
m = 100,	m = 100	
PDI = 0.047 ± 0.011, LSI = 92,604 kcps	PDI = 0.075 ± 0.023, LSI = 49,120 kcps	

Figure 3.15 DLS profiles of PM_{100}-PF_m-*20*% in EtOH at C_p = 1 mg/mL

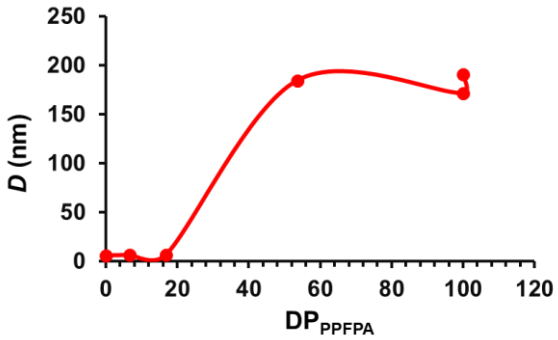

Figure 3.16 The relationship between mean particle diameter and DP_{PPFPA} of PM_{100}-PF_m-*20*% determined by DLS as a number distribution function at C_p = 1 mg/mL

Up to this point, it was realized that the uncontrolled polymerization may be caused by the unequivalent reactivity [95] between the methacrylate monomer, MPC and the acrylate monomer, PFPA. In principle, MPC is more reactive than PFPA as the former generates the tertiary radical species which are more stable than the secondary radical generated by the latter during radical polymerization. To solve this problem, PFPMA was selected as an alternative monomer of which reactivity towards radical polymerization is equivalent to MPC.

3.3 Dispersion polymerization of PFPMA using PMPC macro-CTA

Here, in this case, a series of the block copolymer, $PMPC_n$-*b*-$PPFPMA_m$ with different solid concentration (*x*%), (PM_n-PFM_m-*x*%) were synthesized. Having used PMPC macro-CTA with *n* of 50 and 100, *m* which is the DP of core-forming block of PPFPMA as well as the solid concentration were varied. The maximum *m* was set to be 200. ^{1}H and ^{13}C NMR were used to confirm the success of block copolymer synthesis. As shown for PM_{50}-PFM_{60}-*20*% (**Figure 3.17A**), the characteristic signals appeared at 0.8 – 1.1 and 1.1-2.6 ppm attributable to methyl and methylene protons of the polymer backbone, respectively. The proton signal of peak *m* at 3.1 ppm is assignable to the methyl groups of quaternary amine ($(C\underline{H}_3)_3$-N^+). On the other hand, the signals around 3.6 – 4.3 ppm correspond to α-methyl of a phosphoryl group (peak *a, k*), ester bond (peak *b*) and quaternary amine (peak *l*) of PMPC side group.

According to ^{13}C NMR spectrum (**Figure 3.17B**), carbonyl groups of PMPC and PPFPMA appeared at 178 and 173 ppm, respectively. Carbon atoms of the pentafluorophenyl moiety appeared in a range of 125 – 143 ppm. Moreover, ^{19}F NMR and FT-IR spectroscopy (**Figure 3.18**) were used to confirm the presence of PPFPMA in the diblock copolymer.

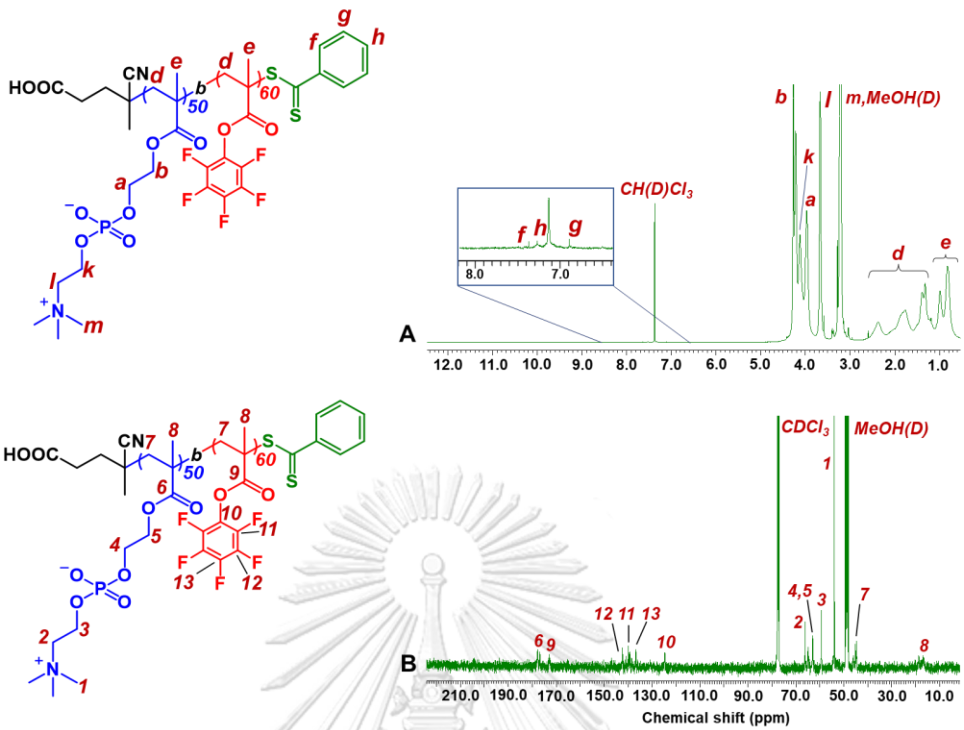

Figure 3.17 (A) ^{1}H NMR spectrum of PM_{50}-PFM_{60}, and (B) ^{13}C NMR spectrum of PM_{50}-PFM_{60}, recorded in $CDCl_3$/MeOH-d_4 (3/1, v/v) at 60°C.

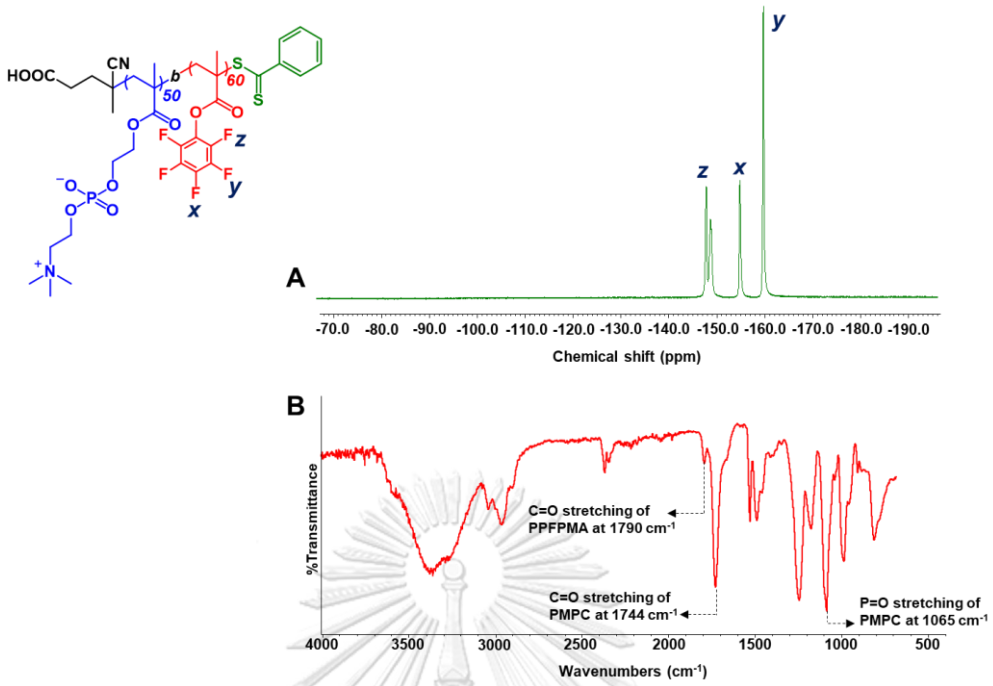

Figure 3.18 (A) ^{19}F NMR spectrum, recorded in $CDCl_3$/MeOH-d_4 (3/1, v/v) at 60 °C and (B) ATR-IR spectrum of PM_{50}-PFM_{60}

There are the characteristic peaks of pentafluorophenyl group in the polymer chain appearing at -147, -149 ppm (*ortho*), -155 ppm (*para*), and -161 ppm (*meta*). FT-IR spectrum showed C=O stretching of carbonyl groups of PPFPMA and PMPC at 1790 and 1744 cm^{-1}, respectively. The appearance of phosphoryl group corresponding to PMPC side chain can also be evidenced from P=O stretching at 1065 cm^{-1}.

As determined from ^1H NMR data, the kinetics of RAFT dispersion polymerization of PFPMA using PMPC macro-CTA to synthesize block copolymers with targeted DP_{PPFPMA} of 200 can be established**.** According to **Figure 3.19**, using $PMPC_{50}$ as macro-CTA, PFPMA was almost entirely consumed by 8 h at 20% solid concentration. The kinetic of polymerization became much slower at 5% solid concentration indicating the dilution has a strong impact on the growth of PPFPMA second block. It took 24 h for complete PFPMA conversion. Increasing the chain length and molecular weight of the PMPC macro-CTA from 50 to 100, the kinetic was

so low that only 54% PFPMA conversion was reached at 24 h. Pseudo-first order kinetics (**Figure 3.19B**) demonstrated that the RAFT dispersion polymerization of PFPMA was well controlled regardless of the molecular weight of PMPC macro-CTA and solid concentration.

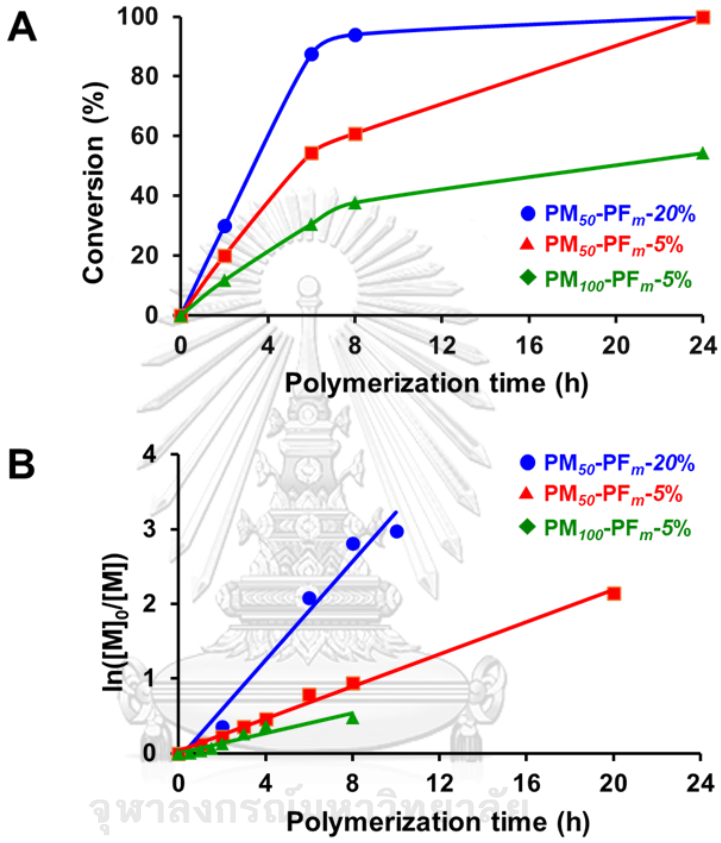

Figure 3.19 (A) Monomer conversion as a function of polymerization time and (B) pseudo-first order kinetics of PFPMA polymerization using PMPC as a macro-CTA.

Additionally, DLS profiles as a function of LSI of PM_m-*b*-PFM_n (**Figure A6**) displayed narrow distribution in all conditions, implying that polymerization of the diblock copolymer using PMPC macro-CTA and PFPMA as a monomer for a second block was well-controlled and also generate well-defined polymeric micelles.

3.3.1 Characterization of nanostructures formed upon PISA

Nanostructures self-assembled from the block copolymers were monitored by both TEM and DLS. As shown in **entry 2, column 1 of Figure 3.20**, PM_{50}-PFM_{60}-*20%* assembled into spherical-like micelles with bumpy surface having size of ~ 131.5 nm. Individual particle looks like an aggregate of smaller nanoparticles (~ 20 – 30 nm). Further growth of PPFPMA block let to PM_{50}-PFM_{93}-*20%* with slightly larger overall diameter (~ 147.9 nm) having the same morphology. There seems to be a greater number of small nanoparticles combined into one aggregate. The fact that DLS profiles (**column 1**, **Figure 3.21**) of both block copolymers appear as single peaks with extremely low polydispersity index (PDI of less than 0.1) suggested that the assembled nanostructures are extremely mono-dispersed. Relatively high light scattering intensity (LSI) of ~ 100,000 also verified the high solid concentration of the solution which appear milky (top right insets in **column 1 of Figure 3.20**). As anticipated, the sizes determined by DLS under hydrated condition are slightly larger than those evaluated by TEM under de-hydrated condition. It should be emphasized that the solution became precipitated once the conversion of PFPMA was almost complete (DP_{PPFPMA} in the range of 188 – 200), implying that the PMPC block with DP of 50 was not enough to provide colloidal stability to the self-assembled structures.

As a result of slower kinetic at 5% solid concentration, we managed to prepare the block copolymer with the shorter PPFPMA block, PM_{50}-PFM_{22}-*5%*. As shown in **entry 1, column 2 of Figure 3.20**, the assembled structure also appeared as bumpy micelles, each contains a few extremely small particles, with an approximate overall diameter ~ 47.2 nm. Extending the block of PPFPMA gave rise to PM_{50}-PFM_{60}-*5%* having a similar structure with slightly larger overall diameter. Interestingly, small nanoparticles of PM_{50}-PFM_{60}-*5%* that combined into one aggregate were larger than those of PM_{50}-PFM_{22}-*5%* as anticipated for the longer PPFPMA block (**entry 2, column 2 of Figure 3.20**).

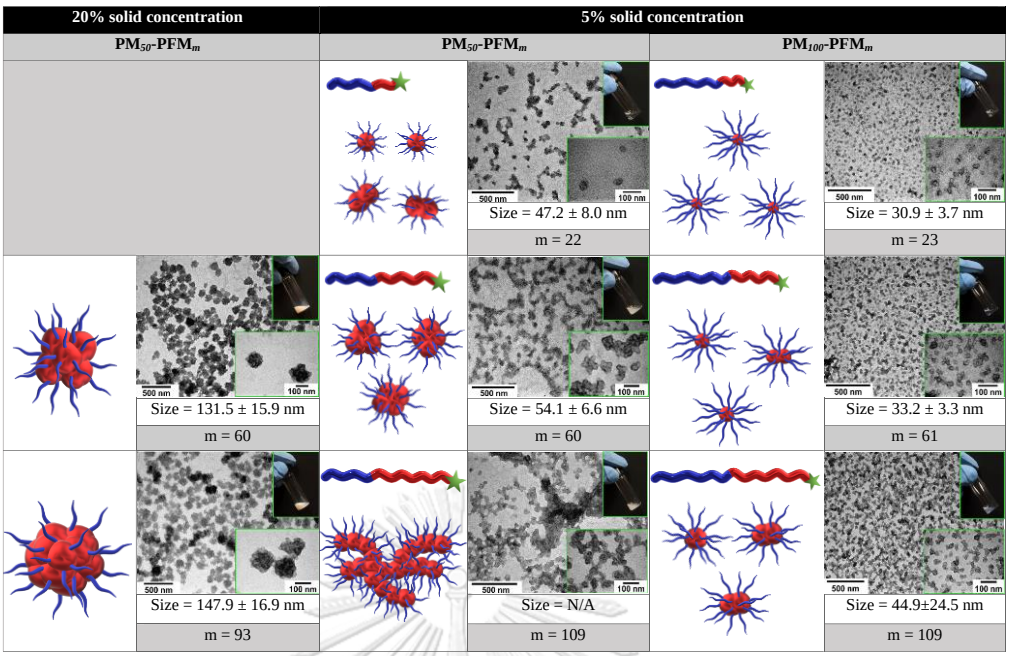

Figure 3.20 TEM images (10,000x) and proposed morphologies of the PM_{50}-PFM_m and PM_{100}-PFM_m series having 5 and 20% solid concentration. Each TEM image contains two insets; one on the top right shows an image of the copolymer solution and one at the bottom right shows a magnified TEM image (40,000x).

20% solid	5% solid	
PM_{50}-PFM_m	PM_{50}-PFM_m	PM_{100}-PFM_m
	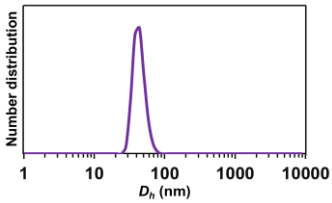	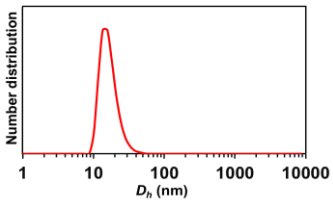
	Size = 39.6 ± 4.1 nm	Size = 24.1 ± 2.6 nm
	m = 22	m = 23
	PDI = 0.144 ± 0.080, LSI = 1,206	PDI = 0.235 ± 0.024, LSI = 258
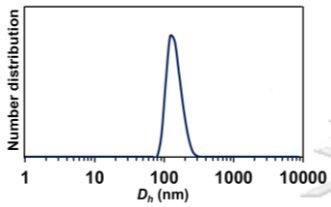	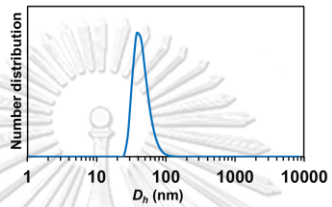	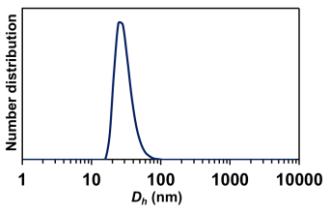
Size = 142.5 ± 1.6 nm	Size = 47.6 ± 1.9 nm	Size = 30.3 ± 4.1 nm
m = 60	m = 60	m = 61
PDI = 0.009 ± 0.007, LSI = 130,143	PDI = 0.095 ± 0.010, LSI = 3,173	PDI = 0.159 ± 0.057, LSI = 917
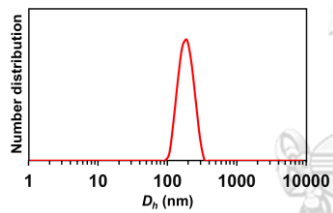	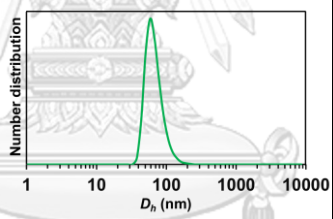	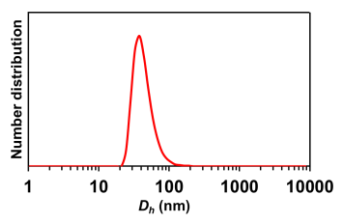
Size = 168.3 ± 2.1 nm	Size = 69.9 ± 2.8 nm	Size = 54.9 ± 12.0 nm
m = 93	m = 109	m = 109
PDI = 0.036 ± 0.005, LSI = 98,549	PDI = 0.117 ± 0.021, LSI = 7,637	PDI = 0.161 ± 0.157, LSI = 3,330

Figure 3.21 DLS profiles of PM_{50}-PFM_m and PM_{100}-PFM_m series with a variety of solid concentration

Having the same block composition, the PM_{50}-PFM_{60}-*5%* apparently consisted of fewer smaller particles in one aggregate than the PM_{50}-PFM_{60}-*20%* (**entry 2, column 1 of Figure 3.20**) suggesting the solid content has a strong impact on both packing density and size of the aggregates. Increasing the PPFPMA block length further to 109 yielded PM_{50}-PFM_{109}-*5%* of which assembled structure was no longer regular in both size and shape. The undirectional inter-micellar aggregation gave

interconnected network (**entry 3, column 2 of Figure 3.20**) so that the size of individual aggregate cannot be identified. As expected, LSI values of the series of PM_{50}-PFM_m-*5%* proportionally decreased as a result of lower solid content as opposed to those of the series of PM_{50}-PFM_m-*20%* (**column 2**, **Figure 3.21**). The solutions appeared to be less milky and more translucent (top right insets in **column 2 of Figure 3.20**).

It has been reported that high-order morphological transition (e.g. sphere-worm-vesicle) during PISA depends on many factors such as volume fraction between hydrophilic/hydrophobic blocks [96, 97], directional fusion between particles to minimize the surface energy [98]. Directional fusion may be disturbed by enormous inflexibility of the polymer chains. Therefore, undirectional sphere-sphere fusion may occur, leading to bumpy micelles and self-aggregation instead of structures with high-order morphologies.[99] Such a trend was observed in this research. Spherical-like micelles of varied degree of inter-particle fusion were evidenced for both the series of PM_{50}-PFM_m-*20%* and PM_{50}-PFM_m-*5%* of which *m* value is less than or close to 50. In other words, the length of core-forming hydrophobic block of PPFPMA does not exceed that of the shell-forming hydrophilic block of PMPC. It is believed that the limited chain mobility is caused by π-π stacking together with hydrophobic interactions among pentafluorophenyl (PFP) entities, the side groups of the core-forming PPFPMA block. In the case of PM_{50}-PFM_{109}-*5%* of which the PPFPMA block was twice longer than the PMPC block, the polymer chains would become even more inflexible. The hydrophilic PMPC composition was not certainly enough to yield spherical-like structure, the most stable morphology, but rather gave rod-like and network-like structures (**entry 3, column 2 of Figure 3.20)**. The formation of assembled structures with unusual non-spherical morphology ("lumpy rod") was also reported by Sugihara and co-workers [100]. *In situ* crosslinking by bifunctional monomer of ethylene glycol dimethacrylate used as a second block

for aqueous dispersion polymerization through PISA led to extreme inflexibility of the polymer chains.

For the series of PM_{100}-PFM_m-*5%*, all assembled structures appeared as spherical-like micelles with lesser degree of inter-particle aggregation as opposed to the series of PM_{50}-PFM_m-*20%* and PM_{50}-PFM_m-*5%*. An average diameter of the individual micelle was in a range of 30-50 nm and proportionally increased as a function of PPFPMA block length. It is obvious that the PMPC with DP of 100 was long enough to provide good colloidal stability to the individual micelle so that the inter-particle aggregation was suppressed. Notably, LSI values of the PM_{100}-PFM_m-*5%* series (**column 3**, **Figure 3.21**) were much less than those of the PM_{50}-PFM_m-*5%* series. This may be explained as a consequence of slow kinetic and relatively low monomer conversion (See **Figure 3.19**). As shown in top right insets in **column 3 of Figure 3.20**, the solutions of the PM_{100}-PFM_m-*5%* series is correspondingly more translucent than other series.

3.4 Core functionalization of nanostructures

The ability to undergo functionalization via post-polymerization modification of the PPFPMA situated in the core of nanostructures assembled upon PISA was evaluated by reacting with PMA, a fluorescence dye. With its well-dispersed characteristic, relatively uniform spherical morphology with low degree of inter-particle aggregation and reasonable composition of functionalizable PPFPMA, PM_{100}-PFM_{61}-*5%* was chosen as a representative diblock copolymer to be subjected to the test. Several attempts have been made to post functionalize the core of PM_{100}-PFM_{61}-*5%* nanostructure. It turned out that the modification was only successful upon using an elevated temperature (75°C) for quite a long period of time (48 h) in the presence of basic catalyst, TEA. We described this difficulty towards modification as a result of the strong π-π stacking and hydrophobic interactions among PFP groups of the core-forming PPFPMA block as mentioned earlier together with the effective stabilization of relatively long hydrophilic PMPC shell that limited the accessability of the nucleophilic modifier, PMA into the core of the nanostructure.

The appearance of a new aromatic proton signal at 8.3 ppm and a shift of methylene protons at 4.6 ppm of conjugated PMA (shifted from 4.9 ppm of free PMA, **Figure 3.22B**) in the ^{1}H NMR spectrum of PM_{100}-PFM_{61}-*5%* nanostructure after reacting with PMA (**Figure 3.22C**) clearly confirmed the success of post-functionalization. Also, the disappearance of five fluorine signals of PFPMA repeat units at -148, -157, and -163 ppm implied that all PFP groups were entirely removed after the modification (**Figure 3.23A**). Additionally confirmed by FT-IR analysis, the disappearance of C=O stretching at 1790 cm^{-1} of ester groups in the PPFPMA block and the increment of C=O stretching at 1674 cm^{-1} and N-H bending at 1598 cm^{-1} reflected the success of PMA attachment via amide bond formation (**Figure 3.23B**).

Nevertheless, a peak split at 1730 cm^{-1} which can be assigned to C=O stretching of carboxyl group clearly implied that PFP ester groups of the core-forming PPFPMA block did not only react with PMA, but also partially hydrolyzed. This may be unavoidable given that the post-polymerization modification was performed at elevated temperature in the presence of basic catalyst. It is also possible that this partial hydrolysis generating hydrophilic carboxyl groups may help loosen the packing of the remaining unreacted PFP entities so that they became easily accessible to the nucleophilic modifier, PMA and thus promoted the post functionalization

The presence of pyrene entities in the core of PM_{100}-PFM_{61}-*5%* nanostructure after post functionalization with PMA was also verified by UV/Vis spectroscopy. According to **Figure 3.24A**, free PMA in MeOH showed the absorption spectrum at the maximum wavelength (λ_{max}) of 340 nm whereas the absorbance of the PM_{100}-PFM_{61}-*5%* modified with PMA showed the red-shifted λ_{max} at 345 nm implying that there is aromatic π-π stacking of pyrene in the core of micelles [101, 102]. As calculated from the calibration curve shown in **Figure A7, Appendix**, the loading content of pyrene in the nanostructure was 230 mg/g (pyrene/copolymer). This value indicated that 36 out of 61 PFPMA repeat units (59%) in the core of nanostructure being substituted with PMA and implying that the rest of PFPMA repeat units (41%) were hydrolyzed. This agrees quite well with the result obtained from FT-IR analysis in that partial hydrolysis took place. The composition of PMPC: PFPMA modified with PMA as shown in **Table 3.2** of 100:36 was close to 100:33 that was evaluated by ^{1}H NMR analysis.

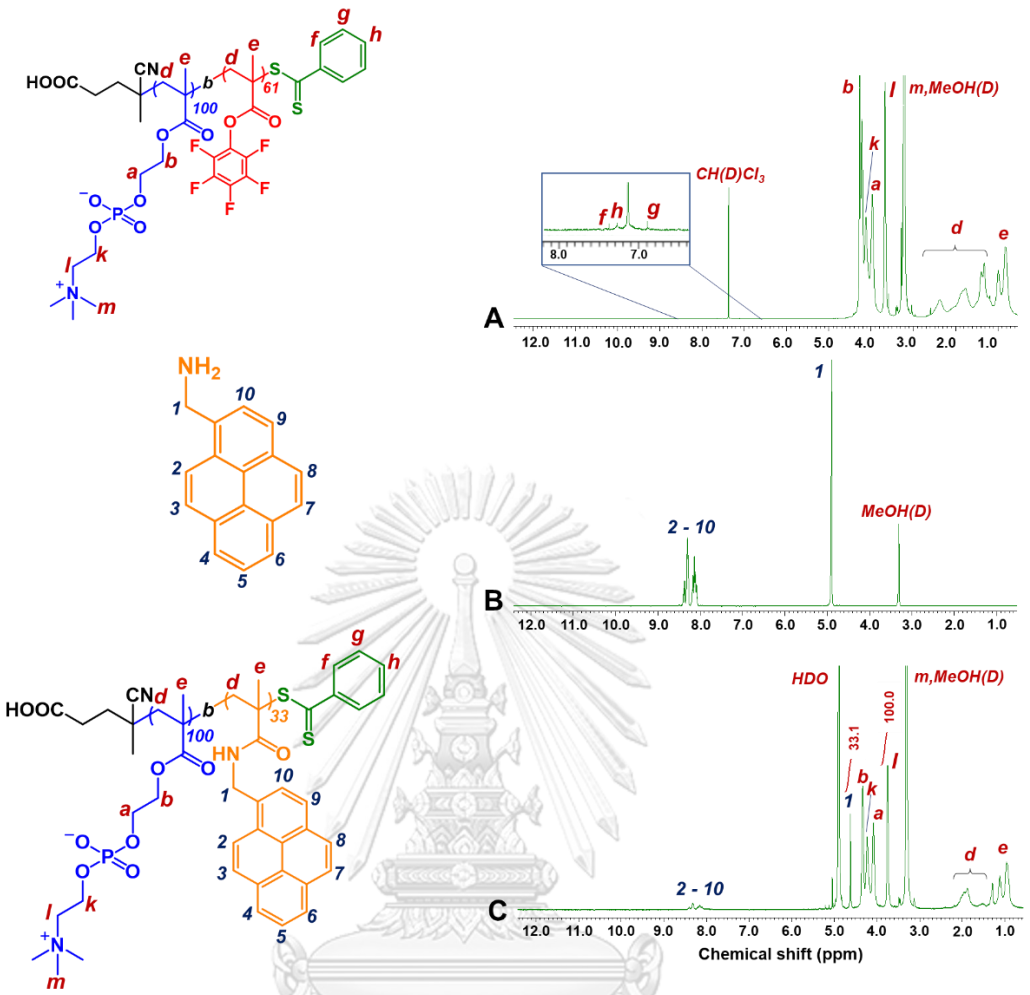

Figure 3.22 ^{1}H NMR spectra of (A) PM_{100}-PFM_{61}-*5*%, recorded in $CDCl_3$/MeOH-d_4 (3/1, v/v) at 60 °C, (B) PMA and (C) PM_{100}-PFM_{61}-*5*% after reacting with PMA, recorded in MeOH-d_4 at 25 °C.

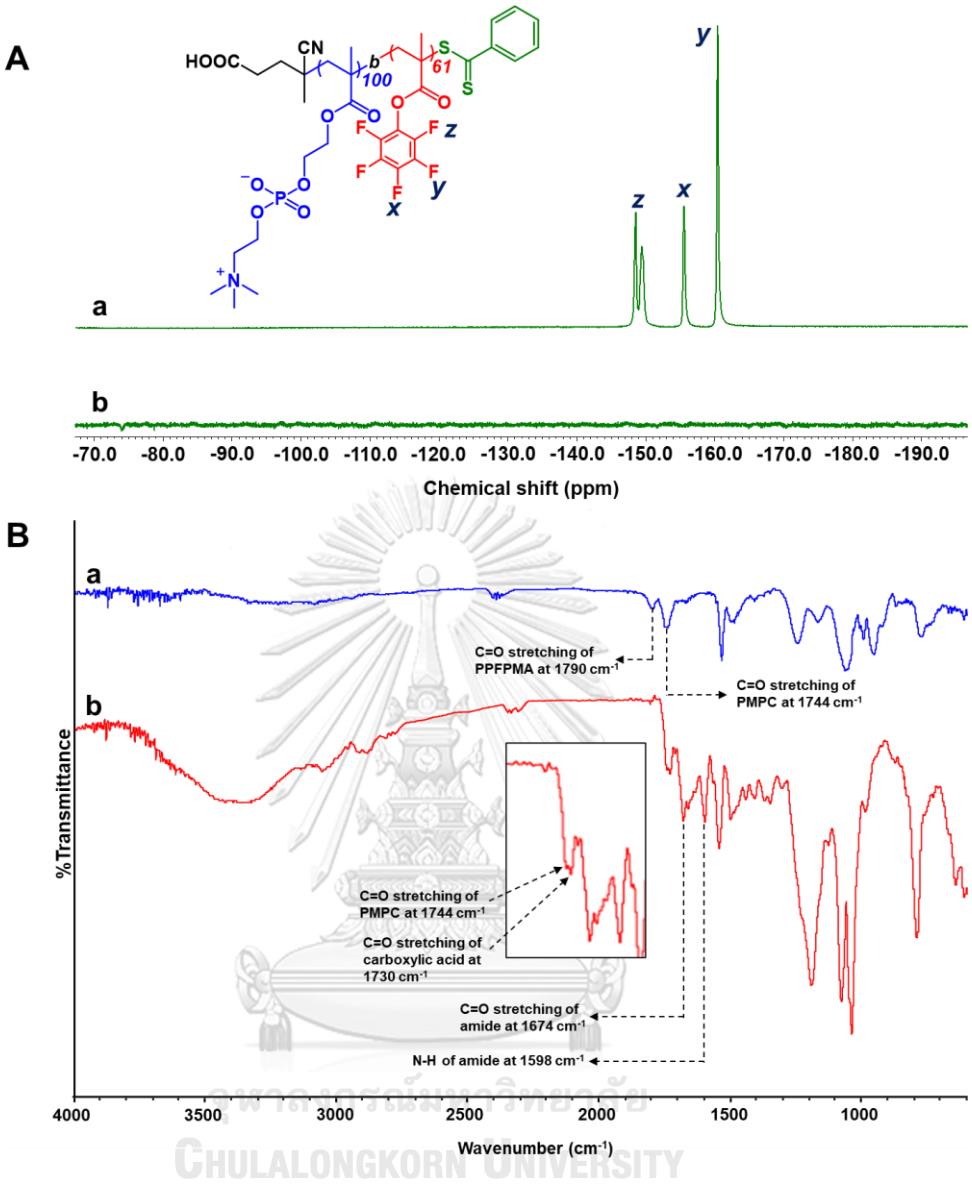

Figure 3.23 (A) ^{19}F NMR spectra recorded in $CDCl_3$/MeOH-d_4 (3/1, v/v) at 60 °C and (B) FT-IR spectra of PM_{100}-PFM_{61}-*5*% (a) before and (b) after reacting with PMA.

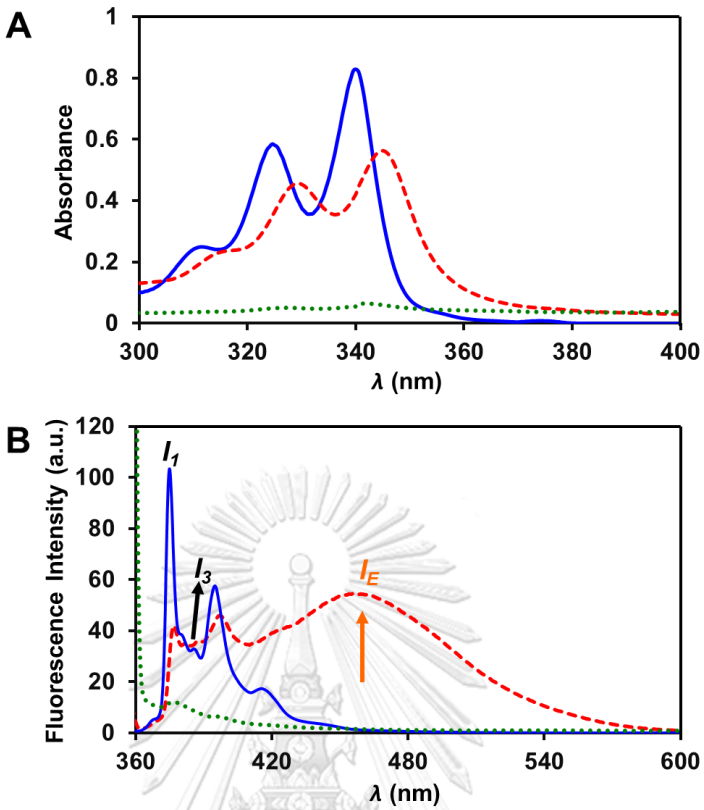

Figure 3.24 (A) UV-visible absorption spectra in MeOH at 25 °C and (B) fluorescence emission spectra (λ_{ex} = 340 nm) in H_2O at 25 °C with slid width of 1.0 nm of PMA (—), PM_{100}-PFM_{61}-5% before (···) and after (---) reacting with PMA.

Table 3.2 The exchange ratio of PMPC:PPFMA calculated from ^{1}H NMR and UV-visible spectroscopy

	The exchange ratio of PMPC:PPFMA	
PMPC:PPFMA = (100:61)[a]	^{1}H NMR	UV-visible[b]
	100:33	100:36

[a]Calculated from quantitative ^{13}C NMR

[b]Calculated by using the standard curve of PMA following the equation:

PMA composition = $\frac{mol\ of\ PMA\ in\ copolymer}{mol\ of\ PFMA\ pendants\ in\ copolymer} \times composition\ unit\ of\ PFMA\ in\ copolymer$

The successful modification by PMA attachment can also be demonstrated by fluorescence spectroscopy as shown in **Figure 3.24B**. Normally, pyrene and its derivatives have been extensively studied as a fluorescence probe to determine microenvironmental polarity from the ratio of the intensities of the first at 376 nm and the third peaks at 388 nm (I_3/I_1) of their emission spectra [103]. Herein, free PMA showed fluorescence emission spectrum with a ratio of I_3/I_1 of 0.32 upon excitation (λ_{ex}) at 340 nm. After being incorporated into the micellar core, I_3/I_1 increased to 0.86. This greater value than that of the free PMA suggested that the pyrene entities situated inside the core experienced a more hydrophobic environment as they substituted PFP ester moieties via post-polymerization modification [104]. Additionally, the increment of fluorescence excimer emission (I_E) at 460 nm and corresponding I_E/I_M ratio (from 0.01 of free PMA to 1.30 of PM_{100}-PFM_{61}-*5%* modified with PMA*)* of which I_M is the intensity of monomer peak at 376 nm implied the closer of neighboring pyrene inside the core of nanostructure due to π- π stacking interaction [105].

After post-polymerization modification with PMA, the nanostructure of PM_{100}-PFM_{61}-*5%* still maintained its micellar structure and spherical shape. As demonstrated by TEM analysis **(Figure 3.25A)** the size of the assembled PM_{100}-PFM_{61}-*5%* prepared in H_2O increased in diameter from ~ 68 to ~ 87 nm after modification. As evaluated by DLS **(Figure 3.25B)** the mean hydrodynamic diameter (D_h) of the assembled particles slightly increased with reasonably narrow PDI (PDI = 0.169) suggesting that the PM_{100}-PFM_{61}-*5%* remained stably dispersed after modification. These results also imply that nanostructure of PMPC-*b*-PPFPMA is core-functionalizable by reactive modifier and can be conveniently prepared for appropriate applications.

For polymer aggregation behavior after post-functionalization, mean hydrodynamic diamether (D_h) of particles before and after post-modification were determined by DLS in H_2O (**Figure 3.25**). $PMPC_{100}$-$PPMA_{33}$ still maintained its micellar structure after post-modification as shown in DLS profile with narrow distribution (PDI = 0.169). D_h of the post-modified micelle was 124.7 nm which was slightly greater than that the micelle before post-functionalization due to larger PMA incorporated inside the core. TEM images of the polymeric micelles in solid state before and after post-functionalization prepared in H_2O show spherical shape of the modified polymer with the mean diameter of particles ~ 68 nm. After post-polymerization modification, the modified polymer also maintained its structure as the spherical micelles became larger than that before post-functionalization with the mean diameter ~ 87 nm due to larger PMA molecules than PFMA side groups were incorporated. These results imply that core-functionalizable PMPC-*b*-PPFPMA micelles could be post-functionalized by reactive modifiers, allowing polymeric micelles to be conveniently prepared for appropriate applications.

A	PM_{100}-PFM_{61}	PM_{100}-PFM_{61} after modification with PMA
	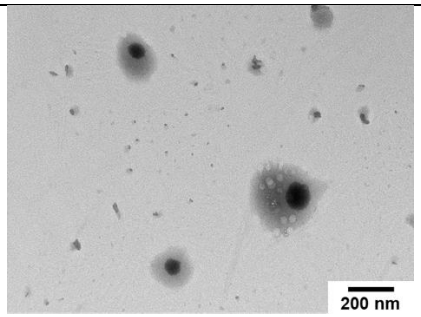	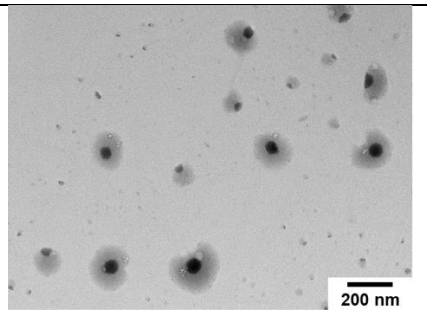
B	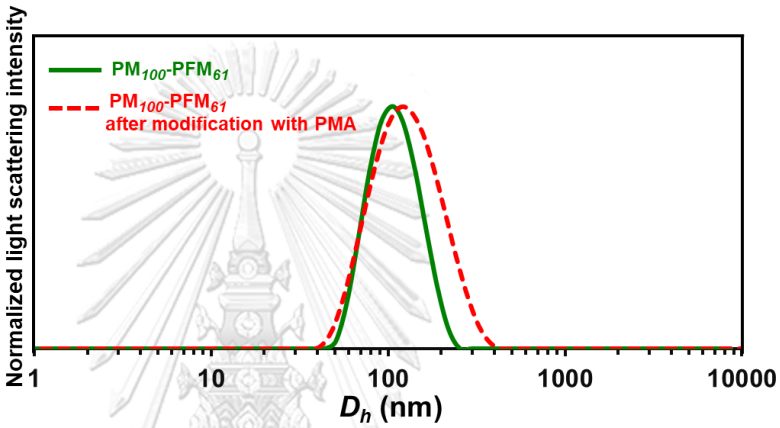	
$D_{h,TEM}$ (nm)	67.9±6.1	87.3±22.8
$D_{h,DLS}$ (nm)	112.5±0.7 PDI = 0.077±0.018	124.7±7.9 PDI = 0.169±0.014

Figure 3.25 (A) Representative TEM micrographs and (B) DLS profiles of PM_{100}-PFM_{61} before and after modification with PMA, prepared in H_2O with polymer concentration (C_p) = 1.0 g/L, I indicates the light scattering intensity (LSI).

3.5 Post-polymerization modification of PPFPA for being used as an antioxidant nanoparticle

3.5.1 Synthesis of PPFPA as a polymer precursor

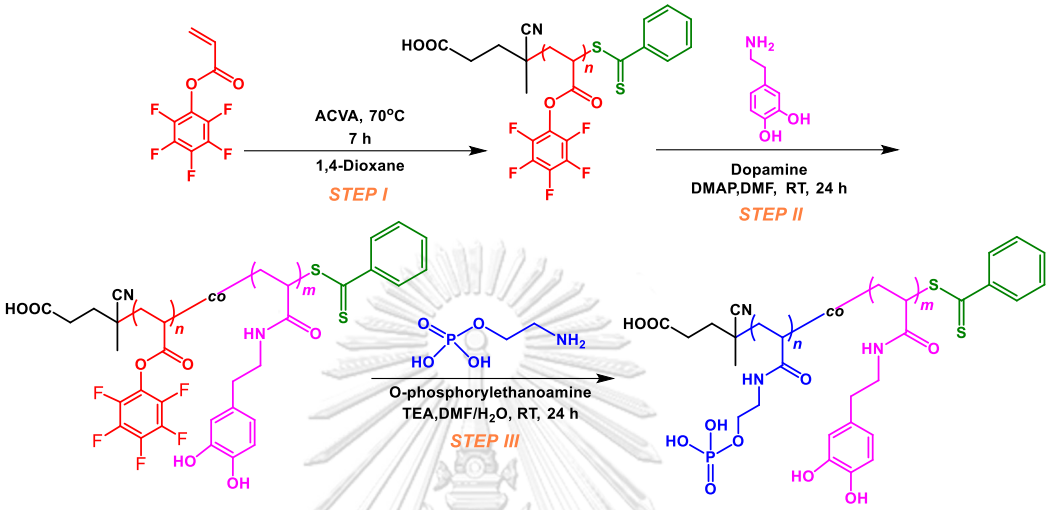

Figure 3.26 Synthetic route of PPFPA by RAFT polymerization and post-polymerization modification to be used as an antioxidant nanoparticle

PPFPA with a target DP of 100 was synthesized via RAFT polymerization at 70°C in 1,4-dioxane as a solvent for 7 h as shown in **Figure 3.30, step I**. PPFPA was characterized and evaluated DP by ^{1}H NMR as shown in **Figure 3.31**. The characteristic proton signals appeared at 1.2 – 2.6 ppm and 2.6 – 3.6 ppm attributed to CH_2 and CH of polymer backbone (peak *a, b*), respectively. An appearance of signals from aromatic protons (peak *f, g, h*) suggested the presence dithiobenzoate group at the chain end of PPFPA.

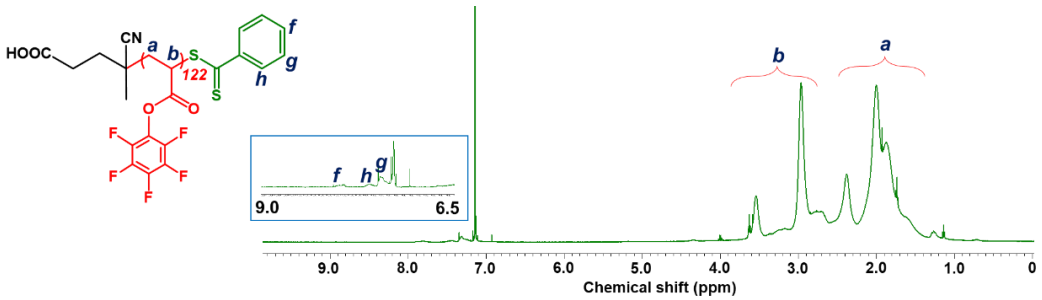

Figure 3.27 ^{1}H NMR spectrum of PPFPA, recorded in $CDCl_3$ at 25°C

The molecular weights determined by ^{1}H NMR ($M_{n,\ NMR}$) are close to the theoretical values ($M_{n,\ th}$) as shown in **Table 3.3**. Theoretical molecular weight ($M_{n.Th}$) of PPFPA was calculated using **Equation 3.3.**

$$M_{n,Th} = \frac{[monomer] \times M_{w,monomer}}{[CTA]} \times conversion + M_{w,CTA} \qquad \textbf{(3.3)}$$

The molecular weight of PPFPA was calculated from the ^{1}H-NMR data ($M_{n.NMR}$) using **Equation 3.4**.

$$M_{n,\ NMR} = \frac{\int H_a \,/\, 2}{\int H_{f,g,h} \,/ 5} + M_{w,CTA} \qquad \textbf{(3.4)}$$

where H_a are the protons at position a corresponding to PPFPA backbone and $H_{f,g,h}$ are the protons of dithioester end-group at the position *f, g, h* as appearing in the ^{1}H-NMR spectrum (**Figure 3.27**).

Table 3.3 Molecular weights and molecular weight distribution of the synthesized PPFPA

Target DP	Exact DP	*%Conversion*	$M_{n,\ Th}$ × 10^4 (g/mol)	$M_{n,\ NMR}$ × 10^4 (g/mol)
100	122	100	2.41	2.90

$M_{n.Th}$ = Theoretical number-averaged molecular weight

$M_{n,\ NMR}$ = Number-averaged molecular weight determined from ^{1}H-NMR data

Moreover, ^{19}F NMR and FT-IR (**Figure 3.28**) were used to confirm the presence of PPFPMA in the diblock copolymer. There are the characteristic peaks of pentafluorophenyl group in the polymer chain appearing at -153 ppm (ortho), -162 ppm (para), and -156 ppm (meta). FT-IR spectrum showed C=O stretching of carbonyl groups of PPFPA at 1780 cm^{-1}.

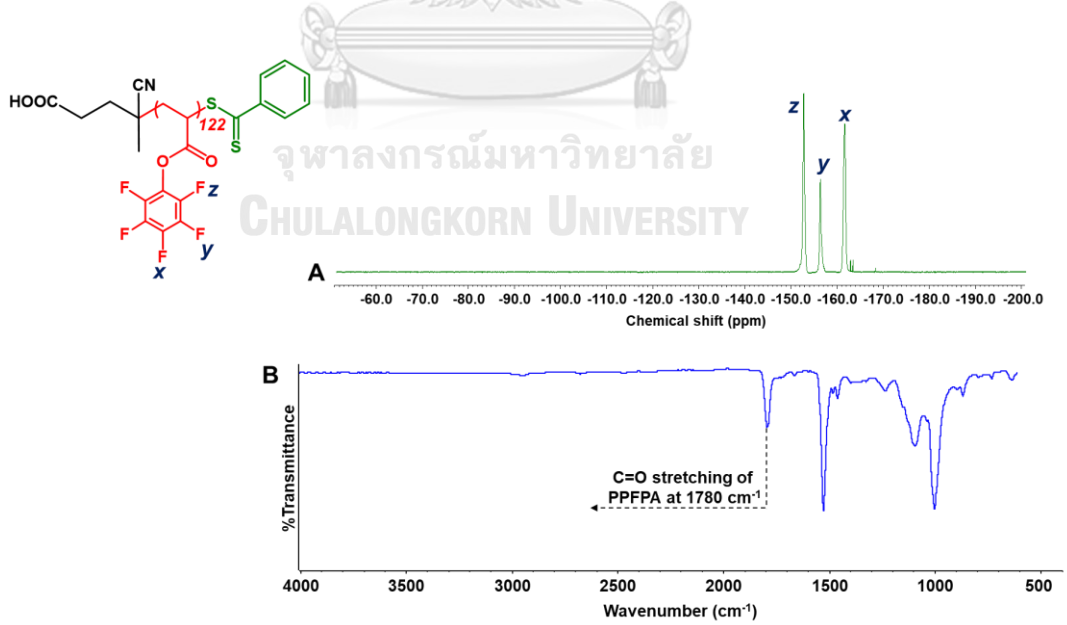

Figure 3.28 (A) ^{19}F NMR spectrum recorded in $CDCl_3$ at 25 °C and (B) ATR-IR spectrum of PPFPA.

PPFPA$_{122}$ was sequentially post-modified by different ratios of DA using DMAP as a base catalyst in DMF as solvent. The reaction was performed at room temperature for 24 h yielding PDA-*co*-PPFPA. After purification, the remaining PFP-entities in PDA-*co*-PPFPA were also post-functionalized by excess PEA to yield the variety composition of PDA$_x$-*co*-PPEA$_y$. Post-polymerization modification of PPFPA by DA and PEA was confirmed by ^{19}F NMR as investigated in **Figure 3.29**.

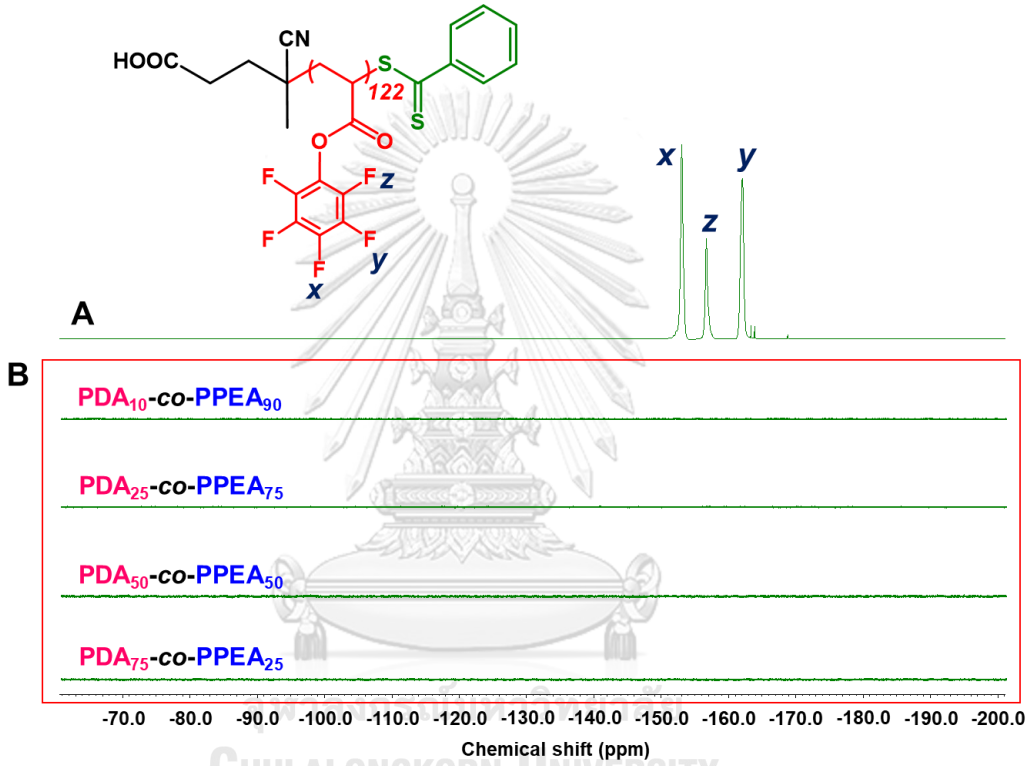

Figure 3.29 ^{19}F NMR spectra recorded in $CDCl_3$ at 25°C of PPFPA of (A) before and (B) after reacting with DA and PEA to yield the various ratios of PDA$_x$-*co*-PPEA$_y$.

The disappearance of five fluorine signals of PPFPA repeat units at -153, -156, and -162 ppm implied that all PFP groups in all compositions were entirely removed after the modification (**Figure 3.29**). Additionally confirmed by ATR-IR analysis, the appearance of O-H stretching of DA in the polymer chain of spectra d – h between 2800 – 3600 cm^{-1} can be confirmed the success of post-polymerization modification by DA. P=O stretching of the phosphate group of PEA at 1124 cm^{-1} confirmed the

attachment of PEA in the polymer chain. The disappearance of C=O stretching at 1780 cm^{-1} of ester groups in the PPFPA and the increment of C=O stretching at 1688 cm^{-1} and N-H bending at 1578 cm^{-1} reflected the success of DA and PEA substitution via amide bond formation (**Figure 3.30**).

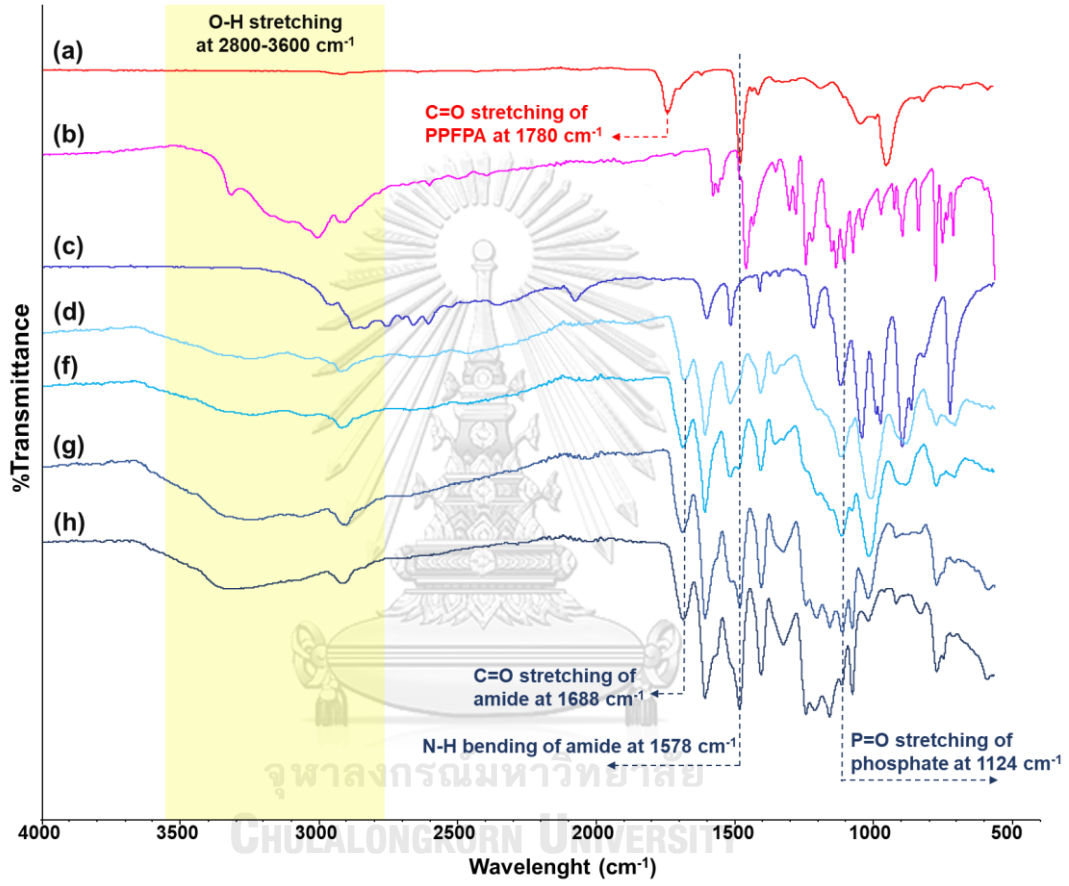

Figure 3.30 ATR-IR spectra of (a) PPFPA, (b) DA, (c) PEA, (d) PDA_{10}-*co*-$PPEA_{90}$, (f) PDA_{25}-*co*-$PPEA_{75}$, (g) PDA_{50}-*co*-$PPEA_{50}$, (h) PDA_{75}-*co*-$PPEA_{25}$

The success of sequential post-polymerization modification by DA and PEA was confirmed by ^{1}H NMR spectroscopy with the appearance of a new aromatic proton signal of DA at 6.3 – 7.2 ppm (peak *f, g, h*) and peak *c, d* at 3.7 and 4.2 ppm, respectively. Moreover, the compositions of DA and PEA in the polymer chain were

evaluated by the relative integration of peaks *f, g, h* which are attributed to protons in the aromatic ring of DA and peak *b* of PPFPA backbone (**Equation 3.5**).

$$x = \frac{\int H_b}{\int H_{f,g,e}/3} \quad , \quad y = 100 - x \tag{3.5}$$

Where *x* and *y* are the compositions of DA and PEA, respectively. It was found that the compositions of DA and PEA calculated from ^{1}H NMR were close to the feed ratios of each modifier as shown in **Table 3.3**.

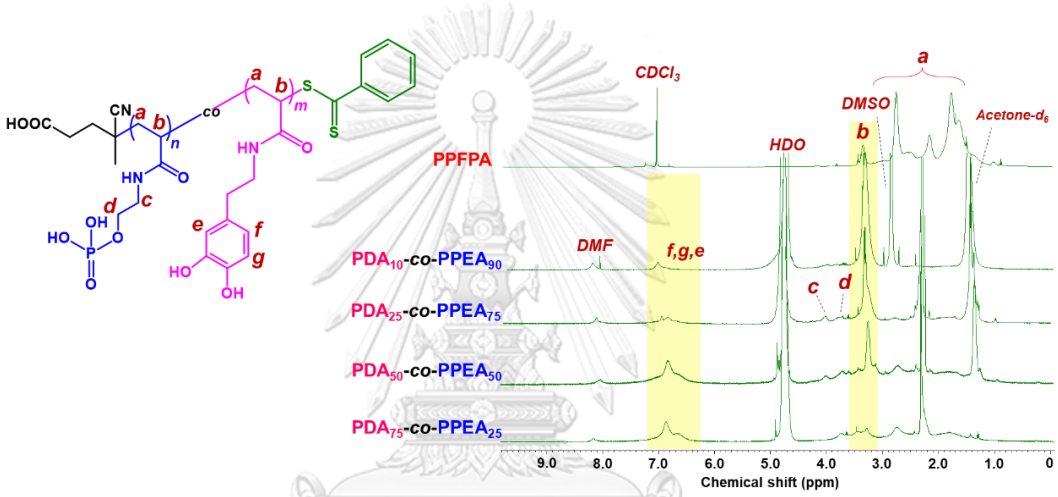

Figure 3.31 ^{1}H spectra of PDA$_x$-*co*-PPEA$_y$, recorded in $CDCl_3$/acetone-d_6 (1/1, v/v) at 25°C

Table 3.4 The compositions of DA and PEA in the polymer chain calculated from ^{1}H NMR

PDA_x-*co*-$PPEA_y$	**Feed ratio of DA:PEA**	**The compositions of DA:PEA calculated from ^{1}H NMR**
PDA_{10}-*co*-$PPEA_{90}$	10 : 90	7 : 93
PDA_{25}-*co*-$PPEA_{75}$	25 : 75	19 : 81
PDA_{50}-*co*-$PPEA_{50}$	50 : 50	56 : 44
PDA_{75}-*co*-$PPEA_{25}$	75 : 25	N/A

N/A = not measurable

Unfortunately, the compositions of DA and PEA could not be estimated for PDA_{75}-*co*-$PPEA_{25}$ since there was no peak *b* of PPFPA backbone in ^{1}H NMR spectrum due to the limitation of copolymer solubility in the mixture of NMR solvent.

3.5.2 Micellar formation of PDA_x-*co*-$PPEA_y$

3.5.2.1 Size distribution of PDAx-co-PPEAy

Size distribution of PDA_x-*co*-$PPEA_y$ was determined by DLS investigated in **Figure 3.32,** measured in H_2O at 25°C with polymer concentration (C_p) = 1 g/L. DLS profiles of the copolymers showed narrow distribution with the particle size in a range of 120 – 200 nm. Low LSI values for PDA_{10}-*co*-$PPEA_{90}$, PDA_{25}-*co*-$PPEA_{75}$ and PDA_{75}-*co*-$PPEA_{25}$ indicate low polymer aggregation dispersed in water. The greater LSI of PDA_{50}-*co*-$PPEA_{50}$, than those of the other copolymers and narrow distribution of DLS profile, implied that this copolymer has a high aggregation to form micelles in water.

	PDA$_{10}$-*co*-PPEA$_{90}$	**PDA$_{25}$-*co*-PPEA$_{75}$**
	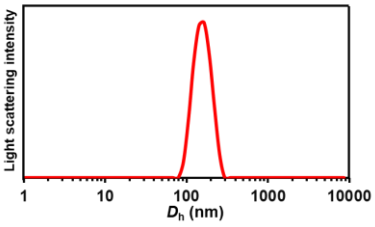	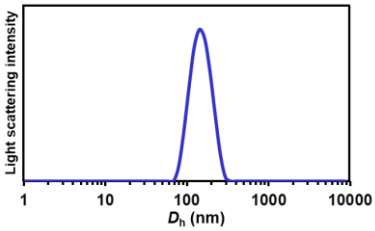
$D_{h,DLS}$ (nm)	170.5 ± 13.1 PDI = 0.246 ± 0.083 LSI = 119 kcps	175.8 ± 26.0 PDI = 0.228 ± 0.026 LSI = 546 kcps
	PDA$_{50}$-*co*-PPEA$_{50}$	**PDA$_{75}$-*co*-PPEA$_{25}$**
	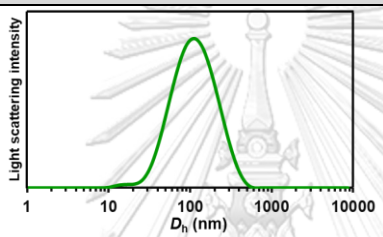	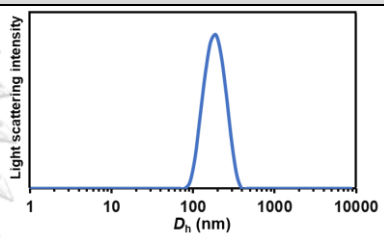
$D_{h,DLS}$ (nm)	127.2 ± 3.3 PDI = 0.270 ± 0.009 LSI = 17,366 kcps	200.4 ± 13.5 PDI = 0.266 ± 0.025 LSI = 161.4 kcps

Figure 3.32 Size distribution profiles of PDA$_x$-*co*-PPEA$_y$, prepared in H_2O with polymer concentration (C_p) = 1.0 g/L, I indicate the light scattering intensity (LSI).

3.5.2.2 CMC determination of the micelles

To further confirm micellar formation, CMC of the polymeric micelles was determined by the logarithmic plot of the concentration of micelles (mg/mL) and the ratio of the first peak at 373 nm and the third peak at 392 nm (I_1/I_3) which was evaluated using emission spectra measured by fluorescence spectroscopy. PDA$_{50}$-*co*-PPEA$_{50}$ solely showed the trend of CMC as 49 µg/mL.

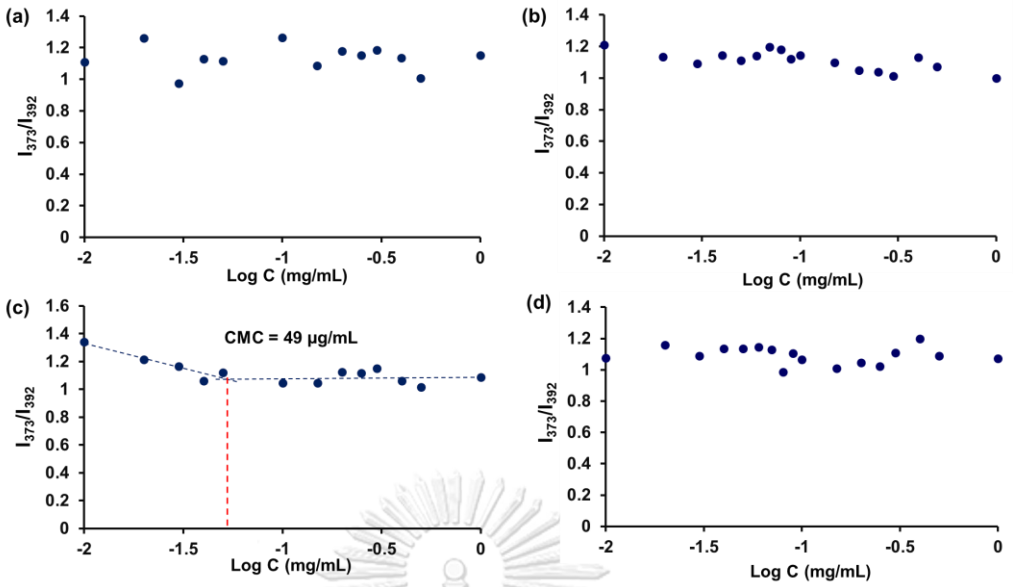

Figure 3.33 CMC determination by fluorescence spectroscopy using the plots of the logarithmic concentration of the micelles (mg/mL) and I_1/I_3 of (a) PDA$_{10}$-*co*-PPEA$_{90}$, (b) PDA$_{25}$-*co*-PPEA$_{75}$, (c) PDA$_{50}$-*co*-PPEA$_{50}$ and (d) PDA$_{75}$-*co*-PPEA$_{25}$

Only CMC trend of PDA$_{50}$-*co*-PPEA$_{50}$ agreed with the DLS result, indicating that the copolymer was well-formation when dispersed in water.

3.5.3 Oxidation stability of PDA$_x$-*co*-PPEA$_y$

Oxidation stability of PDA$_x$-*co*-PPEA$_y$ micelles when exposed to air was determined by UV-Vis spectroscopy. To observe the physical appearance of the micelles dispersed in water, the micelles were continuously stirred in PBS under air for 2 h, 2 d, 5 d, 7 d and 14 d (**Figure 3.38**) to be observed the "auto-oxidation" products in the presence of oxygen in air in UV spectra.

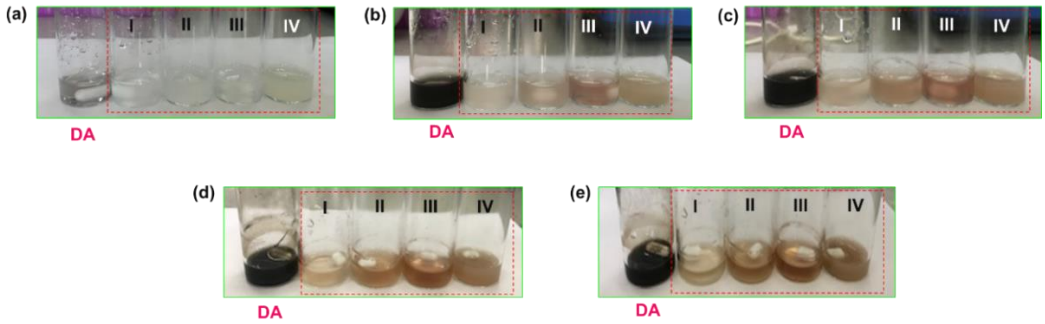

Figure 3.34 The solutions of DA and (I) PDA$_{10}$-*co*-PPEA$_{90}$, (II) PDA$_{25}$-*co*-PPEA$_{75}$, (III) PDA$_{50}$-*co*-PPEA$_{50}$, (IV) PDA$_{75}$-*co*-PPEA$_{25}$ continuously stirred under air for (a) 2 h, (b) 2 d, (c) 5 d, (d) 7 d and (e) 14 d.

Normally, free DA can dissolve in water and become darker when occurring auto-oxidation and auto-polymerization. At 2 h (**Figure 3.34a**), free DA showed a bit darker while the solutions of DA-containing copolymers were still clear indicating that the copolymers conjugated DA can prevent auto-oxidation and polymerization of free DA. However, the micelles solutions became darker upon exposure to air for a longer time. Therefore, these DA conjugated copolymers cannot prevent auto-oxidation when exposed to air for a long time.

DA and its derivatives show the maximum absorbance (λ_{max}) at 280 nm. The UV absorbance with the formation of the auto-oxidation products changes the spectrum by showing other oxidation species such as quinone (λ_{max} = 395 nm), dicatechol (λ_{max} = 280,485 nm) and α,β-dehydrodopamine (λ_{max} = 320 nm). [76]

According to oxidation stability profiles (**Figure 3.35**), PDA$_x$-*co*-PPEA$_y$ exposed to air for 2 h was not generate auto-oxidation products as shown in **Figure 3.35a** that UV spectra of PDA-*co*-PPEA$_y$ show only the characteristic absorbance at λ_{max} = 280 nm of DA. However, UV spectra of the DA-conjugated micelles changed by showing the absorbance of oxidation products between 320 – 485 nm upon direct exposure to air for 2 – 14 d indicated as the black arrow of each profile. It was anticipated that

the copolymers conjugated DA could not be able to stabilize DA inside the core and cannot retard the auto-oxidation of DA by oxygen in air.

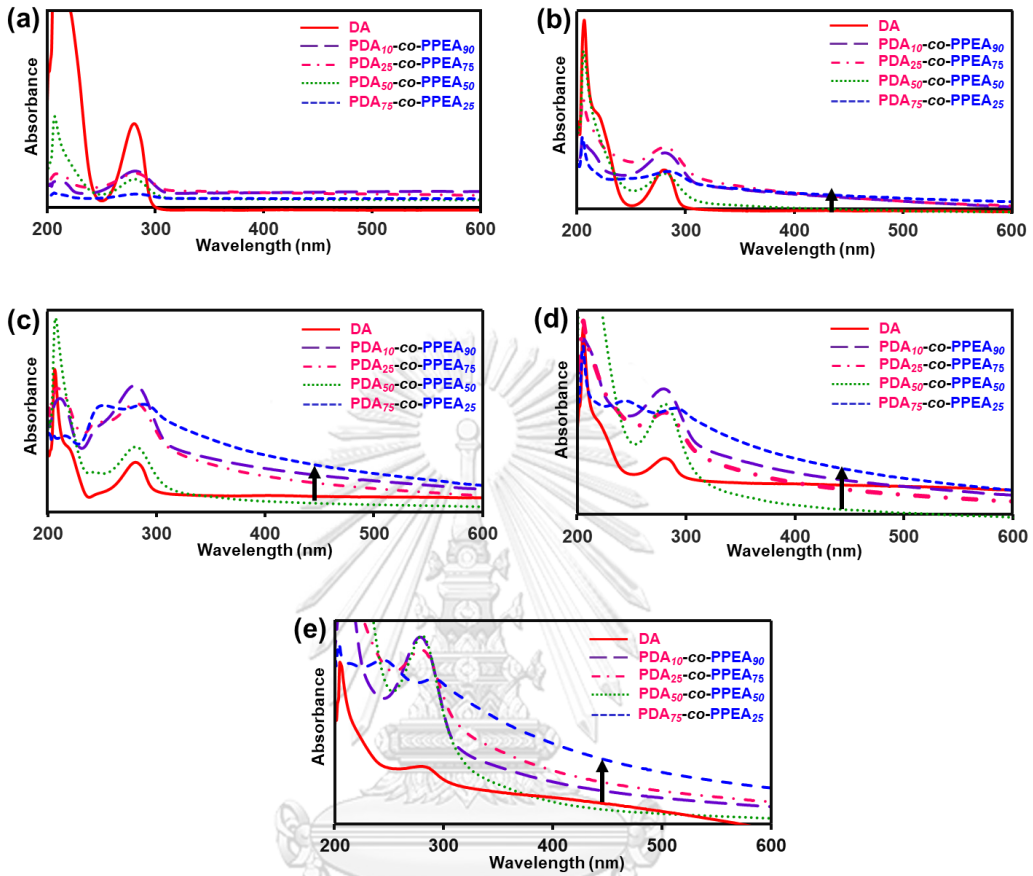

Figure 3.35 Determination of oxidation stability of free DA and PDA$_x$-*co*-PPEA$_y$ when continuously stirred for (a) 2 h, (b) 2 d, (c) 5 d, (d) 7 d and (e) 14 d

CHAPTER IV
CONCLUSION AND SUGGESTION

The preparation and synthetic methodology of core-functionalizable diblock copolymeric micelles based on PFP-entities inside the core have been systematically studied. PMPC was used as a hydrophilic segment and used as a macro-CTA for the extension of PFP-based monomer for a second block synthesis by PISA via RAFT dispersion polymerization. PMPC macro-CTA with various target DPs were synthesized via RAFT polymerization. M_n of PMPC macro-CTA closely resembles theoretical molecular weight and molecular weight distribution (M_w/M_n) were below than 1.5 suggesting that RAFT polymerization was well-controlled.

Synthesis of diblock copolymer PMPC-*b*-PPFPA was systematically investigated with the variation of DP_{PMPC}, DP_{PPFPA}. DP_{PMPC} of 25, 50 and 100 were used as a macro-CTA as well as used as a chain extension for the synthesis of PPFPA as a core-forming block. The polymer solution became precipitation at high DP_{PPFPA} and kinetic study indicated unwell controlled polymerization. Also, DLS profiles displayed bimodal distribution during the growth of PPFPA core-forming block, indicating that *in situ* self-assembled the micelles were not well-formation. Such in this case, the synthesis of diblock copolymer PMPC-*b*-PPFPA was not well-controlled due to different reactivities between MPC and PFPA monomers. Therefore, PFPMA is a tertiary radical monomer that is initiated in the polymerization system as well as a good candidate for the diblock copolymer synthesis using PMPC macro-CTA.

Diblock copolymers of $PMPC_n$-*b*-$PPFPMA_m$ can be also successfully prepared via RAFT dispersion polymerization with the variation of DP_{PMPC}, DP_{PPFPMA} and solid concentration as characterized by ^1H NMR, ^{19}F NMR and FT-IR spectroscopy. According to TEM and DLS analysis, nanostructures assembled from the block copolymers via PISA appeared mostly spherical in shape of varied size and degree of inter-micellar aggregation depending on the solid concentration and the relative

length of the two blocks. The longer core-forming PPFPMA block especially at high solid concentration (20%) yielded bumpy micelles by an aggregate of smaller nanoparticles. Further growth of PPFPMA block, there seems to be a greater number of small nanoparticles combined into one aggregate. However, the solution became precipitated once the conversion of PFPMA was almost complete, implying that the PMPC block with DP of 50 was not enough to provide colloidal stability to the self-assembled structures. As a result of slower kinetic at 5% solid concentration, the assembled structure also appeared as bumpy micelles, each containing a few extremely small particles. Having the same block composition, the PM_{50}-PFM_{60}-*5%* consisted of fewer smaller particles in one aggregate than the PM_{50}-PFM_{60}-*20%* suggesting the solid content has a strong impact on both packing density and size of the aggregates. Increasing the PPFPMA block length further to 109 yielded PM_{50}-PFM_{109}-*5%* of which assembled structure was no longer regular in both size and shape. The un-directional inter-micellar aggregation gave an interconnected network so that the size of individual aggregate cannot be identified. The strong π-π stacking together with hydrophobic interactions among PFP entities of the core-forming PPFPMA block led to the chain inflexibility so that the formation of structures with high-order morphologies was not possible. On the other hand, the inter-micellar aggregation was suppressed once the stabilizer PMPC block was long enough to provide good colloidal stability so that individual micelles could be formed. The well-packed PPFPMA block limited the accessibility of the nucleophilic modifier, a harsh condition (high temperature and catalyst) was therefore required to post-modify the PFP ester groups in the core of nanostructure. Nevertheless, this research investigation has demonstrated the potential of this developed zwitterionic and core-functionalizable nanoassemblies for a wide range of applications.

DA-conjugated polymeric nanostructure is an attractive material for being used as an antioxidant nanoparticle. PPFPA as a polymer precursor was sequentially post-functionalized by the variation ratio of DA and PEA, respectively to yield PDA_x-

co-PPEA$_y$. PDA$_x$-*co*-PPEA$_y$ was characterized by ^{1}H NMR, ^{19}F NMR and ATR-IR spectroscopy. The compositions between DA and PEA in the copolymer were verified by ^{1}H NMR. Size distribution of PDA$_x$-*co*-PPEA$_y$ was determined by DLS. DLS profiles showed narrow distribution in all compositions. The greater LSI of PDA$_{50}$-*co*-PPEA$_{50}$, than those of the other copolymers and narrow distribution of DLS profile implied that this copolymer has a high aggregation to form micelles in water. The results agreed with CMC determination that CMC of PDA$_{50}$-*co*-PPEA$_{50}$ was solely found to be 49 µg/mL while there was no CMC trend for the other compositions. Oxidation stability of PDA$_x$-*co*-PPEA$_y$ micelles when exposed to air was determined by UV-Vis spectroscopy. The polymeric micelles dispersed in water continuously stirred under air for 2 h, 2 d, 5 d, 7 d and 14 d. It was anticipated that the copolymers conjugated DA could not be able to stabilize DA inside the core and cannot retard the auto-oxidation of DA by oxygen in air. It is our on-going effort to post-functionalize PPFPA by reacting with a probe to form a micellar nanosensor that can be used as a nanomaterial for pre-concentration analytes and improve sensitivity of the detection especially organic compound detection in water.

REFERENCES

[1] Liu, K.; Ye, L.; Wang, Y.; Du, G.; Jiang, L., A Pseudopeptide polymer micelle used for asymmetric aatalysis of the aldol reaction in water. *Polymers (Basel)* **2018,** *10* (9), 1004.

[2] Torchilin, V.P., Structure and design of polymeric surfactant-based drug delivery systems. *J. Control Release* **2001,** *73*, 137 - 172.

[3] Deng, R.; Derry, M. J.; Mable, C. J.; Ning, Y.; Armes, S. P., Using dynamic covalent chemistry to drive morphological transitions: controlled release of encapsulated nanoparticles from block copolymer vesicles. *J. Am. Chem. Soc.* **2017,** *139* (22), 7616 - 7623.

[4] Larson, N.; Ghandehari, H., Polymeric conjugates for drug delivery. *Chem. Mater.* **2012,** *24* (5), 840 - 853.

[5] Koker D.; Hoogenboom, R.; De Geest, B. G., Polymeric multilayer capsules for drug delivery. *Chem. Soc. Rev.* **2012,** *41* (7), 2867 - 2884.

[6] Du, J.; Lane, L. A.; Nie, S., Stimuli-responsive nanoparticles for targeting the tumor microenvironment. *J. Control. Release* **2015,** *219*, 205 - 214.

[7] Liu, X.; Yang, Y.; Urban, M. W., Stimuli-responsive polymeric nanoparticles. *Macromol. Rapid Commun.* **2017,** *38* (13), 1700030.

[8] Gao, L. F.; Lin, X.; Hai, X.; Chen, X. W.; Wang, J. H., Polymeric ionic liquid-based fluorescent amphiphilic block copolymer micelle for selective and sensitive detection of *p*-Phenylenediamine. *ACS Appl. Mater. Interfaces* **2018,** *10* (49), 43049 - 43056.

[9] Wu, Y.; Liu, J.; Ma, J.; Liu, Y.; Wang, Y.; Wu, D., Ratiometric nanothermometer based on rhodamine dye-incorporated F127-melamine-formaldehyde polymer nanoparticle: preparation, characterization, wide-range temperature sensing, and precise intracellular thermometry. *ACS Appl. Mater. Interfaces* **2016,** *8* (23), 14396 - 14405.

[10] Wang, Y.; Yin, W.; Ke, W.; Chen, W.; He, C.; Ge, Z., Multifunctional polymeric micelles with amplified fenton reaction for tumor ablation. *Biomacromolecules* **2018,** *19* (6), 1990 - 1998.

[11] Balasubramanian, V.; Onaca, O.; Ezhevskaya, M.; Van Doorslaer, S.; Sivasankaran, B.; Palivan, C. G., A surprising system: polymeric nanoreactors containing a mimic with dual-enzyme activity. *Soft Matter* **2011,** *7* (12), 5595 - 5603.

[12] Kim, J. K.; Yang, S. Y.; Lee, Y.; Kim, Y., Functional nanomaterials based on block copolymer self-assembly. *Prog. Polym. Sci.* **2010,** *35* (11), 1325 - 1349.

[13] Zhang, Q.; Ko, N. R.; Oh, J. K., Recent advances in stimuli-responsive degradable block copolymer micelles: synthesis and controlled drug delivery applications. *Chem. Commun.* **2012,** *48* (61), 7542 - 7552.

[14] Ge, Z.; Liu, S., Functional block copolymer assemblies responsive to tumor and intracellular microenvironments for site-specific drug delivery and enhanced imaging performance. *Chem. Soc. Rev.* **2013,** *42* (17), 7289 -7325.

[15] Zayas, H. A.; Lu, A.; Valade, D.; Amir, F.; Jia, Z.; O'Reilly, R. K.; Monteiro, M. J., Thermoresponsive polymer-supported l-proline micelle catalysts for the direct asymmetric aldol reaction in water. *ACS Macro Lett.* **2013,** *2* (4), 327 - 331.

[16] Mai, Y.; Eisenberg, A., Self-assembly of block copolymers. *Chem. Soc. Rev.* **2012,** *41* (18), 5969 - 5985.

[17] Mori, H.; Endo, T., Amino-acid-based block copolymers by RAFT polymerization. *Macromol. Rapid Commun.* **2012,** *33* (13), 1090 - 1107.

[18] Cheng, F.; Bonder, E. M.; Jäkle, F., Luminescent boron quinolate block copolymers via RAFT polymerization. *Macromolecules* **2012,** *45* (7), 3078 - 3085.

[19] Chakrabarty, A.; Singha, N. K., Tailor-made polyfluoroacrylate and its block copolymer by RAFT polymerization in miniemulsion; improved hydrophobicity in the core-shell block copolymer. *J. Colloid Interface Sci.* **2013,** *408*, 66 - 74.

[20] Qin, Y. Sukul, V.; Pakagos, D.; Cui, C.; Jakle, F., Preparation of organoboron block copolymers via ATRP of silicon and boron-functionalized monomers. *Macromolecules* **2005,** *38*, 8987 - 8990.

[21] Oh, J. K.; Dong, H.; Zhang, R.; Matyjaszewski, K.; Schlaad, H., Preparation of nanoparticles of double-hydrophilic PEO-PHEMA block copolymers by AGET ATRP in inverse miniemulsion. *J. Polym. Sci. A Polym. Chem.* **2007,** *45*, 4764 - 4772.

[22] Min, K.; Gao, H.; Matyjaszewski, K., Preparation of homopolymers and block copolymers in miniemulsion by ATRP using activators generated by electron transfer (AGET). *J. Am. Chem. Soc.* **2004,** *127*, 3825 - 3830.

[23] Li, H.; Li, J.; Ke, W.; Ge, Z., A near-infrared photothermal effect-responsive drug delivery system based on indocyanine green and doxorubicin-loaded polymeric micelles mediated by reversible diels-alder reaction. *Macromol. Rapid Commun.* **2015,** *36* (20), 1841 - 1849.

[24] Penfold, N. J. W.; Yeow, J.; Boyer, C.; Armes, S. P., Emerging trends in polymerization-induced self-assembly. *ACS Macro Lett.* **2019,** *8* (8), 1029 - 1054.

[25] Charleux, B.; Delaittre, G.; Rieger, J.; D'Agosto, F., Polymerization-induced self-assembly: from soluble macromolecules to block copolymer nano-objects in one step. *Macromolecules* **2012,** *45* (17), 6753 - 6765.

[26] Dai, X.; Yu, L.; Zhang, Y.; Zhang, L.; Tan, J., Polymerization-induced self-assembly via RAFT-mediated emulsion polymerization of methacrylic monomers. *Macromolecules* **2019,** *52* (19), 7468 - 7476.

[27] Karagoz, B.; Esser, L.; Duong, H. T.; Basuki, J. S.; Boyer, C.; Davis, T. P., Polymerization-induced self-assembly (PISA) – control over the morphology of nanoparticles for drug delivery applications. *Polym. Chem.* **2014,** *5* (2), 350 - 355.

[28] Pei, Y.; Dharsana, N. C.; van Hensbergen, J. A.; Burford, R. P.; Roth, P. J.; Lowe, A. B., RAFT dispersion polymerization of 3-phenylpropyl methacrylate with poly[2-(dimethylamino)ethyl methacrylate] macro-CTAs in ethanol and associated thermoreversible polymorphism. *Soft Matter* **2014,** *10* (31), 5787 - 5796.

[29] Tan, J.; Li, X.; Zeng, R.; Liu, D.; Xu, Q.; He, J.; Zhang, Y.; Dai, X.; Yu, L.; Zeng, Z., Expanding the scope of polymerization-induced self-assembly: Z-RAFT-mediated photoinitiated dispersion polymerization. *ACS Macro Lett.* **2018,** *7* (2), 255 - 262.

[30] Wang, G.; Wang, Z.; Lee, B.; Yuan, R.; Lu, Z.; Yan, J.; Pan, X.; Song, Y.; Bockstaller, M. R.; Matyjaszewski, K., Polymerization-induced self-assembly of acrylonitrile via ICAR ATRP. *Polymer* **2017,** *129*, 57 - 67.

[31] Alzahrani, A.; Zhou, D.; Kuchel, R. P.; Zetterlund, P. B.; Aldabbagh, F., Polymerization-induced self-assembly based on ATRP in supercritical carbon dioxide. *Polym. Chem.* **2019,** *10* (21), 2658 - 2665.

[32] Huo, M.; Zhang, Y.; Zeng, M.; Liu, L.; Wei, Y.; Yuan, J., Morphology evolution of polymeric assemblies regulated with fluoro-containing mesogen in polymerization-induced self-assembly. *Macromolecules* **2017,** *50* (20), 8192 - 8201.

[33] Ye, Q.; Huo, M.; Zeng, M.; Liu, L.; Peng, L.; Wang, X.; Yuan, J., Photoinduced reversible worm-to-vesicle transformation of azo-containing block copolymer assemblies prepared by polymerization-induced self-assembly. *Macromolecules* **2018,** *51* (9), 3308 - 3314.

[34] Zhao, W.; Ta, H. T.; Zhang, C.; Whittaker, A. K., Polymerization-induced self-assembly (PISA) -control over the morphology of (19)F-containing polymeric nano-objects for cell uptake and tracking. *Biomacromolecules* **2017,** *18* (4), 1145 - 1156.

[35] Blanazs, A.; Madsen, J.; Battaglia, G.; Ryan, A. J.; Armes, S. P., Mechanistic insights for block copolymer morphologies: how do worms form vesicles? *J. Am. Chem. Soc.* **2011,** *133* (41), 16581 - 16587.

[36] Blanazs, A.; Ryan, A. J.; Armes, S. P., Predictive phase diagrams for RAFT aqueous dispersion polymerization: effect of block copolymer composition, molecular weight, and copolymer concentration. *Macromolecules* **2012,** *45* (12), 5099 - 5107.

[37] Semsarilar, M.; Jones, E. R.; Blanazs, A.; Armes, S. P., Efficient synthesis of sterically-stabilized nano-objects via RAFT dispersion polymerization of benzyl methacrylate in alcoholic media. *Adv. Mater.* **2012,** *24* (25), 3378 - 3382.

[38] Gauthier, M. A.; Gibson, M. I.; Klok, H. A., Synthesis of functional polymers by post-polymerization modification. *Angew. Chem. Int. Ed. Engl.* **2009,** *48* (1), 48 - 58.

[39] Boaen, N. K.; Hillmyer, M. A., Post-polymerization functionalization of polyolefins. *Chem. Soc. Rev.* **2005,** *34* (3), 267 - 275.

[40] Günay, K. A.; Theato, P.; Klok, H.-A., Standing on the shoulders of hermann staudinger: post-polymerization modification from past to present. *J. Polyme. Sci. A Polym. Chem.* **2013,** *51* (1), 1 - 28.

[41] Arslan, M.; Gok, O.; Sanyal, R.; Sanyal, A., Clickable poly(ethylene glycol)-based copolymers using azide-alkyne click cycloaddition-mediated step-growth polymerization. *Macromol. Chem. Phys.* **2014,** *215* (22), 2237 - 2247.

[42] Chen, J.; Sun, R.; Liao, X.; Han, H.; Li, Y.; Xie, M., Tandem metathesis polymerization-induced self-assembly to nanostructured block copolymer

and the controlled triazolinedione modification for enhancing dielectric properties. *Macromolecules* **2018,** *51* (24), 10202 - 10213.

[43] Busatto, N.; Keddie, J. L.; Roth, P. J., Sphere-to-worm morphological transitions and size changes through thiol–para-fluoro core modification of PISA-made nano-objects. *Polym. Chem.* **2020,** *11* (3), 704 - 711.

[44] Agar, S.; Baysak, E.; Hizal, G.; Tunca, U.; Durmaz, H., An emerging post-polymerization modification technique: The promise of thiol-para-fluoro click reaction. *J. Polym. Sci. A Polym. Chem.* **2018,** *56* (12), 1181 - 1198.

[45] Singha, N. K.; Gibson, M. I.; Koiry, B. P.; Danial, M.; Klok, H. A., Side-chain peptide-synthetic polymer conjugates via tandem "ester-amide/thiol-ene" post-polymerization modification of poly(pentafluorophenyl methacrylate) obtained using ATRP. *Biomacromolecules* **2011,** *12* (8), 2908 - 2913.

[46] Sardon, H.; Chan, J. M. W.; Ono, R. J.; Mecerreyes, D.; Hedrick, J. L., Highly tunable polyurethanes: organocatalyzed polyaddition and subsequent post-polymerization modification of pentafluorophenyl ester sidechains. *Polym. Chem.* **2014,** *5* (11), 3547 - 3550.

[47] Graisuwan, W.; Zhao, H.; Kiatkamjornwong, S.; Theato, P.; Hoven, V. P., Formation of thermo-sensitive and cross-linkable micelles by self-assembly of poly(pentafluorophenyl acrylate)-containing block copolymer. *J. Polym. Sci. A Polym. Chem.* **2015,** *53* (9), 1103 - 1113.

[48] Monge, S.; Haddleton, D. M., Synthesis of precursors of poly(acryl amides) by copper mediated living radical polymerization in DMSO. *Eur. Polym. J.* **2004,** *40* (1), 37 - 45.

[49] Eberhardt, M.; Théato, P., RAFT Polymerization of pentafluorophenyl methacrylate: preparation of reactive linear diblock copolymers. *Macromol. Rapid Commun.* **2005,** *26* (18), 1488 - 1493.

[50] Eberhardt, M.; Mruk, R.; Zentel, R.; Théato, P., Synthesis of pentafluorophenyl(meth)acrylate polymers: New precursor polymers for the synthesis of multifunctional materials. *Eur. Polym. J.* **2005,** *41* (7), 1569 - 1575.

[51] Theato, P., Synthesis of well-defined polymeric activated esters. *J. Polym. Sci. A Polym. Chem.* **2008,** *46* (20), 6677 - 6687.

[52] Gibson, M. I.; Fröhlich, E.; Klok, H.-A., Postpolymerization modification of poly(pentafluorophenyl methacrylate): Synthesis of a diverse water-soluble polymer library. *J. Polym. Sci. A Polym. Chem.* **2009,** *47* (17), 4332 - 4345.

[53] Pinyakit, Y.; Palaga, T.; Kiatkamjornwong, S.; Hoven, V. P., Sequential post-polymerization modification of a pentafluorophenyl ester-containing homopolymer: a convenient route to effective pH-responsive nanocarriers for anticancer drugs. *J. Mater. Chem. B* **2020,** *8* (3), 454 - 464.

[54] Graisuwan, W.; Puthong, S.; Zhao, H.; Kiatkamjornwong, S.; Theato, P.; Hoven, V. P., Thermoresponsive and active functional fiber mats for cultured cell recovery. *Biomacromolecules* **2017,** *18* (11), 3714 - 3725.

[55] Nilles, K.; Theato, P., Sequential conversion of orthogonally functionalized diblock copolymers based on pentafluorophenyl esters. *J. Polym. Sci. A Polym. Chem.* **2010,** *48* (16), 3683 - 3692.

[56] Noree, S.; Tangpasuthadol, V.; Kiatkamjornwong, S.; Hoven, V. P., Cascade post-polymerization modification of single pentafluorophenyl ester-bearing homopolymer as a facile route to redox-responsive nanogels. *J. Colloid Interface Sci.* **2017,** *501*, 94 - 102.

[57] Vakili, M.; Cunningham, V. J.; Trebbin, M.; Theato, P., Polymerization-induced thermal self-assembly of functional and thermo-responsive diblock copolymer nano-objects via RAFT aqueous polymerization. *Macromol. Chem. Phys.* **2019,** *220* (2), 1800370.

[58] Hu, N.; Li, J. H.; Shi, D. J.; Liu, X. Y.; Chen, M. Q., Synthesis and self-assembly behaviors of four-armed amphiphilic polystyrene-b-poly(N-isopropylacrylamide) copolymers. *Polym. Sci. Ser. B* **2013,** *55* (1-2), 69 - 76.

[59] Damsongsang, P.; Hoven, V. P.; Yusa, S.-i., Core-functionalized nanoaggregates: preparation via polymerization-induced self-assembly and their applications. *New J. Chem.* **2021**, *45*, 12776 - 12791.

[60] Couturaud, B.; Georgiou, P. G.; Varlas, S.; Jones, J. R.; Arno, M. C.; Foster, J. C.; O'Reilly, R. K., Poly(pentafluorophenyl methacrylate)-based nano-objects developed by photo-PISA as scaffolds for post-polymerization functionalization. *Macromol. Rapid Commun.* **2019,** *40* (2), e1800460.

[61] Inoue, Y.; Onodera, Y.; Ishihara, K., Preparation of a thick polymer brush layer composed of poly(2-methacryloyloxyethyl phosphorylcholine) by surface-initiated atom transfer radical polymerization and analysis of protein adsorption resistance. *Colloids Surf. B Biointerfaces* **2016,** *141*, 507 - 512.

[62] Ishihara, K.; Mu, M.; Konno, T.; Inoue, Y.; Fukazawa, K., The unique hydration state of poly(2-methacryloyloxyethyl phosphorylcholine). *J. Biomater. Sci. Polym. Ed.* **2017,** *28* (10-12), 884 - 899.

[63] Sugihara, S.; Blanazs, A.; Armes, S. P.; Ryan, A. J.; Lewis, A. L., Aqueous dispersion polymerization: a new paradigm for in situ block copolymer self-assembly in concentrated solution. *J. Am. Chem. Soc.* **2011,** *133* (39), 15707 - 15713.

[64] Shihara, K. Ueda, T.; Nakabayashi, N., Preparation of phospholipid polymers and their properties as polymer hydrogel membranes. *Polym. J.* **1990,** *22*, 355 - 360.

[65] Ishihara, K. Oshida, H.; Endo, Y.; Ueda, T.; Watanabe, A.; Nakabayashi, N., Hemocompatibility of human whole blood on polymers with a phospholipid polar group and its mechanism. *J. Biomed. Mater. Res.* **1992,** *26*, 1543 - 1552.

[66] Iwata, R.; Suk-In, P.; Hoven, V. P.; Takahara, A.; Akiyoshi, K.; Iwasaki, Y., Control of nanobiointerfaces generated from well-defined biomimetic polymer brushes for protein and cell manipulations. *Biomacromolecules* **2004,** *5* (6), 2308 - 2314.

[67] Park, J.; Kurosawa, S.; Takai, M.; Ishihara, K., Antibody immobilization to phospholipid polymer layer on gold substrate of quartz crystal microbalance immunosensor. *Colloids Surf. B Biointerfaces* **2007,** *55* (2), 164 - 172.

[68] Murali, V. S.; Wang, R.; Mikoryak, C. A.; Pantano, P.; Draper, R., Rapid detection of polyethylene glycol sonolysis upon functionalization of carbon nanomaterials. *Exp. Biol. Med.* **2015,** *240* (9), 1147 - 1151.

[69] Hu, J.; Zhuang, W.; Ma, B.; Su, X.; Yu, T.; Li, G.; Hu, Y.; Wang, Y., Redox-responsive biomimetic polymeric micelle for simultaneous anticancer drug delivery and aggregation-induced emission active Imaging. *Bioconjug. Chem.* **2018,** *29* (6), 1897 - 1910.

[70] Noy, J.-M.; Cao, C.; Stenzel, M., Length of the Stabilizing zwitterionic poly(2-methacryloyloxyethyl phosphorycholine) block influences the activity of the conjugated arsenic drug in drug-directed polymerization-induced self-assembly particles. *ACS Macro Lett.* **2018,** *8* (1), 57 - 63.

[71] Wu, Z.; Chen, B.; Gan, Z.; Chen, F.; Luo, X., Exogenous vitamin C-triggered surface charge conversion of pH/reduction-responsive micelles for the enhanced tumor-specific activity of loaded doxorubicin. *Mol. Pharm.* **2020,** *17* (3), 954 - 964.

[72] Su, X.; Ma, B.; Hu, J.; Yu, T.; Zhuang, W.; Yang, L.; Li, G.; Wang, Y., Dual-responsive doxorubicin-conjugated polymeric micelles with aggregation-induced emission active bioimaging and charge conversion for cancer therapy. *Bioconjug. Chem.* **2018,** *29* (12), 4050 - 4061.

[73] Xie, R.; Tian, Y.; Peng, S.; Zhang, L.; Men, Y.; Yang, W., Poly(2-methacryloyloxyethyl phosphorylcholine)-based biodegradable nanogels for controlled drug release. *Polym. Chem.* **2018,** *9* (36), 4556 - 4565.

[74] Ma, B.; Zhuang, W.; Wang, Y.; Luo, R.; Wang, Y., pH-sensitive doxorubicin-conjugated prodrug micelles with charge-conversion for cancer therapy. *Acta Biomater.* **2018,** *70*, 186 - 196.

[75] Kirkinezos, I. G.; Moraes, C. T., Reactive oxygen species and mitochondrial diseases. Semin. *Cell Dev. Biol.* **2001,** *12* (6), 449 - 457.

[76] Hasegawa, U.; Moriyama, M.; Uyama, H.; van der Vlies, A. J., Catechol-bearing block copolymer micelles: Structural characterization and antioxidant activity. *Polymer* **2015,** *66*, 1 - 7.

[77] Yang, B.; Chen, Y.; Shi, J., Reactive oxygen species (ROS)-based nanomedicine. *Chem. Rev.* **2019,** *119* (8), 4881 - 4985.

[78] Nishikawa, M., Reactive oxygen species in tumor metastasis. *Cancer Lett.* **2008,** *266* (1), 53 - 59.

[79] Mittal, M.; Siddiqui, M. R.; Tran, K.; Reddy, S. P.; Malik, A. B., Reactive oxygen species in inflammation and tissue injury. *Antioxid. Redox Signal* **2014,** *20* (7), 1126 - 1167.

[80] Dou, Y.; Li, C.; Li, L.; Guo, J.; Zhang, J., Bioresponsive drug delivery systems for the treatment of inflammatory diseases. *J. Control Release* **2020,** *327*, 641 - 666.

[81] Pandhair, V. Sekhon, B. S., Reactive oxygen species and antioxidants in plants: an overview. *J. Plant Biochem. Biotech.* **2006,** *15*, 71 - 78.

[82] Nagasaki, Y., Design and application of redox polymers for nanomedicine. *Polym. J.* **2018,** *50* (9), 821 - 836.

[83] Vong, L. B.; Kobayashi, M.; Nagasaki, Y., Evaluation of the toxicity and antioxidant activity of redox nanoparticles in zebrafish (Danio rerio) embryos. *Mol. Pharm.* **2016,** *13* (9), 3091 - 3097.

[84] Vong, L. B.; Nagasaki, Y., Combination treatment of murine colon cancer with doxorubicin and redox nanoparticles. *Mol. Pharm.* **2016,** *13* (2), 449 - 455.

[85] Scalbert, A. Johnson, I. T.; Saltmarsh, M., Polyphenols: antioxidants and beyond. *Am. J. Clin. Nutr.* **2005,** *81*, 215S - 217S.

[86] Gonzalez-Sarrias, A.; Nunez-Sanchez, M. A.; Tomas-Barberan, F. A.; Espin, J. C., Neuroprotective effects of bioavailable polyphenol-derived metabolites against oxidative stress-induced cytotoxicity in human neuroblastoma SH-SY5Y cells. *J. Agric. Food Chem.* **2017,** *65* (4), 752 - 758.

[87] Dubey, S. Singh, D.; Misra, R. A., Enzymatic synthesis and various properties of poly(catechol). *Enzyme Microb. Technol.* **1998,** *23*, 432 - 437.

[88] Dreyer, D. R.; Miller, D. J.; Freeman, B. D.; Paul, D. R.; Bielawski, C. W., Elucidating the structure of poly(dopamine). *Langmuir* **2012,** *28* (15), 6428 - 6435.

[89] Lynge, M. E. W., R.; Postma, A.; Stadler, B., Polydopamine—a nature-inspired polymer coating for biomedical science. *Nanoscale* **2011,** (3), 4916 - 4928.

[90] Moriyama, M.; Metzger, S.; van der Vlies, A. J.; Uyama, H.; Ehrbar, M.; Hasegawa, U., Inhibition of angiogenesis by antioxidant micelles. *Adv. Healthc. Mater.* **2015,** *4* (4), 569 - 575.

[91] Patil, N.; Cordella, D.; Aqil, A.; Debuigne, A.; Admassie, S.; Jérôme, C.; Detrembleur, C., Surface- and redox-Active multifunctional polyphenol-derived poly(ionic liquid)s: controlled synthesis and characterization. *Macromolecules* **2016,** *49* (20), 7676 - 7691.

[92] Shahkaramipour, N.; Lai, C. K.; Venna, S. R.; Sun, H.; Cheng, C.; Lin, H., Membrane surface modification using thiol-containing zwitterionic polymers via bioadhesive polydopamine. *Ind. Eng. Chem. Res.* **2018,** *57* (6), 2336 - 2345.

[93] Chang, C. C.; Kolewe, K. W.; Li, Y.; Kosif, I.; Freeman, B. D.; Carter, K. R.; Schiffman, J. D.; Emrick, T., Underwater superoleophobic surfaces prepared from polymer zwitterion/dopamine composite coatings. *Adv. Mater. Interfaces* **2016,** *3* (6), 1500521.

[94] Asha, A. B.; Chen, Y.; Zhang, H.; Ghaemi, S.; Ishihara, K.; Liu, Y.; Narain, R., Rapid mussel-inspired surface zwitteration for enhanced antifouling and antibacterial properties. *Langmuir* **2019,** *35* (5), 1621 - 1630.

[95] Ishihara K., Ueda, T., Nakabayashi, N., Preparation of Phospholipid and Their Properties as Polymer Hydrogel Membranes. *Polym. j.*, **1990**, 22 (5) 355-360.

[96] Matsuo, Y.; Konno, R.; Ishizone, T.; Goseki, R.; Hirao, A., Precise synthesis of block polymers composed of three or more blocks by specially designed linking methodologies in conjunction with living anionic polymerization system. *Polymers* **2013,** *5* (3), 1012 - 1040.

[97] Tan, J.; Xu, Q.; Zhang, Y.; Huang, C.; Li, X.; He, J.; Zhang, L., Room Temperature Synthesis of Self-Assembled AB/B and ABC/BC Blends by Photoinitiated Polymerization-Induced Self-Assembly (Photo-PISA) in Water. *Macromolecules* **2018,** *51* (18), 7396 - 7406.

[98] Lowe, A. B., RAFT alcoholic dispersion polymerization with polymerization-induced self-assembly. *Polymer* **2016,** *106*, 161 - 181.

[99] Foster, J. C.; Varlas, S.; Couturaud, B.; Coe, Z.; O'Reilly, R. K., Getting into shape: reflections on a new generation of cylindrical nanostructures' self-assembly using polymer building blocks. *J. Am. Chem. Soc.* **2019,** *141* (7), 2742 - 2753.

[100] Guan, S.; Chen, A., Influence of spacer lengths on the morphology of biphenyl-containing liquid crystalline block copolymer nanoparticles via polymerization-induced self-assembly. *Macromolecules* **2020,** *53* (15), 6235 - 6245.

[101] Sugihara, S.; Armes, S. P.; Blanazs, A.; Lewis, A. L., Non-spherical morphologies from cross-linked biomimetic diblock copolymers using RAFT aqueous dispersion polymerization. *Soft Matter* **2011,** *7* (22), 10787 - 10793.

[102] Wang, Q.; Zhang, Q.; Zhang, Q. W.; Li, X.; Zhao, C. X.; Xu, T. Y.; Qu, D. H.; Tian, H., Color-tunable single-fluorophore supramolecular system with assembly-encoded emission. *Nat. Commun.* **2020,** *11* (1), 158 - 166.

[103] Wu, Y.; Wang, J.; Zeng, F.; Huang, S.; Huang, J.; Xie, H.; Yu, C.; Wu, S., Pyrene derivative emitting red or near-Infrared light with monomer/excimer conversion and its application to ratiometric detection of hypochlorite. *ACS Appl. Mater. Interfaces* **2016,** *8* (2), 1511 - 1519.

[104] Osa, M.; Itoda, Y.; Suzuki, Y.; Yumoto, T.; Yoshida, A., A fluorescence probe study on the effects of surfactants on cloud points in aqueous poly(N-isopropylacrylamide) solutions. *Polym. J.* **2014,** *47* (1), 59 - 65.

[105] Basu Ray, G.; Chakraborty, I.; Moulik, S. P., Pyrene absorption can be a convenient method for probing critical micellar concentration (cmc) and indexing micellar polarity. *J. Colloid Interface Sci.* **2006,** *294* (1), 248 - 254.

[106] Bains, G. K.; Kim, S. H.; Sorin, E. J.; Narayanaswami, V. The extent of pyrene excimer fluorescence emission is a reflector of distance and flexibility: analysis of the segment linking the LDL receptor-binding and tetramerization domains of apolipoprotein E3. *Biochemistry* **2012,** *51* (31), 6207 - 6219.

[107] Hasegawa, U.; Moriyama, M.; Uyama, H.; van der Vlies, A. J. Catechol-bearing block copolymer micelles: Structural characterization and antioxidant activity. *Polymer* **2015,** *66*, 1 - 7.

APPENDIX

PM_{25}-PF_m-*20%*	PM_{50}-PF_m-*20%*
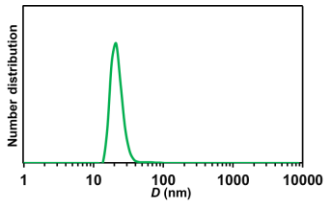	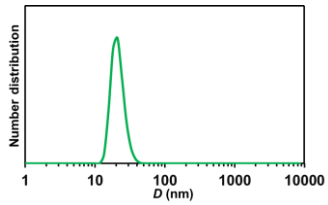
Size = 20.2 ± 9.5	Size = 23.1 ± 7.5
m = 17,	m = 31,
PDI = 0.457 ± 0.298, LSI = 3,702	PDI = 0.429 ± 0.174, LSI = 12,262
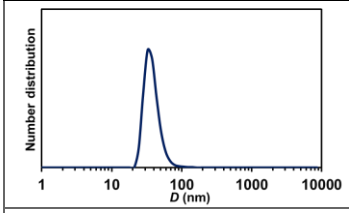	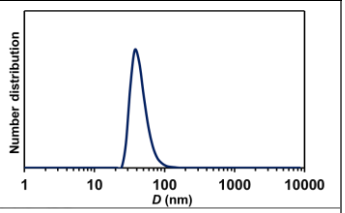
Size = 35.8 ± 22.9	Size = 50.1 ± 6.2
m = 29,	m = 60,
PDI = 0.298 ± 0.018, LSI = 26,219	PDI = 0.174 ± 0.018, LSI = 22,445
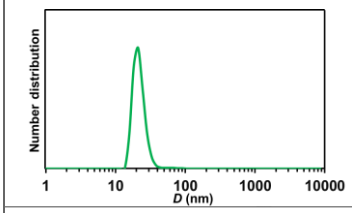	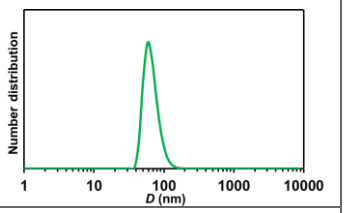
Size = 31.4 ± 15.5	Size = 61.2 ± 4.1
m = 58,	m = 77,
PDI = 0.255 ± 0.016, LSI = 37,054	PDI = 0.137 ± 0.056, LSI = 26,759
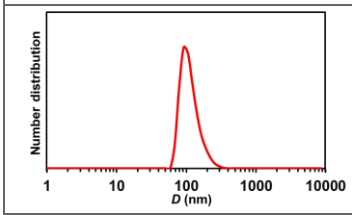	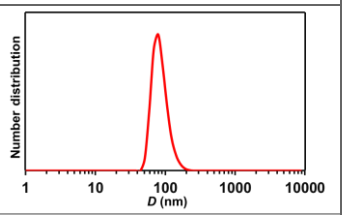
Size = 108.7 ± 16.2	Size = 81.4 ± 6.8
m = 94,	m = 92,
PDI = 0.130 ± 0.036, LSI = 97,842	PDI = 0.105 ± 0.051, LSI = 64,143

Figure A1 DLS profiles of PM_{25}-PF_m-*20%* and PM_{50}-PF_m-*20%* as number distribution in TFE using polymer concentration (C_p) 1 mg/mL

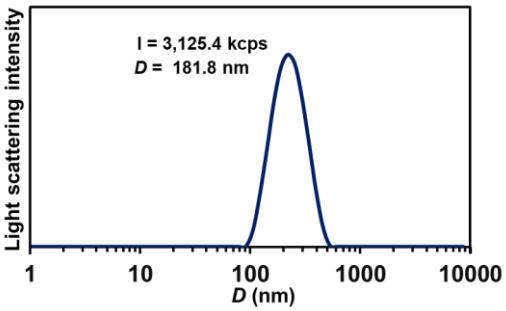

Figure A2 DLS profile of $PMPC_{25}$ Macro-CTA in TFE using polymer concentration (C_p) 1 mg/mL

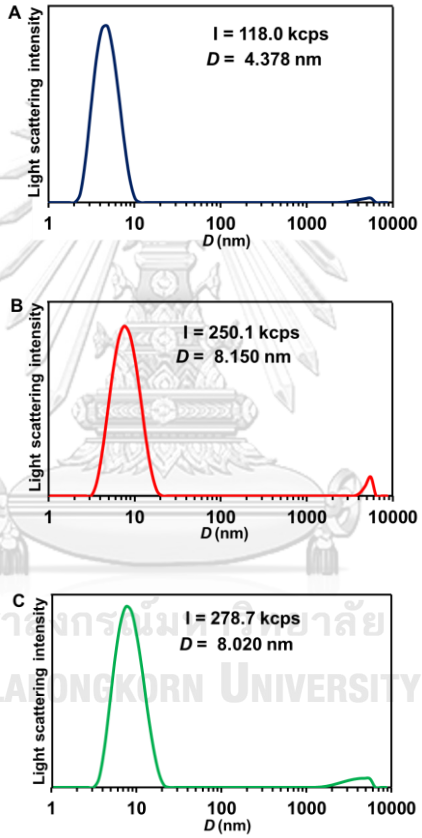

Figure A3 DLS profiles of PMPC macro-CTA with DPs of (a) 25, (b) 50 and (c) 100 in EtOH using polymer concentration (C_p) 1 mg/mL

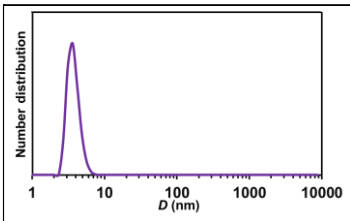	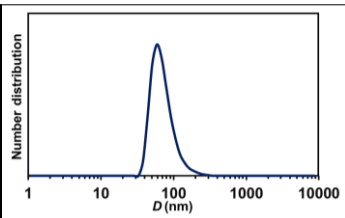	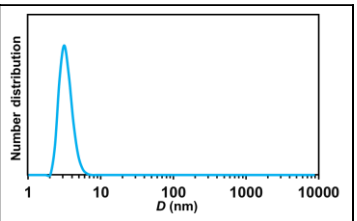
Size = 3.8 ± 0.6	Size = 58.3 ± 32.4	Size = 3.3 ± 0.3
m = 13,	m = 49,	m = 85,
PDI = 0.496 ± 0.007, LSI = 471.4 kcps	PDI = 0.683 ± 0.077, LSI = 541.5 kcps	PDI = 0.683 ± 0.077, LSI = 340.5 kcps
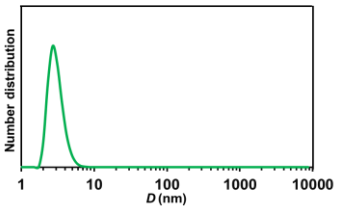	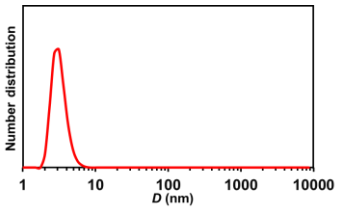	
Size = 2.8 ± 0.3	Size = 3.0 ± 0.2	
m = 92,	m = 94	
PDI = 0.328 ± 0.004, LSI = 89.9 kcps	PDI = 0.347 ± 0.137, LSI = 97.7 kcps	

Figure A4 DLS profiles of PM_{25}-PF_m-20% as number distribution in EtOH using polymer concentration (C_p) 1 mg/mL

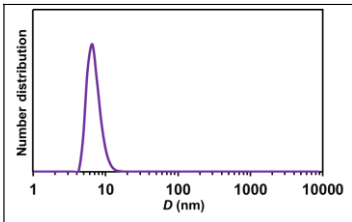	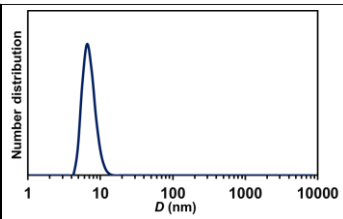	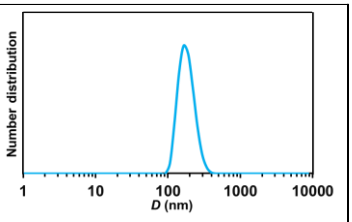
Size = 6.3 ± 0.5	Size = 6.8 ± 0.5	Size = 184.6 ± 12.4
m = 7,	m = 17,	m = 54,
PDI = 0.569 ± 0.029, LSI = 464 kcps	PDI = 1.000 ± 0.000, LSI = 1,298 kcps	PDI = 0.069 ± 0.069, LSI = 82,817 kcps
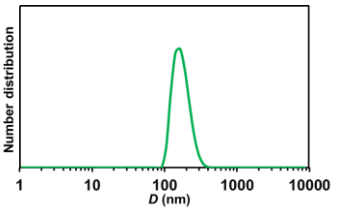	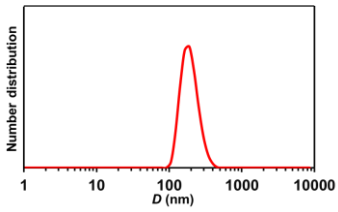	
Size = 171.6 ± 8.1	Size = 190.6 ± 5.8	
m = 100,	m = 100	
PDI = 0.079 ± 0.039, LSI = 92,604 kcps	PDI = 0.079 ± 0.019, LSI = 49,120 kcps	

Figure A5 DLS profiles of PM_{100}-PF_m-*20%* as number distribution in EtOH using polymer concentration (C_p) 1 mg/mL

20% solid	5% solid	
PM_{50}-PFM_m	PM_{50}-PFM_m	PM_{100}-PFM_m
	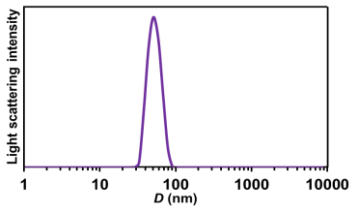	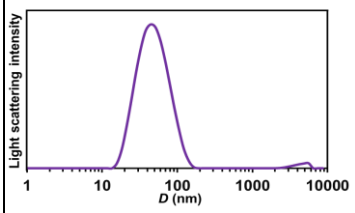
	Size = 53.1 ± 2.3	Size = 40.8 ± 5.8
	m = 22,	m = 23,
	PDI = 0.144 ± 0.080, LSI = 1,206	PDI = 0.235 ± 0.024, LSI = 258
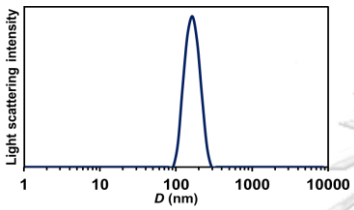	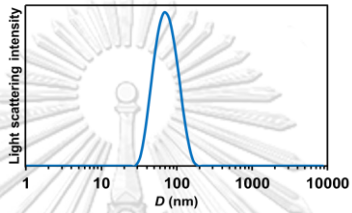	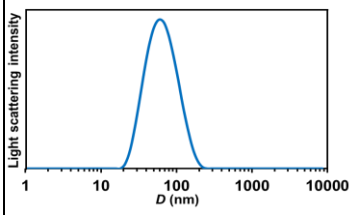
Size = 169.8 ± 3.1	Size = 74.9 ± 0.7	Size = 64.6 ± 3.8
m = 60,	m = 60,	m = 61,
PDI = 0.009 ± 0.007, LSI = 130,143	PDI = 0.095 ± 0.010, LSI = 3,173	PDI = 0.159 ± 0.057, LSI = 917
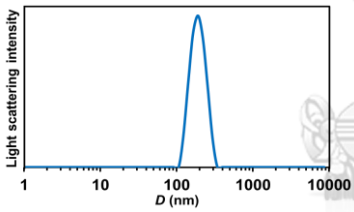	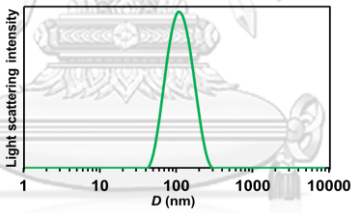	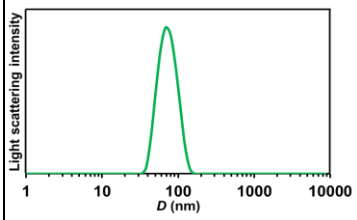
Size = 194.6 ± 1.5	Size = 116.5 ± 2.4	Size = 73.2 ± 1.3
m = 93,	m = 109,	m = 109,
PDI = 0.036 ± 0.005, LSI = 98,549	PDI = 0.117 ± 0.021, LSI = 7,637	PDI = 0.161 ± 0.157, LSI = 3,330

Figure A6 DLS profiles as a function of LSI of PM_{50}-PFM_m and PM_{100}-PFM_m series with a variety of solid concentration

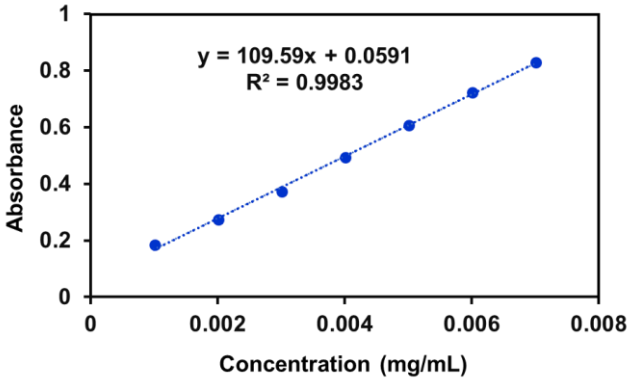

Figure A7 Calibration curve of PMA as a function of dye concentration in MeOH.

VITA

NAME	Miss Panittha Damsongsang
DATE OF BIRTH	3 September 1992
PLACE OF BIRTH	Bangkok
INSTITUTIONS ATTENDED	Department of Chemisitry, Faculty of Sciene, Chulalongkorn University
HOME ADDRESS	42/83 Chalongkrung Road, Lamphakchee, Nongchok, Bangkok, 10530
PUBLICATION	Pinyorospathum, C.; Chaiyo, S.; Sae-ung, P.; Hoven, V. P.; Damsongsang, P.; Siangproh, W.; Chailapakul, O. "Disposable paper-based electrochemical sensor using thiol-terminated poly(2-methacryloyloxyethyl phosphorylcholine) for the label-free detection of C-reactive protein" Microchim. Acta, 2019, 186(7), 472. Sharker, K.K.; Shigeta, Y.; Ozoe, S.; Damsongsang, P.; Hoven, V.P.; Yusa, S. "Upper critical solution temperature behavior of pH-responsive amphoteric statistical copolymers in aqueous solutions" ACS Omega, 2021, 6 (13), 9153 – 9163. Damsongsang, P.; Hoven V.P.; Yusa, S. "Core-functionalized nanoaggregates: preparation via polymerization-induced self-assembly and their applications" New J. Chem., 2021, 45, 12776 – 12791. Meethong, T.; Damsongsang, P.; Ngamchuea, K.; Chainok, K.; Sahasithiwat, S.; Tuntulani, T.; Vanalabhpatana, P.; Parasuk, V.; Thamyongkit, P.; Hoven, V.P.; Unruangsri, J. "Nickel-based water-soluble metallopolymer for the electrochemical hydrogen evolution reaction in neutral-

pH water” 2021, 3 (10), 5051 – 5060.
Damsongsang, P.; Yusa, S.; Hoven, V.P. “Zwitterionic nano-objects having functionalizable hydrophobic core: formation via polymerization-induced self-assembly and their morphology” Eur. Polym. J. “Submitted manuscript”.